EVOKED POTENTIALS AND THEIR APPLICATIONS IN CARDIAC ARREST, PROSTHETIC FEEDBACK, AND FOCUSED ULTRASOUND

by

Ze Ou

A thesis submitted to Johns Hopkins University
in conformity with the requirements for the degree of
Master of Science in Engineering

Baltimore, Maryland
August, 2022

Abstract

The hypoxic-ischemic (HI) brain injury is a major complication after cardiac arrest (CA). While the HI brain injury affects all regions of the brain, the majority of the studies have focused on the injury of the cerebral cortex and the hippocampus. The thalamus is an important subcortical structure due to its functions in sensation, sleep, attention, and arousal, and has been shown to be selectively vulnerable to HI injury. Despite the importance of the thalamus, there does not exists a translatable quantitative metric of thalamic injury after CA. Thus, this thesis focuses on studying thalamic injury after CA using somatosensory evoked potentials (SSEPs). The thesis first reviews past studies on thalamic blood flow, metabolism, immune response, cell damage, and electrophysiology change after CA to paint a full picture of the problem. The existing quantitative metrics of somatosensory evoked potentials to evaluate the integrity of the somatosensory pathway after CA are then reported to identify potential areas for breakthrough. Lastly, our current work on noninvasive monitoring of thalamocortical (TC) connectivity with wavelet filtering and Granger causality (GC) analysis is presented. Multiresolution wavelet (MRW) analysis extracted the SSEP N10 and high-frequency oscillation (HFO) components. The Granger causality between the two components were calculated. The results show that the HFO to N10 GC measure could reflect the severity of CA and highlights the first 10 minutes post-return of spontaneous circulation (ROSC) as the critical period for TC dissociation intervention.

In the last two parts of the thesis, additional projects utilizing evoked potentials to study the ultrasound neuromodulation effect on the spinal cord and the cognitive limitations of prosthetic sensory feedback were also reported. These works are documented for archiving purposes and enlightening readers on the broad spectrum of evoked potential applications.

Motor evoked potential amplitudes were suppressed during low-frequency focused ultrasound (LIFUS) modulation and gradually recovered after modulation. The future goal of this project is to use focused ultrasound to inhibit TC neurons and to increase TC association in the acute phase of recovery after cardiac arrest.

P300 event-related potential is commonly associated with the subject's level of confidence about the category of a stimulus. When a new sensory feedback intensity was introduced, no different in force level was found, but the higher P300 amplitude in response to the novel sensory stimulation showed that the brain were able to recognize the new stimulation level. This work provides evidence that the upper limit of prosthetic sensory feedback level should be more than just three levels.

Thesis Committee

Primary Readers

Nitish V. Thakor (Primary Advisor)
Professor
Department of Biomedical Engineering
Johns Hopkins School of Medicine

Romergryko G. Geocadin
Professor
Department of Neurology, Neurosurgery, and
Anesthesiology-Critical Care Medicine
Johns Hopkins Medical Institutions

Amir Manbachi
Assistant Professor
Department of Biomedical Engineering
Johns Hopkins School of Medicine

Acknowledgments

I would like to thank my research advisor, Dr. Nitish Thakor, for his support, patience, and guidance throughout my thesis study. He has taught me the value of focus and finish, constantly writing, and communication, which I will forever cherish for my career. I would also like to thank my clinical advisor, Dr. Romgergryko Geocadin, for all the inspiring discussion on the clinical needs and applications to motivate this work. I will forever remember Dr. Amir Manbachi's open arms and offers of collaboration opportunities. I learned a great deal about ultrasound, teamwork, and data analysis through these opportunities.

Secondly, I would like to acknowledge the tremendous support from Dr. Yu Guo and Dr. Payam Gharibani, who have dedicated great amounts of time and efforts to my projects and experiments. I would like to thank Ariel Slepyan and Dr. Tray Duy Tran on all the discussion we have had on wavelet design. I would also like to thank everyone in the Neuroengineering Biomedical Instrumentation Lab, Dr. Janaka Senarathna, Catherine Ding, Denis Routkevitch, Max Kerensky, Yucheng (Jacky) Tian, Yucheng Shen, Ziwei Li, Yuhang Fu, and others for their input and support at various stages of this work.

Lastly, I would like to thank my parents, my sister, and my girlfriend for their support all these years. You gave me all the strength to chase my dream. This work could not have been possible without you.

Table of Contents

List of Tables

List of Figures

Chapter 1

Review: Evaluation of Thalamocortical Connectivity after Cardiac Arrest

1.1 Abstract

With the maturity of cardiopulmonary resuscitation (CPR) techniques and technologies, many patients were able to survive cardiac arrest but many never wake up or fully regain neurological functions. The current focus of post-cardiac arrest management has shifted to brain injury prevention, prognostication, and treatment. One of the important steps in brain injury management is the care for thalamus, as the thalamus is an important subcortical brain structure for sensation, sleep, attention, and arousal. This chapter aims to review the current understanding of thalamic injury after cardiac arrest with studies from the perspectives of blood flow, metabolism, histology, and electrophysiology. The review found that the thalamus experiences hyperremia and hyperexcitability after mild and intermediate cardiac arrest, and hyporemia and thalamocortical dissociation after severe cardiac arrest.

The review also found that we currently lack a translatable and well-validated biomarker to quantify the thalamocortical dissociation after cardiac arrest. Therefore, there is a need to develop such metric.

1.2 Introduction

Cardiac arrest is the leading cause of morbidity in the US, with more than 377,000 people experiencing out-of-hospital cardiac arrest (OHCA) each year, 90% of them fatal [1]. Cardiac arrest is defined as the cessation of cardiac mechanical activity, breathing, and consciousness. It leads to a drastic decrease in cerebral blood flow (CBF) and permanent damage of brain tissue and neurological functions [2]. In fact, neurological complication is the leading cause of disability and morbidity after OHCA survival [3]. It is believed that the recovery of the thalamus and the thalamocortical pathway is crucial to the recovery of the entire brain [4]. However, clinically, neuroprognostication has solely focused on the recovery of the cerebral cortex with techniques like electroencephalography (EEG) and somatosensory evoked potential (SSEP). This chapter aims to lay the foundation of knowledge about thalamocortical recovery after cardiac arrest and the evoked potential technique.

1.3 Neuroprognostication

Let us first review the current standard practice in clinics to monitor progress and prognosticate patients after cardiac arrest. The common cause

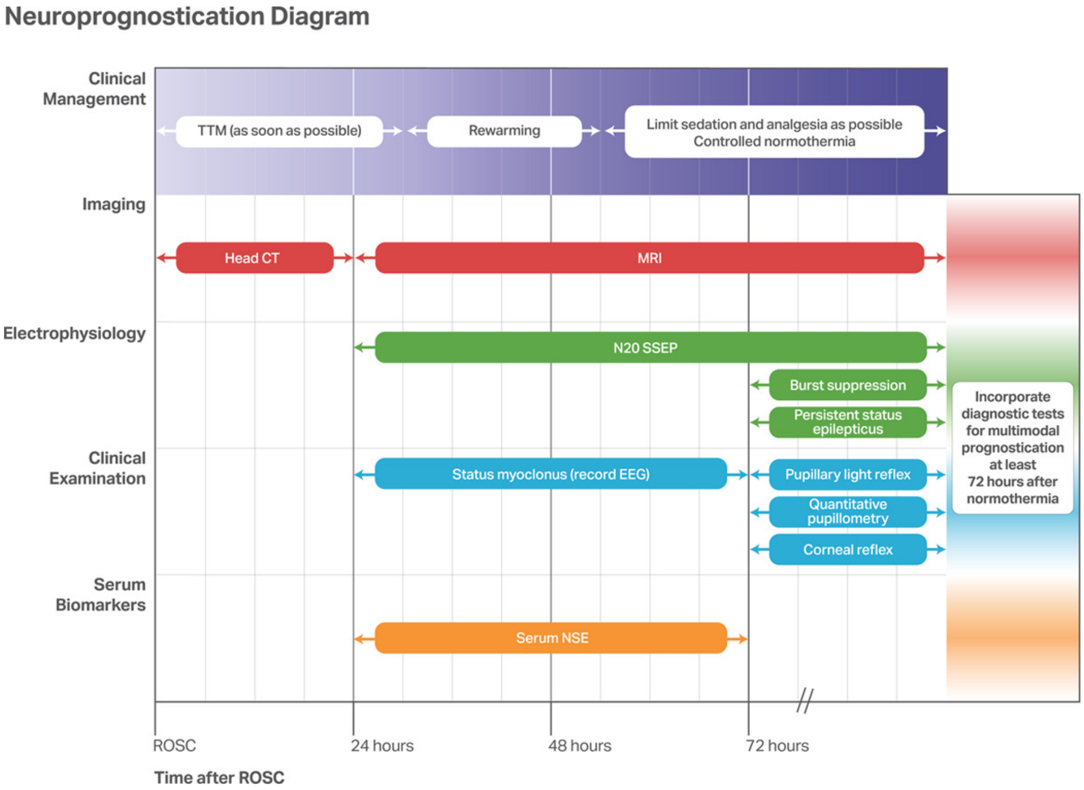

Figure 1.1: Multimodal Neuroprognostication Multimodal neuroprognostication usually consists of a series of diagnostic tests at least within 72 hours after ROSC. CT indicates computed tomography; EEG, electroencephalogram; MRI, magnetic resonance imaging; NSE, neuron-specific enolase; ROSC, return of spontaneous circulation; SSEP, somatosensory evoked potential; and TTM, targeted temperature management. (Adapted from [5])

of death among cardiac arrest survivors in comatose conditions is the withdrawal of life-sustaining therapy (WLST) [6]. Accurate prognosis can help clinicians make better WLST decisions [5]. Prognosis techniques usually includes clinical examination, EEG, SSEP, serum biomarkers, and neuroimaging technologies (Figure 1.1). However, these prognostication methods are good candidates for predicating poor neurological outcomes, but not for predicting good neurological outcomes [7]. However, if clinicians have predicted poor neurological outcome for a patient, they may spend less effort on the patient. The reduced level of care will actively affect the patient's recovery, even when the original poor neurological outcome prognosis was incorrect. Such phenomenon is called the self-fulfilling prophecy, i.e. that an originally false expectation leads to its realization [8]. If accurate metrics for positive neurological outcomes are developed, clinicians will be able to avoid the self-fulfilling prophecy and better allocate resources to save patients. Evoked potential has immense potential to become the first reliable marker for positive neurological outcomes, because it can be recorded cortically, subcortically, and in the periphery. Therefore, the rest of the chapter is dedicated to the introduction of somatosensory and motor evoked potential, and their relationships to thalamocortical connectivity.

1.4 Importance of the Thalamus

The thalamus is a group of nuclei situated in the center of the brain between the cerebral cortex and the brain stem [10]. The most well-known nuclei of the thalamus are 4 sensory relay nuclei: lateral geniculate nucleus for visual input, ventral posterolateral (VPL) and ventral posteromedial (VPM) nuclei for somatosensory input, ventral anterior and ventral ventrolateral nuclei for motor input, and medial geniculate nucleus for auditory input (Figure 1.2) [9], [11]. However, to claim the thalamus is just a sensory relay station is to sell the thalamus short. Besides the excititory thalamocortical (TC) relay neurons, another group of important neurons are the inhibitory neurons in the thalamic reticular nucleus (TRN). These neurons send axons to TC and cortical neurons and modify the information flow to the cortex [12]–[14]. The thalamus also

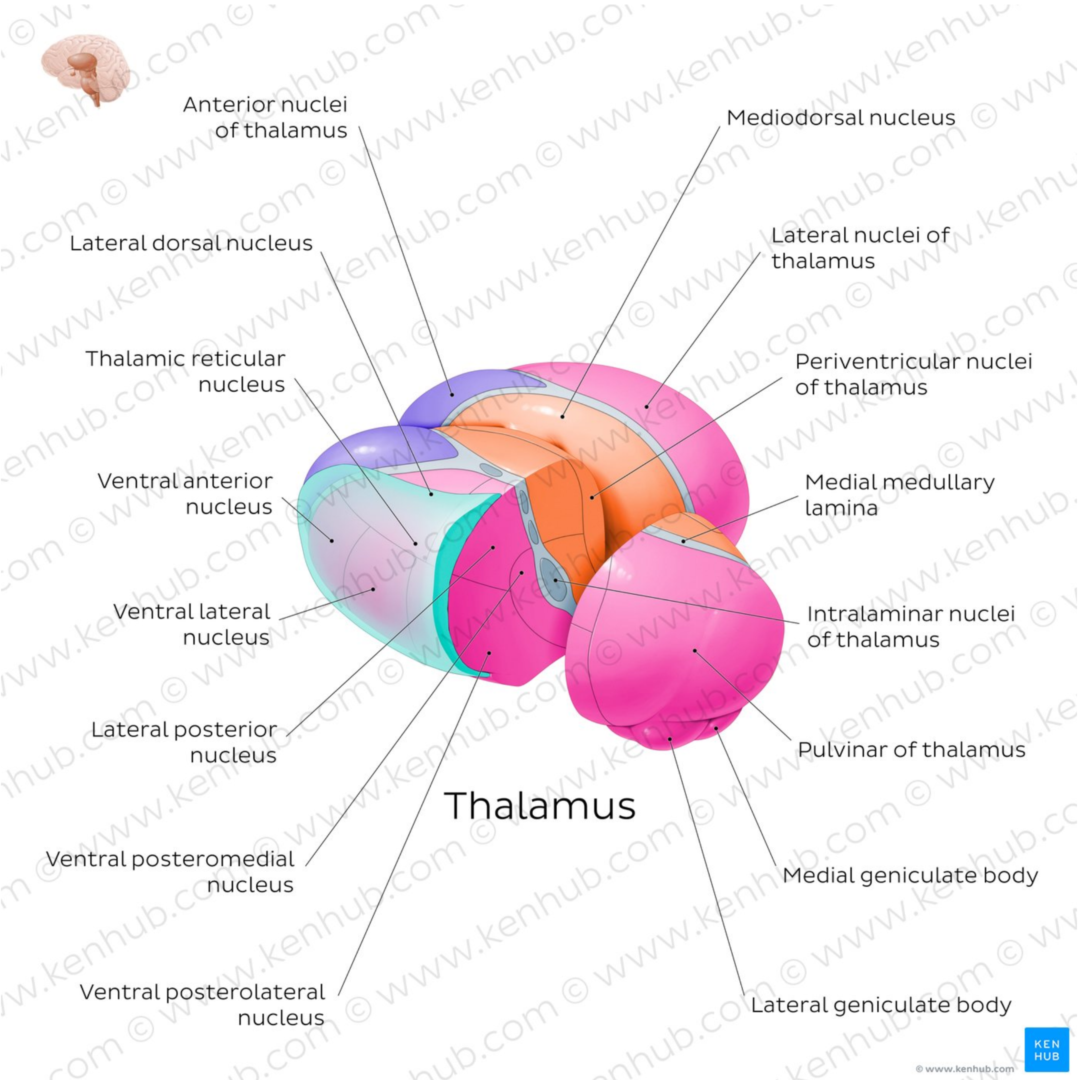

Figure 1.2: Schematic drawings of thalamic nuclei Lateral geniculate nucleus relays visual input, ventral posterolateral (VPL) and ventral posteromedial (VPM) nuclei relay somatosensory input, ventral anterior and ventral ventrolateral nuclei relay motor input, and medial geniculate nucleus relays auditory input. Thalamic reticular nucleus (TRN) modulates thalamocortical information flow. ([9])

received input from other parts of the brain and processing of information in the thalamus makes it the gatekeeper of information for the cerebral cortex [10]. Thus, the thalamus also plays important roles in the regulation of sleep, attention, and arousal [15]–[17].

1.5 Recovery of Thalamocortical Pathway after Hypoxia Ischemia

1.5.1 Thalamic Metabolism

Foley et al. (2017) measured regional cerebral blood flow (CBF) and brain oxygenation (PbO2) 24 hours after asphyxial CA in immature rats (n = 26, 6–8/group) using arterial spin label MRI and tissue electrodes, respectively [18]. 24 hours after asphyxia CA, cortical, hippocampal, and amygdalic CBF were comparable to sham CBFs, but thalamus CBF was 32% higher in CA group than sham group (283 ± 21 vs. 213 ± 6 ml/100g/min, CA vs. sham, respectively, $P < 0.05$). The study also measured PbO2 at different oxygenation concentration (FiO2 = 0.21, 0.5, 1) from the cortex and the thalamus, the two regions with the lowest and the highest post-resusitation CBF in their previous report [19]. When the subjects received high concentrations of oxygentaion (FiO2 = 0.5, 1), the PbO2 for the cortex and thalamus were above the ischemic threshold (10 mmHg) and comparable to the sham group. However, when the subjects received room air, both cortical and thalamus PbO2 dropped below the ischemic threshold and were lower compared to shams, but the difference to shams were only significant for cortical PbO2. Given their results, the authors argued that the elevated level of thalamus CBF 24 hours post-resusitation is consistent with the increased thalamus firing rate after cardiac arrest [4]. However, even though the thalamus CBF was higher in the CA group, the PbO2 was lower when room air was given, therefore further scrutinizing is needed before this argument can be perceived as correct. Furthermore, in the original thalamus firing rate paper, the authors theorized that the increase in thalamic firing was due to reduced inhibition from the RT neurons [4]. Thus, the question of which one is the dominant factor at play remains to be answered.

Putzu et al. (2018) studied the regional differences in cerebral glucose metabolism after cardiac arrest in rats with [^{18}F]fluorodeoxyglucose (FDG) positron emission tomography (PET) and autoradiography [20]. [^{18}F]FDG, a glucose analogue, is taken up and retained by cerebral cells according to energy demand [21]. Two hours after cardiac arrest and resuscitation, the rats' cerebral glucose metabolism was evaluated with PET and autoradiography. The authors found that, while the global cerebral glucose uptake decreased by more than 50% in both sham and cardiac arrest groups compared to the control group, the absolute and relative regional glucose uptake decreased significantly in cortical areas and increased significantly in deep structures like midbrain, pons, and cerebellum, comparing cardiac arrest group to sham group. They also found decreased glucose metabolism in areas like striatum, hippocampus, and thalamus, but the reduction was not statistically significant. These results indicate that after the event of cardiac arrest, cerebral glucose metabolism experienced redistribution from the neocortex to phylogenetically older structures like midbrain, pons, and the cerebellum. Therefore, based on this study, glucose supply to the thalamus is not severely affected after cardiac arrest.

A similar study was conducted by Fruscht et al. in 2004 [22]. They compared glucose metabolism in patients who developed posthypoxic myoclonus (PHM) after cardiac arrest with normal age-matched controls with FDG PET.

The patients were scanned 10.9 years after symptom onset (ranging from 4 to 25 years). The study found that PHM patients had bilateral increase in glucose metabolism in the pontine tegmentum and ventral lateral thalamus. Ventral lateral thalamus is a major relay hub for peripheral afferents, and the pontine tegmentum receives input from the motor, premotor, and somatosensory cortex. The authors suggested, in the paper, that the thalamic hypermetabolism could be related to Purkinje cell deaths in the cerebellum, which projects to the fastigial nucleus which in turn projects to the ventral lateral nucleus. This study is interesting in that it shows the long-lasting effect of cardiac arrest to the thalamus and to the patients.

1.5.2 Thalamic Neuronal Death

Sharma et al. (2011) used immunohistochemistry with light and electron microscopy to study the breakdown of the blood-brain barrier and neuronal death in different regions of the brain with a cardiac arrest porcine model [23]. The piglets were randomized into three cardiac arrest groups: no CPR, CPR with saline infusion, and CPR with methylene blue infusion. For the no CPR control group, the brains were removed for analysis 0, 5, and 30 minutes after cardiac arrest. For the two CPR groups, the brains were removed for analysis 30, 60, and 180 minutes after ROSC. After fixations in formaldehyde, brain tissues from different regions of the brain including the thalamus went through normal histology and/or immunohistochemistry. Tissues were stained with cresyl violet, hematoxylin and eosin, or Luxol Fast Blue. Immunohistochemistry for albumin, glial fibrillary acidic protein (GFAP) and myelin basic protein (MBP) was performed using monoclonal albumin, GFAP and MBP antisera [23]. Brain edema and electrolyte concentration were measured from the water content of the same tissue. The authors found breakdown of the blood-brain barrier as evidenced by the presence of albumin in the neuropil 5, 30, 60, and 180 minutes after CA, with the thalamus leading the leakage. And interestingly, the presence of albumin was very specific in the thalamus. Some areas showed massive concentration of albumin, while adjacent areas were completely void of it. Leakage of albumin also means the formation of brain edema, and the authors were able to find increasing levels of water and Na+ and Cl- concentrations in the thalamus as time increased after cardiac arrest. Traditional histology methods also showed corresponding neuron deaths in these albumin positive areas in the thalamus, which had the greatest number of neuron deaths along with the hippocampus and the cerebral cortex. They also claimed to observe heightened glial cell acitivty and myelin damage, but the quantitative result has not been published yet.

Ahn et al. (2021) studied the histopathological changes in animal model of CA in regions related to autonomic control with cresyl violet (a marker for Nissl substance), Fluoro-Jade B (a marker for neuronal death), and Iba-1 immunohistochemistry (a marker for microglial activation) [24]. They found that the earliest neuronal damage or death was found in the myelencephalon and spinal cord, before the neuronal damage in the cerebral cortex, hippocampus, thalamus, hypothalamus, and amygdala took place (Figure 1.3). In previous studies, ischemic brain damage was found in the thalamic reticular nucleus

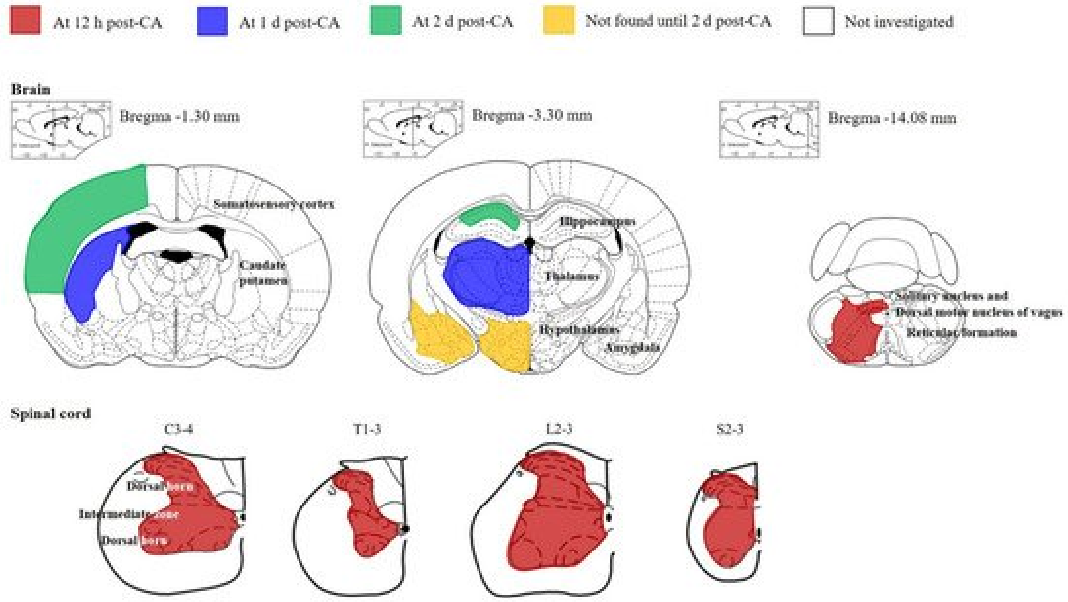

Figure 1.3: Schematic drawings of neuronal damage/death in brain and spinal cord regions related to autonomic control in the rat (Adapted from [24])

6 hours after CA by terminal deoxynucleotidyltransferase-mediated dUTP-biotin nick end-labeling (TUNEL) staining of DNA fragments [25], [26].

Instead of studying neuronal death of all types, Björklund et al. (2014) and Haglund et al. (2019) focused on selective eosinophilic neuronal death (SEND) in different brain regions after resuscitated cardiac arrest [27], [28]. The readers should be aware that SEND is probably not an immediate consequence of cardiac arrest, as it does not exist in non-resuscitated CA patients. They extracted histopathological brain sections from 6 regions of the brain from 46 CA non-survivors, and graded the level of SEND in a particular brain region on a scale of 0 to 4 based on the percentage of SEND in the in the most severely affected area of view under the microscope. They found that there was a significant difference in SEND severity across brain regions, the

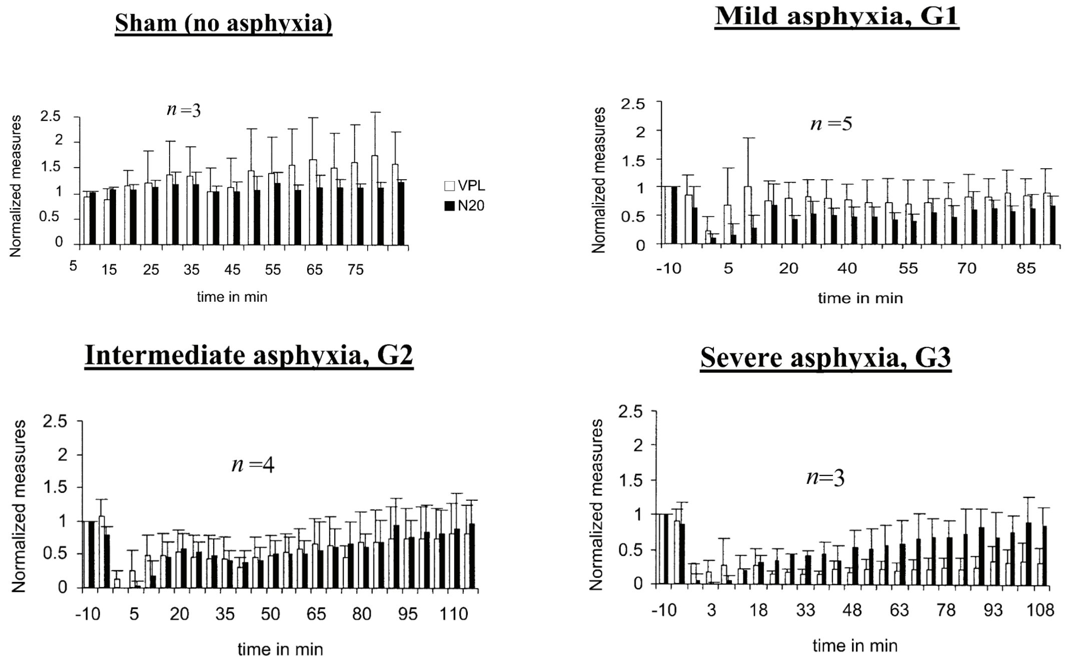

Figure 1.4: N20 and VPL ON Response (Adapted from [29])

thalamus being the most affected, and the brain stem the least affected. They also investigated the correlation between SEND severity and time to ROSC, and found significant correlation for the neocortex and basal ganglia, but not for the thalamus and other brain regions.

1.5.3 Thalamic-Somatosensory Pathway

Now, let us look at what we currently know about the recovery of the thalamo-somatosensory pathway after cardiac arrest. Muthuswamy et al. (2002) recorded SSEPs from the ventral posterior lateral (VPL) nuclei of the thalamus and the primary somatosensory cortex in order to study the differential vulnerability of the cortical and sub-cortical structures during different levels of global ischemia [29]. The VPL multi-unit responses to somatosensory stimuli usually consists of three periods: the ON response period (<30ms), the OFF period (30-100ms), and the spindle oscillation period (>100ms). It is generally believed that the ON response is generated by thalamic relay neurons to the somatosensory cortex, and the spindle oscillation is generated by the interaction between the thalamic relay and reticular thalamic neurons. Muthuswamy et al. found that the VPL ON response recovered similarly to the cortical N20 component in the mild (3min) and the intermediate (5min) asphyxia subjects, but showed different trajectories of recovery compared to the cortical N20 component in the severe asphyxia (7min) cases, indicating a thalamo-cortical dissociation after severe asphyxia. 3 out of 5 animals in severe asphyxia showed VPL suppression while N20 enjoyed gradual recoveries close to baseline levels after the return of spontaneous circulation (ROSC) (Figure 1.4). On the other hand, the spindle rhythm disappeared earlier and recovered later than the VPL ON response in mild and intermediate asphyxia, but never recovered in the severe asphyxia cases. The recovery of cortical N20 component in all three degrees of cardiac arrest indicates a resistance of the somatosensory cortex to ischemic injury, compared to the thalamus. The earlier disappearance of the spindle oscillation after asphyxia and later recovery after ROSC compared to VPL ON response seems to suggest a selective dysfunction of the VPL-RT network [29].

Shoykhet et al. (2012) did an excellent study of thalamocortical dysfunction and thalamic injury after asphyxial cardiac arrest with single neuron recordings of whisker deflection and histochemical analysis in developing rats [4] . They moved the rats' whiskers 7 degree in 8 directions and recorded

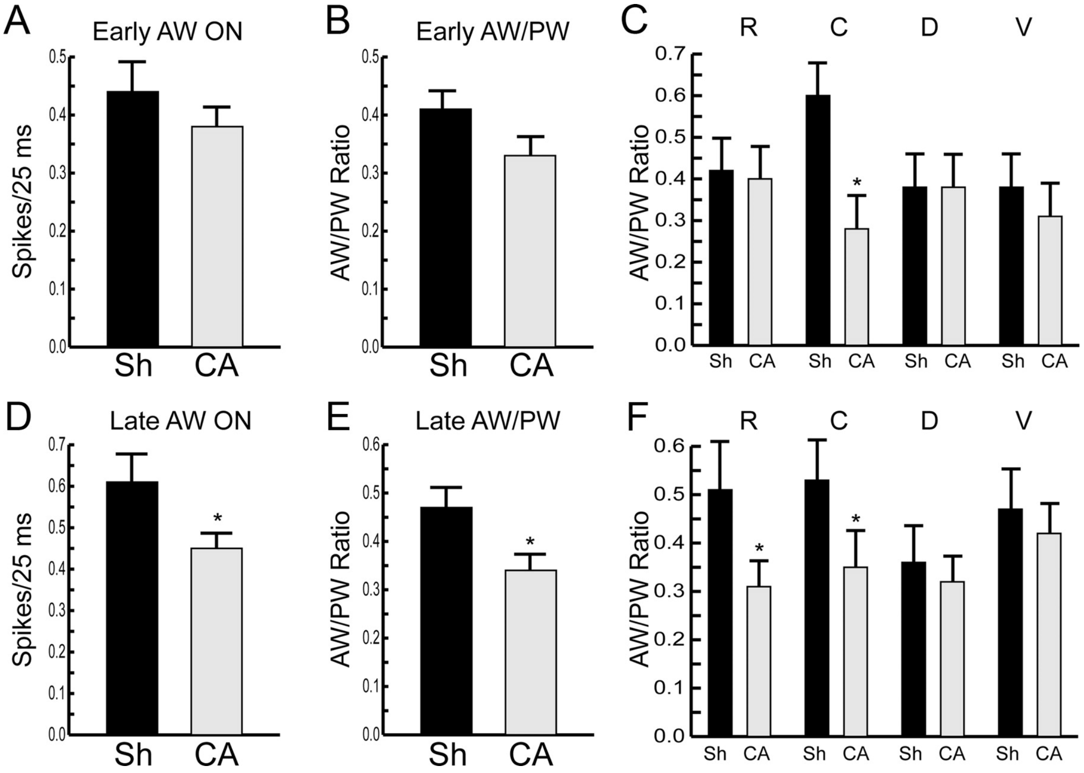

Figure 1.5: Receptive field properties of thalamocortical neurons after CA or sham insult (Adapted from [4])

single-unit activities in the ventral posterior medial (VPM) nuclei of the thalamus, and the rats were assessed either 48-72 hours after CA, or at least 6 weeks after CA. In the early-assessed group, the CA group had statistically higher spontaneous and evoked firing rates compared to the sham group. In the later group, the firing rates for some neurons stayed elevated, though to a lesser extent, for the CA group compared to the sham group. The elevated firing rate suggest possible injury to thalamic inhibitory neurons. What's more interesting is, other than studying the amplitude of neural responses, that Shoykhet et al. looked into the change in the receptive field of the VPM neurons. Each VPM neuron has a primary whisker (PW) that elicits the most robust response, and 4 adjacent whiskers (AW) — rostral, caudal, dorsal, and ventral. They found that the caudal AW response magnitude was significantly reduced in early cardiac arrest rats, compared with early shams. In the late cardiac arrest rats, the different between AW and PW responses became more prominent, with both the rostral and caudal AW responses reduced (Figure 1.5). These results suggest that the receptive field of thalamocortical neurons become more focused on the primary whisker after global ischemic injury. Suspecting that the thalamic inhibitory neurons suffered injury after cardiac arrest, the group performed histology analysis with FJB, GAD65, and Iba1. While FJB and GAD65 were not able to identify neural degeneration in RT, Iba1 found elevated activity of microglia. Collectively, these histology results suggest that the RT inhibitory neurons suffered a nonlethal injury. Lastly, they stained the thalamus with De Olmos's amino cupric silver stain, and they found selective degenration of neurites and intact soma in RT and VPM. This could explain why FJB and GAD65 did not work.

1.5.4 Strato-pallidal-thalamo-cortical Pathway

Following their electrophysiology recordings in the thalamus [4], Aravamuthan and Shoykhet (2015) went ahead and studied the effect of cardiac arrest on the basal ganglia and the motor cortex with electrophysiology [30]. They simultaneously recorded local field potential (LFP) from the motor cortex, and LFP and single-neuro spikes from the rat entopeduncular nucleus (EPN). EPN is equivalent to the primate globus pallidus pars interna. Although this study did not directly focus on the recovery of the thalamus after cardiac arrest, it is related to the thalamus through the basal ganglia-thalamo-cortical motor network. EPN sends its output through the ventral lateral thalamic nucleus to the motor cortex [31], [32] and is modulated by the inhibitory thalamic reticular nucleus [33], [34]. In this study, they found increased coherence between EPN spike and motor cortex LFP, but decreased coherence between EPN LFP and motor cortex LFP after cardiac arrest compared to the sham condition. Since LFP mostly reflect synaptic input activity [35] and spike is the output activity, the authors explained that shared input to both structures decreased after cardiac arrest, but input from EPN to the cortex is more coherent probably due to less inhibition from the thalamic reticular nucleus [4].

Shoykhet and Middleton (2016) published a follow-up study on the same two datasets [36]. They examined the effect of global ischemia during development on spontaneous and evoked firing of somatosensory and motor thalamocortical neurons in adulthood. They found that the VPM spontaneous and evoked firing rate were lower and correlated with the whisker-evoked firing rate in sham rats, but not in cardiac arrest rats, even after the rats progressed into adulthood. They argue that abnormal thalamus firing patterns might had affected the organization of cortical circuitry in adulthood. Previously in [30], the authors reported decreased coherence between EPN and MCx LFP after cardiac arrest. In this study, they extended the finding by showing that, in sham rats, the normalized total power of EPN LFP covaries with that of MCx LFP in multiple frequency ranges. However, such covariation was not observed in CA rats except in the low θ frequency.

In the latest publication from the same group, Ton et al. (2021) developed

11-min and 12-min cardiac arrest rat model and applied 34 °C mild hypothermia as a form of therapy for 8 hours to a 12.5-min cohort [37]. They then studied the extent of microglial activation and neuronal degeneration in the thalamus with anti-Iba1 antibody, amino cupric silver, and Gad67. They discovered that the most injured area in the thalamus is the thalamic reticular nucleus. The percent of RT area covered by Iba1 and CuAg staining increased respectively as arrest duration increased [37]. CuAg staining localized the degeneration to neuronal somata and synaptic terminals in RT. Furthermore, their result of mild hypothermia in the 12.5-min cohort suggests that mild hypothermia cannot prevent injury to the RT. They further characterized their result by classified the RT into the anterior salient, the intermediate somatosensory, and the posterior auditory segments and discovered that only the intermediate and posterior segments were selectively injured, even though the entire RT consists solely of inhibitory GABA-ergic neurons [38]. Thus, the neuronal type along could not explain the selective vulnerability of RT in the entire thalamus. To confirm this result, the authors also studied the characteristics of cortical GABA-ergic neurons after cardiac arrest, and found no significant difference in the number of GAD67 + neurons in the motor, somatosensory, and auditory cortices.

A recent human MRI study also confirmed the vulnerability of the striato-pallidal-thalamo-cortical pathway after cardiac arrest. Silva et al. (2017) calculated cortical thickness and deep gray matter volumetry of cardiac arrest survivors and controls [39]. With regards to subcortical changes, the authors found that basal ganglia, thalamus, and brain stem volumes of coma patients were significantly lower than those of control. Interestingly, the authors performed principle component analysis (PCA) on the whole dataset and found that CA-induced cortical and subcortical injuries take place independently.

1.6 Discussion

As a summary, all studies of thalamic injury after CA discussed in Section 1.5 are tabulated into Tables 1.1, 1.2, 1.3.

After mild and intermediate CA, thalamus would experience hyperemia in the acute phase of recovery [18], [19], but the opposite is true for severe CA: initial hyperemia was not observed and hypoperfusion was present 60 minutes after ROSC [19]. In addition, thalamic autoregulation was absent in severe CA cases [19]. One of our group's recent publications shows that early thalamocortical reperfusion is associated with neurological outcomes at 24 h [43]. Though not mechanistic studies, these reports showed the different recovery trajectories of thalamic blood flow after different intensities of cardiac arrest and the importance of early reperfusion to functional recovery. Thus, future translational studies on blood flow and autoregulation of the thalamus after cardiac arrest could target inducing initial hyperemia in severe CA cases.

In terms of thalamic glucose metabolism after cardiac arrest, the two studies cited reported contradictory results [20], [22]. Thus, more studies are necessary before conclusion can be drawn on the thalamic glucose metabolism trajectory after cardiac arrest.

While thalamic blood flow only showed serious damage in the severe CA cases, thalamic neuronal damage was obvious across all levels of injuries [4],

[23]–[29], [37], [40]. Especially worth paying attention to is the selective vulnerability of the inhibitory thalamic reticular nucleus (TRN) neurons [4], [29], [37], [44]. TRN neurons forms a closed loop with and inhibit thalamocortical (TC) neurons, thus modulating TC neuron activities and generating spindle oscillations [14]. The increased blood flow and damaged inhibitory TRN neurons could be the explanations for the increased thalamocortical neuronal activity and the disappearance of rhythmic spindles after cardiac arrest [4], [29]. Such elevated spontaneous and evoked firings of TC neurons after CA may not be desired as they could lead to excitotoxicity and cell death further down the road [45].

Electrophysiology recordings such as somatosensory evoked potentials (SSEPs) and local field potentials (LFPs) in the thalamus were also used to evaluate the functional properties of the thalamus after cardiac arrest [4], [29], [30], [40]–[42], [44]. TC neurons showed elevated levels of firing after CA [4], but cortically recorded SSEPs showed a different recovery trajectory in the severe CA cases [29], [44], thus suggesting an thalamocortical dissociation after CA. More recently, our group has attemped to quantify this thalamocortical dissociation with advanced signal processing methods such as direct Directed Transfer Function and Granger Causality [41], [42]. However, these studies reported elevated levels of association between the thalamus and the cortex in the immediate phase after CA, deviating from the earlier hypothesis of thalamocortical dissociation. Thus, a thalamocortical dissociation biomarker that is more compatible with histology and electrophysiology evidence is necessary to aid our understanding of thalamic injury and our attempt to identify effective interventions after CA.

1.7 Conclusion

Thalamus is crucial for good neurological outcomes after CA because it is associated with sensory relay, sleep, attention, and arousal. Blood flow, histology, and electrophysiology evidence has shown that the thalamus is vulnerable to ischemic injury after CA, but there exists no bedside monitoring tool to quantify the injury level nor effective intervention. Thus, there is a need to develop effective biomarkers to inform clinicians of thalamic injury level and aid researchers in identifying potential treatments.

Table 1.1: Summary of thalamic injury after cardiac arrest studies

Study Types	Subject	CA Modality & Duration	Methods	Findings
Blood Flow	Male Sprague Dawley rats, postnatal day 16-18	Asphyxia, 9 minutes	Arterial spin labeling (ASL) magnetic resonance imaging (MRI) for cerebral blood flow (CBF), tissue electrode for PbO2	Thalamic CBF was 32% higher after CA vs. sham at 24 h. CBF of other regions all recovered to sham levels by 24 h. [18]
Blood Flow	Male Sprague Dawley rats, postnatal day 16-18	Asphyxia, 8.5-12 minutes	ASL-MRI, mean arterial pressure (MAP) manipulation via epinephrine	Thalamic CBF displayed early hyperemia in the 8.5 and 9 min asphyxia groups at 5 mins after ROSC (204% and 188% of baseline, respectively, $P < 0.05$), and subsequently decreased to baseline values 10 and 60 min after ROSC, respectively. In the 12 mins, asphyxia group initial hyperemia was not observed and thalamic CBF displayed hypoperfusion from 60 mins after ROSC, reaching a nadir of 62% baseline at 150 mins. No thalamic autoregulation 60 minutes after 12 min CA. [19]
Metabolism	Male Sprague Dawley rats, adult	Potassium chloride and esmolol, 8 minutes	[^{18}F]fluorodeoxyglucose (FDG) autoradiography and positron emission tomography	Thalamus showed no significant change in absolute glucose metabolism level 2 h after CA. Relative metabolism indicated a redistribution from the cortex to brainstem and cerebellum. [20]
Metabolism	Patients with posthypoxic myoclonus after CA, 47 ± 10 years	N/A	FDG-PET, MRI	Significant bilateral increase in glucose metabolism in the ventrolateral thalamus in patients compared to controls. [22]
Brain Volume	Coma patients, 16 ± 8 days after CA	N/A	MRI	Basal ganglia, thalamus, and brain stem volumes of coma patients were significantly lower than those of control. [39]

Table 1.2: Summary of thalamic injury after cardiac arrest studies (continued)

Study Types	Subject	CA Modality & Duration	Methods	Findings
Histology	Piglets, 12-14 weeks	Ventricular fibrillation, 12 minutes	Immunohistochemistry for albumin, glial fibrillary acidic protein (GFAP) and myelin basic protein (MBP)	Thalamus showed the most progressive neuronal, glial, and myelin damage from 5 to 180 minutes after CA. [23]
Histology	Male Sprague Dawley rats, 16 weeks	Asphyxia, 5 minutes	Cresyl Violet (CV), FJB staining, Iba-1 immunoreactivity	The earliest neuronal damage or death was found in the myelencephalon and spinal cord, before the neuronal damage in the cerebral cortex, hippocampus, thalamus, hypothalamus, and amygdala took place. [24]
Histology	Male Sprague Dawley rats, adult	Asphyxia, 8 minutes	H&E staining	Thalamus showed the second highest histopathological damage after hippocampus evaluated at 24 h after CA. [25]
Histology	Long Evans rats, postnatal days 17-19	Asphyxia, 11-12 minutes	amino cupric silver for neuronal degeneration, anti-Iba1 antibody for microglia, anti-Gad67 antibody for inhibitory neurons	They discovered that the most injured area in the thalamus is the anterior and intermediate segments of the thalamic reticular nucleus. The percent of TRN area covered by Iba1 and CuAg staining increased respectively as arrest duration increased. [37]
Histology	Male Sprague Dawley rats, adult	Ventricular fibrillation, 10 minutes	Terminal deoxynucleotidyltransferase-mediated dUTP-biotin nick end-labeling (TUNEL)	Thalamic reticular nucleus (TRN) showed an early onset of degeneration at 6 h after CA and peaked at 3 days by TUNEL. [26]
Histology	Non-survivor patients of cardiac arrest treated with hypothermia	N/A	Brain autopsy microscopic slides and selective eosinophilic neuronal death (SEND) quantification	Thalamus exhibited intermediate SEND vulnerability. [27]
Histology	Non-survivor patients of cardiac arrest treated with hypothermia	N/A	Brain autopsy microscopic slides and selective eosinophilic neuronal death (SEND) quantification	Thalamus exhibited severe SEND vulnerability. [28]

Table 1.3: Summary of thalamic injury after cardiac arrest studies (continued)

Study Types	Subject	CA Modality & Duration	Methods	Findings
Electrophysiology & Histology	Male Sprague Dawley rats, postnatal day 17-19	Asphyxia, 9 minutes	Whisker deflection and SSEP, Glutamic acid decarboxylase (GAD), cytochrome oxidase (CO), Fluoro-Jade B (FJB) staining	48 –72 h after cardiac arrest, thalamocortical neurons demonstrate significantly elevated firing rates both during spontaneous activity and in response to whisker deflections. The elevated evoked firing rates persist for at least 6 – 8 weeks after injury. Despite the overall increase in firing, by 6 weeks, thalamocortical neurons display degraded receptive fields, with decreased responses to adjacent whiskers. Extensive degeneration of neurites in the somatosensory nucleus as well as activation of microglia in the reticular nucleus. [4]
Electrophysiology & Histology	Male Wistar rats, adult	Asphyxia, 3-7 minutes	EEG, EP, local field potential (LFP), multi-unit activities (MUA)	The ventraposterior lateral nucleus (VPL) ON response recovered similarly to the cortical N20 component in the mild (3min) and the intermediate (5min) asphyxia subjects, but showed different trajectories of recovery compared to the cortical N20 component in the severe asphyxia (7min) cases, indicating a thalamo-cortical dissociation after severe asphyxia. The spindle rhythm disappeared earlier and recovered later than the VPL ON response in mild and intermediate asphyxia, but never recovered in the severe asphyxia cases. [29]
Electrophysiology & Histology	Non-survivor patients of cardiac arrest		EEG, SSEP, H&E staining	Absent SSEP responses were always accompanied by thalamic damage. In patients with additional thalamic involvement, burst-suppression with identical bursts was observed. [40]
Electrophysiology	Male Sprague Dawley rats, postnatal 3 weeks	Asphyxia, 9.5 minutes	LFP, single-neuron firing	Basal ganglia entopeduncular nucleus (EPN) firing rate is lower in cardiac arrest survivors (19.5±2.4 Hz) compared with controls (27.4±2.7 Hz; $P < 0.05$). Cardiac arrest survivors also demonstrate greater coherence between EPN single neurons and motor cortex LFP (3—100 Hz; $P < 0.001$). [30]
Electrophysiology	Male Wistar rats, adult	Asphyxia, 5 minutes	LFP	direct Directed Transfer Function between somatosensory cortex and thalamic VPL LFPs in both directions increased in the acute phase of recovery after CA. [41]
Electrophysiology	Male Sprague Dawley rats, adult	Asphyxia, 5 minutes	LFP	Granger causality from thalamic VPL LFP to somatosensory cortex LFP increased in the acute phase of recovery after CA. [42]

References

[1] S. S. Virani, A. Alonso, H. J. Aparicio, E. J. Benjamin, M. S. Bittencourt, C. W. Callaway, A. P. Carson, A. M. Chamberlain, S. Cheng, F. N. Delling, *et al.*, "Heart disease and stroke statistics—2021 update: A report from the american heart association," *Circulation*, vol. 143, no. 8, e254–e743, 2021.

[2] I. Jacobs, V. Nadkarni, I. T. F. on Cardiac Arrest, C. R. Outcomes, C. PARTICIPANTS, J. Bahr, R. A. Berg, J. E. Billi, L. Bossaert, P. Cassan, A. Coovadia, *et al.*, "Cardiac arrest and cardiopulmonary resuscitation outcome reports: Update and simplification of the utstein templates for resuscitation registries: A statement for healthcare professionals from a task force of the international liaison committee on resuscitation (american heart association, european resuscitation council, australian resuscitation council, new zealand resuscitation council, heart and stroke foundation of canada, interamerican heart foundation, resuscitation councils of southern africa)," *Circulation*, vol. 110, no. 21, pp. 3385–3397, 2004.

[3] P. Vaagenes, M. Ginsberg, U. Ebmeyer, L. Ernster, M. Fischer, S.-E. Gisvold, A. Gurvitch, K. A. Hossmann, E. M. Nemoto, A. Radovsky, *et al.*, "Cerebral resuscitation from cardiac arrest: Pathophysiologic mechanisms," *Critical care medicine*, vol. 24, no. 2, 57S–68S, 1996.

[4] M. Shoykhet, D. J. Simons, H. Alexander, C. Hosler, P. M. Kochanek, and R. S. Clark, "Thalamocortical dysfunction and thalamic injury after asphyxial cardiac arrest in developing rats," *Journal of Neuroscience*, vol. 32, no. 14, pp. 4972–4981, 2012.

[5] A. R. Panchal, J. A. Bartos, J. G. Cabañas, M. W. Donnino, I. R. Drennan, K. G. Hirsch, P. J. Kudenchuk, M. C. Kurz, E. J. Lavonas, P. T. Morley, *et al.*, "Part 3: Adult basic and advanced life support: 2020 american heart association guidelines for cardiopulmonary resuscitation and emergency cardiovascular care," *Circulation*, vol. 142, no. 16_Suppl_2, S366–S468, 2020.

[6] J. Elmer, C. Torres, T. P. Aufderheide, M. A. Austin, C. W. Callaway, E. Golan, H. Herren, J. Jasti, P. J. Kudenchuk, D. C. Scales, *et al.*, "Association of early withdrawal of life-sustaining therapy for perceived neurological prognosis with mortality after cardiac arrest," *Resuscitation*, vol. 102, pp. 127–135, 2016.

[7] B. Lachance, Z. Wang, N. Badjatia, and X. Jia, “Somatosensory evoked potentials and neuroprognostication after cardiac arrest,” *Neurocritical care*, vol. 32, no. 3, pp. 847–857, 2020.

[8] R. G. Geocadin, M. A. Peberdy, and R. M. Lazar, “Poor survival after cardiac arrest resuscitation: A self-fulfilling prophecy or biologic destiny?” *Critical care medicine*, vol. 40, no. 3, pp. 979–980, 2012.

[9] G. Sandic. (2022). “Thalamic nuclei,” [Online]. Available: `https://www.kenhub.com/en/library/anatomy/thalamic-nuclei` (visited on 08/10/2022).

[10] S. M. Sherman and R. W. Guillery, *Exploring the thalamus and its role in cortical function*. MIT press, 2006.

[11] S. M. Sherman and R. Guillery, “The role of the thalamus in the flow of information to the cortex,” *Philosophical Transactions of the Royal Society of London. Series B: Biological Sciences*, vol. 357, no. 1428, pp. 1695–1708, 2002.

[12] J. W. Crabtree, “Functional diversity of thalamic reticular subnetworks,” *Frontiers in systems neuroscience*, vol. 12, p. 41, 2018.

[13] R. Guillery, S. Feig, and D. Lozsadi, “Paying attention to the thalamic reticular nucleus,” *Trends in neurosciences*, vol. 21, no. 1, pp. 28–32, 1998.

[14] D. Pinault, “The thalamic reticular nucleus: Structure, function and concept,” *Brain research reviews*, vol. 46, no. 1, pp. 1–31, 2004.

[15] J. E. Jan, R. J. Reiter, M. B. Wasdell, and M. Bax, “The role of the thalamus in sleep, pineal melatonin production, and circadian rhythm sleep disorders,” *Journal of pineal research*, vol. 46, no. 1, pp. 1–7, 2009.

[16] K. McAlonan, J. Cavanaugh, and R. H. Wurtz, “Guarding the gateway to cortex with attention in visual thalamus,” *Nature*, vol. 456, no. 7220, pp. 391–394, 2008.

[17] Y. D. Van der Werf, M. P. Witter, and H. J. Groenewegen, “The intralaminar and midline nuclei of the thalamus. anatomical and functional evidence for participation in processes of arousal and awareness,” *Brain research reviews*, vol. 39, no. 2-3, pp. 107–140, 2002.

[18] L. M. Foley, R. S. Clark, A. L. Vazquez, T. K. Hitchens, H. Alexander, C. Ho, P. M. Kochanek, and M. D. Manole, “Enduring disturbances in regional cerebral blood flow and brain oxygenation at 24 h after asphyxial cardiac arrest in developing rats,” *Pediatric research*, vol. 81, no. 1, pp. 94–98, 2017.

[19] M. D. Manole, L. M. Foley, T. K. Hitchens, P. M. Kochanek, R. W. Hickey, H. Bayir, H. Alexander, C. Ho, and R. S. Clark, “Magnetic resonance imaging assessment of regional cerebral blood flow after asphyxial cardiac arrest in immature rats,” *Journal of Cerebral Blood Flow & Metabolism*, vol. 29, no. 1, pp. 197–205, 2009.

[20] A. Putzu, S. Valtorta, G. Di Grigoli, M. Haenggi, S. Belloli, A. Malgaroli, M. Gemma, G. Landoni, L. Beretta, and R. M. Moresco, “Regional differences in cerebral glucose metabolism after cardiac arrest and resuscitation in rats using [18 f] fdg positron emission tomography and autoradiography,” *Neurocritical care*, vol. 28, no. 3, pp. 370–378, 2018.

[21] M. Reivich, D Kuhl, A Wolf, J Greenberg, M. a. Phelps, T Ido, V Casella, J Fowler, E Hoffman, A Alavi, *et al.*, “The [18f] fluorodeoxyglucose method for the measurement of local cerebral glucose utilization in man.,” *Circulation research*, vol. 44, no. 1, pp. 127–137, 1979.

[22] S. J. Frucht, M. Trošt, Y. Ma, and D. Eidelberg, “The metabolic topography of posthypoxic myoclonus,” *Neurology*, vol. 62, no. 10, pp. 1879–1881, 2004.

[23] H. S. Sharma, A. Miclescu, and L. Wiklund, “Cardiac arrest-induced regional blood–brain barrier breakdown, edema formation and brain pathology: A light and electron microscopic study on a new model for neurodegeneration and neuroprotection in porcine brain,” *Journal of neural transmission*, vol. 118, no. 1, pp. 87–114, 2011.

[24] J. H. Ahn, T.-K. Lee, H.-J. Tae, B. Kim, H. Sim, J.-C. Lee, D. W. Kim, Y. S. Kim, M. C. Shin, Y. Park, *et al.*, “Neuronal death in the cns autonomic control center comes very early after cardiac arrest and is not significantly attenuated by prompt hypothermic treatment in rats,” *Cells*, vol. 10, no. 1, p. 60, 2021.

[25] L. Katz, U. Ebmeyer, P. Safar, A. Radovsky, and R. Neumar, “Outcome model of asphyxial cardiac arrest in rats,” *Journal of Cerebral Blood Flow & Metabolism*, vol. 15, no. 6, pp. 1032–1039, 1995.

[26] B. W. Böttiger, B. Schmitz, C. Wiessner, P. Vogel, and K.-A. Hossmann, “Neuronal stress response and neuronal cell damage after cardiocirculatory arrest in rats,” *Journal of Cerebral Blood Flow & Metabolism*, vol. 18, no. 10, pp. 1077–1087, 1998.

[27] E. Björklund, E. Lindberg, M. Rundgren, T. Cronberg, H. Friberg, and E. Englund, “Ischaemic brain damage after cardiac arrest and induced hypothermia–a systematic description of selective eosinophilic neuronal death. a neuropathologic study of 23 patients,” *Resuscitation*, vol. 85, no. 4, pp. 527–532, 2014.

[28] M. Haglund, E. Lindberg, and E. Englund, “Hippocampus and basal ganglia as potential sentinel sites for ischemic pathology after resuscitated cardiac arrest,” *Resuscitation*, vol. 139, pp. 230–233, 2019.

[29] J. Muthuswamy, T Kimura, M. Ding, R Geocadin, D. Hanley, and N. Thakor, “Vulnerability of the thalamic somatosensory pathway after prolonged global hypoxic–ischemic injury,” *Neuroscience*, vol. 115, no. 3, pp. 917–929, 2002.

[30] B. R. Aravamuthan and M. Shoykhet, “Long-term increase in coherence between the basal ganglia and motor cortex after asphyxial cardiac arrest and resuscitation in developing rats,” *Pediatric research*, vol. 78, no. 4, pp. 371–379, 2015.

[31] L.-N. Hazrati and A. Parent, “Contralateral pallidothalamic and pallidotegmental projections in primates: An anterograde and retrograde labeling study,” *Brain research*, vol. 567, no. 2, pp. 212–223, 1991.

[32] A. Parent and L. De Bellefeuille, “Organization of efferent projections from the internal segment of globus pallidus in primate as revealed by flourescence retrograde labeling method,” *Brain research*, vol. 245, no. 2, pp. 201–213, 1982.

[33] M. D. Humphries and K. Gurney, “The role of intra-thalamic and thalamocortical circuits in action selection,” *Network: Computation in Neural Systems*, vol. 13, no. 1, pp. 131–156, 2002.

[34] S. N. Haber and R. Calzavara, “The cortico-basal ganglia integrative network: The role of the thalamus,” *Brain research bulletin*, vol. 78, no. 2-3, pp. 69–74, 2009.

[35] G. T. Einevoll, C. Kayser, N. K. Logothetis, and S. Panzeri, “Modelling and analysis of local field potentials for studying the function of cortical circuits,” *Nature Reviews Neuroscience*, vol. 14, no. 11, pp. 770–785, 2013.

[36] M. Shoykhet and J. W. Middleton, “Cardiac arrest-induced global brain hypoxia-ischemia during development affects spontaneous activity organization in rat sensory and motor thalamocortical circuits during adulthood,” *Frontiers in neural circuits*, vol. 10, p. 68, 2016.

[37] H. T. Ton, K. Raffensperger, and M. Shoykhet, "Early thalamic injury after resuscitation from severe asphyxial cardiac arrest in developing rats," *Frontiers in Cell and Developmental Biology*, p. 3521, 2021.

[38] E. G. Jones, "Thalamic circuitry and thalamocortical synchrony," *Philosophical Transactions of the Royal Society of London. Series B: Biological Sciences*, vol. 357, no. 1428, pp. 1659–1673, 2002.

[39] S. Silva, P. Peran, L. Kerhuel, B. Malagurski, N. Chauveau, B. Bataille, J. A. Lotterie, P. Celsis, F. Aubry, G. Citerio, *et al.*, "Brain gray matter mri morphometry for neuroprognostication after cardiac arrest," *Critical care medicine*, vol. 45, no. 8, e763, 2017.

[40] M. J. van Putten, C. Jansen, M. C. Tjepkema-Cloostermans, T. M. Beernink, R. Koot, F. Bosch, A. Beishuizen, and J. Hofmeijer, "Postmortem histopathology of electroencephalography and evoked potentials in postanoxic coma," *Resuscitation*, vol. 134, pp. 26–32, 2019.

[41] D. Wu, A. Bezerianos, D. Sherman, X. Jia, and N. V. Thakor, "Causal interactions between thalamic and cortical lfps following hypoxic-ischemic brain injury," in *2011 5th International IEEE/EMBS Conference on Neural Engineering*, IEEE, 2011, pp. 184–187.

[42] C. Chen, A. Maybhate, D. Israel, N. V. Thakor, and X. Jia, "Assessing thalamocortical functional connectivity with granger causality," *IEEE Transactions on Neural Systems and Rehabilitation Engineering*, vol. 21, no. 5, pp. 725–733, 2013.

[43] Y. Guo, S.-M. Cho, Z. Wei, Q. Wang, H. R. Modi, P. Gharibani, H. Lu, N. V. Thakor, and R. G. Geocadin, "Early thalamocortical reperfusion leads to neurologic recovery in a rodent cardiac arrest model," *Neurocritical care*, pp. 1–13, 2022.

[44] R. G. Geocadin, J. Muthuswamy, D. L. Sherman, N. V. Thakor, and D. F. Hanley, "Early electrophysiological and histologic changes after global cerebral ischemia in rats," *Movement disorders*, vol. 15, no. S1 S1, pp. 14–21, 2000.

[45] M. P. Goldberg, J. H. Weiss, P. Pham, and D. Choi, "N-methyl-d-aspartate receptors mediate hypoxic neuronal injury in cortical culture.," *Journal of Pharmacology and Experimental Therapeutics*, vol. 243, no. 2, pp. 784–791, 1987.

Chapter 2

Methods: Somatosensory Evoked Potential Analysis

2.1 Abstract

Based on the review in the previous chapter, electrophysiology studies based on somatosensory evoked potentials (SSEPs) and local field potentials (LFPs) demonstrated thalamocortical dissociation after cardiac arrest, but a proper metric to quantify the dissociation does not exist. Thus, this chapter hopes to review current SSEP analysis methods to identify potential breakthroughs to develop bedside monitoring method. This chapter first familiarize readers with the technique of SSEPs, then to review advance SSEP analysis methods, and lastly to introduce the two coupling measures previously tested. The review found that in order to develop noninvasive coupling biomarker, a method to extract subcortical activity from noninvasive recording is needed. The method identified in this case is multiresolution wavelet (MRW) analysis. This chapter proposes a two-step approach to quantify thalamocotical dissociation after cardiac arrest: MRW to extract subcortical activity, and Granger

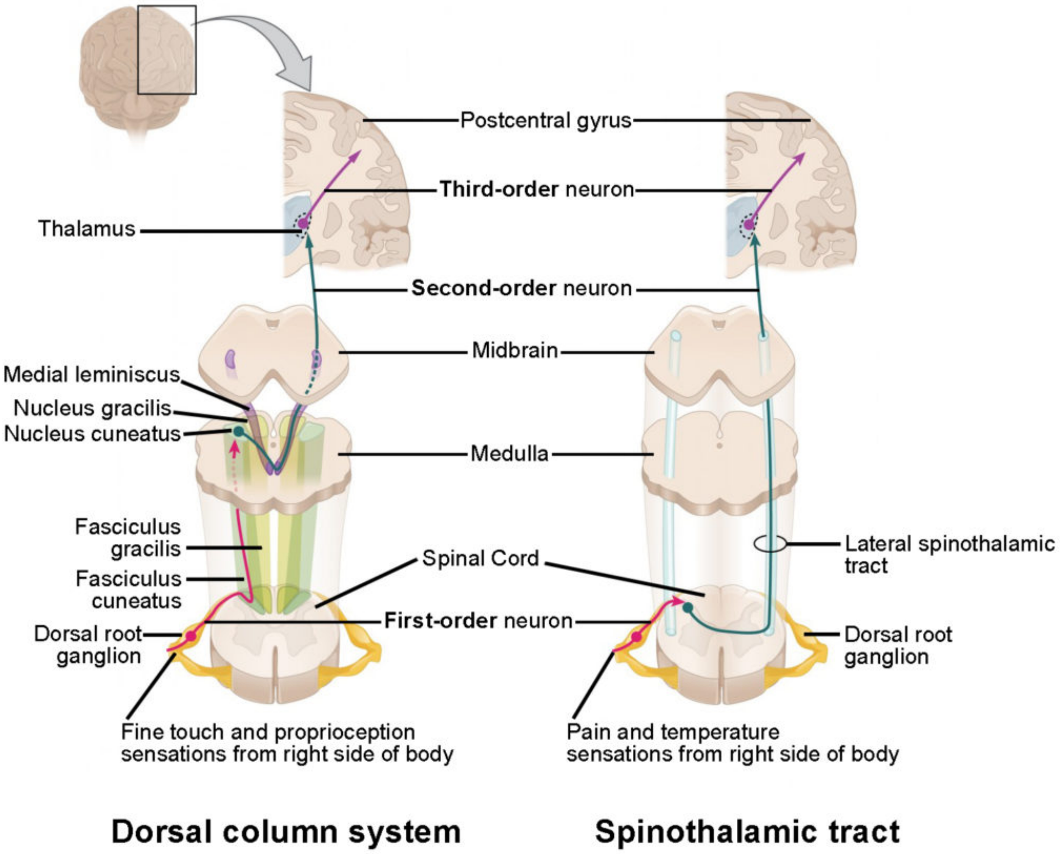

Figure 2.1: Spinal Ascending Pathways The dorsal column system and spinothalamic tract are the major ascending pathways that connect the periphery with the brain (Adapted from [1]).

causality to quantify the coupling betwen subcortical and cortical activities.

2.2 Somatosensory Evoked Potential

The somatosensory nervous system contains three subsystems: one subsystem that transmits information about touch, vibration, and pressure from cutaneous mechanoreceptors, one that transmits information about position of our body, and the last one that transmits information about pain and temperature . The pseudounipolar neurons in the dorsal root ganglion outside

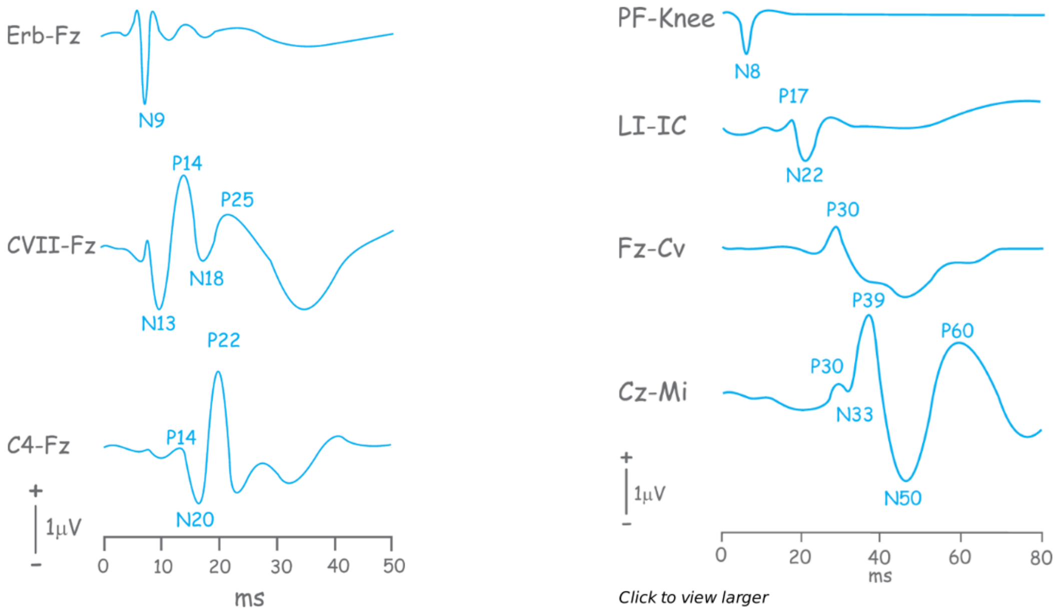

(a) Median Nerve

(b) Posterior Tibial Nerve

Figure 2.2: Somatosensory Evoked Potentials in Human (a) stimulation of the left median nerve. (b) stimulation of the posterior tibial nerve. (Adapted from [3]).

of the spinal cord give rises to a peripheral and a central processes. The peripheral processes branch within the skin and form mechanoreceptors and free nerve endings. The central processes synapse in the spinal cord or in the brain stem. Mechanoreceptors in the skin, muscle, and tendons transduce mechanical stimulus into electric signal and sends it along the somatosensory afferents into the dorsal column of the spinal cord and synapse in the dorsal column nuclei in the medulla. The second-order neurons in the medulla send their axons across the midline to the contralateral ventral posterior lateral and medial nuclei in the thalamus. Lastly, third-order neurons in the thalamus send their axons to the ipsilateral primary somatosensory cortex, or S1 (Figure 2.1) [2].

As action potentials travel from the periphery through the spinal cord, pass the subcortical regions, and finally into the cortex, SSEP can be recorded along the entire somatosensory pathway (Figure 2.2). Although SSEP can be generated by mechanical stimuli to the skin, it is typically elicited by electric stimulation of peripheral nerves, circumventing the complex interaction between external stimuli with the skin and mechanoreceptors [3]–[6].

The standard practice to elicit SSEP is to place a bipolar surface electrode at the wrist and stimulate with a frequency of 4.7 or 5 Hz and a stimulus duration of 0.2 ms [7]. Ag/AgCl recording electrodes can be placed at the Erb's point, behind the neck, and C3' and C4', 1.5 cm posterior to C3 and C4, on the scalp [3]. Recordings are time-locked to the onset of stimulus and averaged together to produce the evoked potential trace. Averaging will keep the amplitude of the signal and reduce the amplitude of the noise, thus increasing the signal-to-noise ratio (SNR). To be more precise, the SNR increases linearly with the square root of the number of trials [8]

In humans, stimulation of the median nerve can elicit evoked potentials N9 at the Erb's point, N13 at the back of the neck, and N20 from the scalp [3]. The naming convention of evoked potential is always a letter P or N followed by a number. P stands for positive peak, and N stands for negative peak. The number can represent the latency of the evoked potential in millisecond or its order in a sequence of evoked potential. Stimulation of the posterior tibial nerve can elicit evoked potentials N8 at the back of the knee, N22 at upper lumbar and lower thoracic spine levels, and P39 from the scalp (Figure 2.2) [3]. The absence of the N20 component from median nerve stimulation has been the iconic predictor of poor neurological outcome in clinical practice [9]–[19].

In rats, constant current pulses of 0.6-7 mA with 200 μs duration at a frequency of 0.5 Hz is often used to stimulate the median or the posterior tibial nerves to record SSEP. Screw electrodes are put on top of the corresponding somatosensory cortex in light contact of the dura mater for recordings [20]–[27]. The N10 component from median nerve stimulation in rat is equivalent to the N20 component in humans.

The SSEP waveform is generally considered to have 4 parts in sequential order: short-latency high frequency oscillations (HFOs), short-latency component (N10 in rat or N20 in human), long-latency HFOs, and lastly long-latency component (N30 in rat or N70 in human). The short-latency HFOs and the N10 component reflect thalamo-cortical activities, and the long-latency HFOs and the N30 component reflect cortico-cortical activities [24], [28]–[35]. Multiple studies showed that the early and later parts of HFOs respond differently to stimulus greater than 10 Hz [33]–[35]. At a stimulus rate of 12.3 Hz, the amplitude of the long-latency HFOs seriously decreased, but that of the short-latency HFOs was barely affected [33]. These results suggested that the long-latency HFOs are generated by postsynaptic neural network in the areas 3b and 1, whereas the short-latency HFOs are generated by action potentials of the thalamocortical fibers [32].

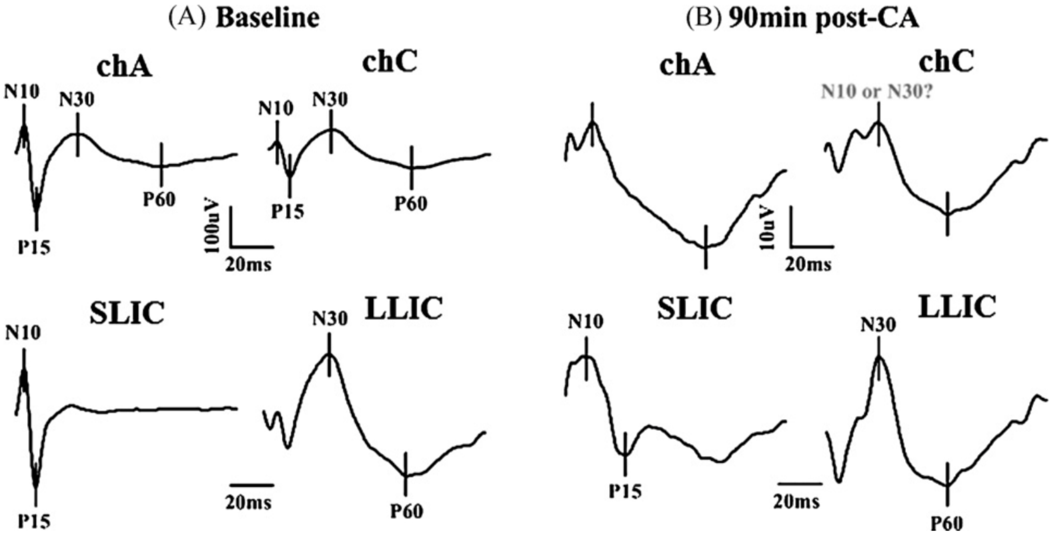

Figure 2.3: Independent component analysis of SSEPs into short- and long- latency components at baseline (A) and after cardiac arrest (B). Each of the two upper plots contain the averaged raw SSEPs of two channels in the same hemisphere. Each of the two lower plots contain the ICA-decomposed independent components. Notice in (B), ICA revealed the covered-up P15 component. (Adapted from [28])

2.3 Advanced SSEP Analysis Methods

2.3.1 Independent Component Analysis

When a multivariate data set is given, it can be assumed to be a linear combination of some latent independent components, which are non-gaussian and mutually independent. Independent component analysis (ICA) is the statistical process of decomposing a signal into its maximum likelihood independent components. ICA is related to principal component analysis (PCA), but is more powerful at identifying the underlying sources. ICA has been commonly used for blind source separation in various neural signals including evoked potential [28], [36]–[39]. In a previous study in our lab, ICA was used to separate the short-latency and long-latency components of SSEPs and helped to

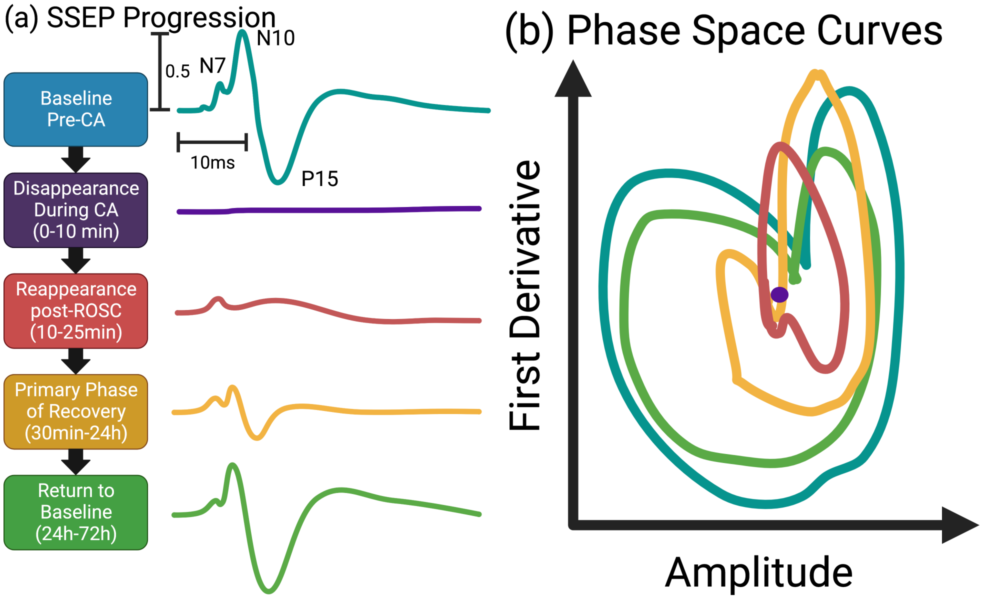

Figure 2.4: Illustrations of SSEP signals and corresponding phase space areas (PSAs). (A) Illustration of progression of SSEP from baseline to recovery after CA (B) Illustration of corresponding PSAs. Notice that signals with smaller amplitudes and narrower widths have smaller areas.

reveal a component hidden after cardiac arrest (Fig. 2.3)[28]. The separation of short- and long-latency components showed different trajectories of recovery after cardiac arrest, suggesting that the two components reflect the injury and recovery of the thalamic and cortical regions, respectively.

2.3.2 Phase Space Analysis

The phase space of a dynamical system is the set of all possible states of a system, with each point in the space representing a unique state [40], [41]. The space usually consists of all possible values of a signal and its derivative, and the system travels from point to point to form the phase space curve (Figure 2.4). Madhok et al. came up with the idea to measure the area encircled by this curve. While the shape of the phase space curve is directly related to the shape of the signal, the area bounded by the curve is related to the energy of the signal [22]. Therefore, a large amplitude and fast transition signal will generate a large phase space area, thus accounting for information in the signal that was previously discarded by the traditional peak amplitude and latency method. It is also advantageous compared to the area under the curve method because a signal with large peak amplitude but narrow width will not generate a large area under the curve but it will for phase space area.

In the original study by Madhok et al., the phase space areas during the first 85-190 minutes post-CA were significantly different ($p = 0.02$) between rats with good outcomes (72 hr neurologic deficit score (NDS) ≥ 50) and poor outcomes (72 hr NDS < 50). Phase space area not only had a high outcome prediction accuracy (80 to 93%, $p < 0.05$) during 85 to 190 minutes post-CA, but also offered 78% sensitivity and 83-100% specificity for good outcomes. In comparison, traditional SSEP N10 to P15 peak-to-peak amplitudes were only good predictors of poor neurological outcomes, with inability to prognosticate good outcomes. Overall, phase space area showed greater greater separation between good and bad neurological recovery groups compared to peak-to-peak amplitudes (Figure 2.5). Phase space area was also used to analyze the effects of hypothermia on SSEPs [22], [27].

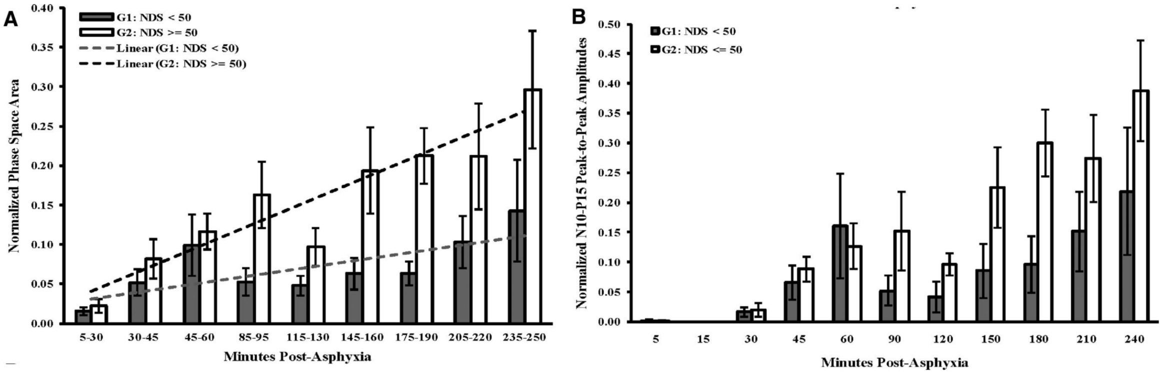

Figure 2.5: Evolution of somatosensory evoked potentials (SSEPs) as assessed by the phase space areas (PSAs) and N10-P15 peak-to-peak amplitudes. (A) Progression of PSA recovery of both the good and bad recovery groups. Although not statistically significant in the immediate phase, the difference of PSAs between the two groups were statistically significant from 85 to 250 minutes post-asphyxia ($p = 0.04$). (B) Progression of N10-P15 peak-to-peak amplitudes. The difference between the two groups was never statistically significant. (Adapted from [22])

2.3.3 Wavelet Analysis

Wavelet literally means "small wave", or in more specific terms, a wave-like transient oscillation in a certain frequency band that begins at zero, oscillates, then return to zero.

Although wavelets can be described by a single function such as in the cases of Morlet wavelet, Mexican hat wavelet, etc. [42], wavelets can also be constructed efficiently through filter banks and multiresolution analysis [43], [44].

Suppose we have a lowpass filter H_0 and a highpass filter H_1. We feed a discrete signal $x[n]$ through the filters and downsample. Then we reconstruct the signal with upsampling and the corresponding reconstruction filters F_0 and F_1 to obtain $\hat{x}[n]$ (Figure 2.6. Ideally, we would like to achieve perfect

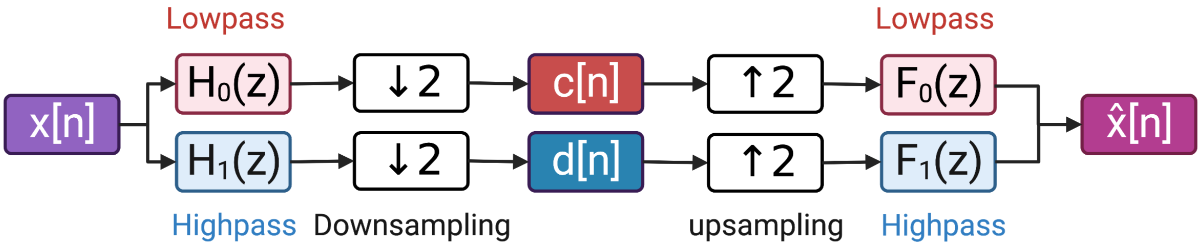

Figure 2.6: Filter Bank Decomposition and Perfect Reconstruction. The signal $x[n]$ is first decomposed by two filters into a lowpassed band and a highpassed band. The two bands of information are then downsampled so the total size of the signal stays the same. The resulting signals of the decomposition stage is $c[n]$ and $d[n]$, both are half the size of the original signal. The two bands of signal are then upsampled again and reconstructed with the corresponding filters to obtain $\hat{x}[n]$. Certain conditions on filter design can be satisfied to achieve perfect reconstruction of the signal

reconstruction of the signal, where $x[n] = \hat{x}[n]$. This is achieved by careful selection of filter coefficients by satisfying the distortion elimination and anti-aliasing conditions [45]. This process is demonstrated below.

In the z-domain:

$$C(z) = \frac{1}{2}\left[H_0(z^{\frac{1}{2}})X(z^{\frac{1}{2}}) + H_0(-z^{\frac{1}{2}})X(-z^{\frac{1}{2}})\right]$$

$$D(z) = \frac{1}{2}\left[H_1(z^{\frac{1}{2}})X(z^{\frac{1}{2}}) + H_1(-z^{\frac{1}{2}})X(-z^{\frac{1}{2}})\right]$$

$$\begin{aligned}
\hat{X}(z) &= F_0(z)C(z^2) + F_1(z)D(z^2) \\
&= \frac{1}{2}\left[H_0(z)X(z) + H_0(-z)X(-z)\right]F_0(z) \\
&+ \frac{1}{2}\left[H_1(z)X(z) + H_1(-z)X(-z)\right]F_1(z) \\
&= \frac{1}{2}\left[H_0(z)F_0(z) + H_1(z)F_1(z)\right]X(z) \\
&+ \frac{1}{2}\left[H_0(-z)F_0(z) + H_1(-z)F_1(z)\right]X(-z)
\end{aligned} \tag{2.1}$$

In order for $\hat{X}(z) = X(z)$, we need to satisfy two conditions:

$$H_0(z)F_0(z) + H_1(z)F_1(z) = 2z^{-D} \tag{2.2}$$

$$H_0(-z)F_0(z) + H_1(-z)F_1(z) = 0 \tag{2.3}$$

To satisfy the second condition, or the anti-aliasing condition, we let

$$\begin{aligned} H_0(-z) &= F_1(z) \\ -H_1(-z) &= F_0(z) \end{aligned} \tag{2.4}$$

Then the first condition becomes:

$$H_0(z)H_1(-z) - H_0(-z)H_1(z) = 2z^{-D} \tag{2.5}$$

Let

$$P_0(z) = H_0(z)F_0(z) = H_0(z)H_1(-z) \tag{2.6}$$

Then

$$P_0(z) - P_0(-z) = 2z^{-D} \tag{2.7}$$

Suppose $P_0(z)$ is in the format of

$$P_0(z) = a + bz^{-1} + cz^{-2} + dz^{-3} + ez^{-4} \tag{2.8}$$

Then

$$P_0(z) - P_0(-z) = 2bz^{-1} + 2dz^{-3} = 2z^{-D} \tag{2.9}$$

From the last equation, we know that D is always odd, and only one odd parameter of $P_0(z)$ can be nonzero. Thus, to design a perfect reconstruction filter bank, we first design a halfband filter $P_0(z)$. Then we spectral factor the roots of $P_0(z)$ into $H_0(z)$ and $F_0(z)$. Lastly, we use the anti-aliasing property to calculate $H_1(z)$ and $F_1(z)$.

Thus, $\hat{x}[n]$ is a perfect reconstruction of $x[n]$ with a delay of D steps.

The simplest and earliest wavelet was developed by Alfred Haar [46]. The lowpass filter is $[\frac{1}{\sqrt{2}} \frac{1}{\sqrt{2}}]$, and the highpass filter is $[\frac{1}{\sqrt{2}} - \frac{1}{\sqrt{2}}]$. Note that the filter coefficients satisfy the conditions listed above. The Haar filters are essentially the moving average and the moving difference filters with energy conservation. In order to produce the Haar wavelets from the Haar filters, Mallat et al. devised the multiresolution analysis as shown in Figure 3.2 [43]. The idea is that by repeating the filters in multilayer design, the kernel will contain more coefficients and the frequency band will become narrower (Figure 2.7). In the case of the Haar wavelet, the scaling function eventually becomes a unit step from 0 to 1, and the wavelet function is 1 from 0 to 0.5, and -1 from 0.5 to 1.

Apart from the Haar wavelets, Daubechies identified the maxflat halfbands and distributed the roots to form the classic Daubechies wavelets. These wavelets have been used extensively in many fields such as image processing and bioelectric signal extraction [44], [47], [48].

Thakor et al. pioneered the use of multiresolution analysis on somatosensory evoked potentials [49]. They showed in an anesthesized cat model that the detailed or higher frequency component of multiresolution analysis displayed an early and rapid decline in response to hypoxic injury, while the

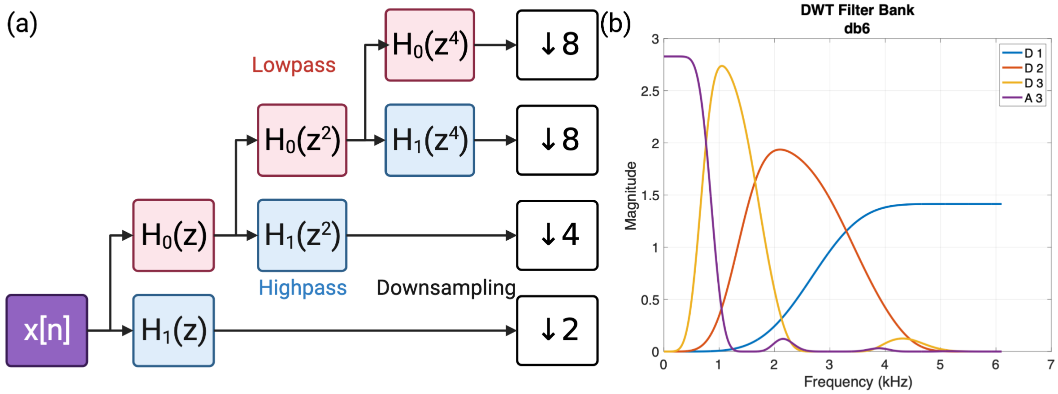

Figure 2.7: Representative filter bank pass bands of a three-layer Daubechies wavelet with 6 vanishing moments (db6). D stands for detail. A stands for approximation. The detail bands correspond to the outputs with the final filter being the highpass filter. The one and only approximation band cooresponds to the output with all lowpass filters, thus it has the lowest frequency band.

coarse component displayed an earlier recovery upon reoxygenation. Another previous study from the lab also used the technique to denoise the SSEP signal [21]. More recently, Superlet analysis has been introduced as the superior method for transient brain signal analysis as it offers superior time and frequency resolution compared to traditional wavelet methods [50]. The authors combined a set of wavelets with increasingly constrained bandwith geometrically. This maintains the good temporal resolution of single wavelets and gains frequency resolution in the upper bands. The idea was adopted from a similar concept, in which superior resolution was achieved with the Fourier transform [51].

Wavelet analysis excels at locating transient oscillation signals in the time-frequency domain. The key with using traditional orthogonal wavelets is to identify the wavelet that best matches the shape of the signal. The orthogonal property will ensure the correlation between the signal and the output will be

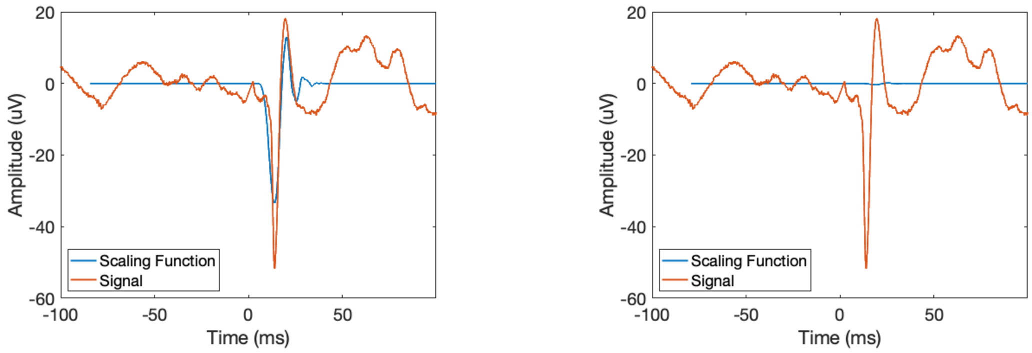

(a) **(b)**

Figure 2.8: Illustrations of the correlation between the scaling function and the signal at two locations. (a) The scaling function matches well with the signal at this location, thus a large correlation coefficient was produced. (b) The scaling function does not match well with the signal at this location, thus a small correlation coefficient was produced.

high only when the signal coincides with the wavelet (Figure 2.8).

Mathematically, the output of wavelet decomposition and reconstruction with the scaling $\phi(t)$ and wavelet $\psi(t)$ functions can be expressed as

$$\begin{aligned} c(k) &= \langle x(t), \phi(t-k) \rangle = \sum_{\tau} x(\tau)\phi(\tau - k) \\ d(s,k) &= \left\langle x(t), \psi(\frac{t-k}{s}) \right\rangle = \sum_{\tau} x(\tau)\psi(\frac{\tau-k}{s}) \\ x(t) &= \sum_{k} c(k)\phi(t-k) + \sum_{s,k} d(s,k)\psi(\frac{t-k}{s}) \end{aligned} \tag{2.10}$$

where $\langle\rangle$ is the dot product operation, k is the parameter for time-shift, and s is the parameter for scale.

2.4 Thalamocortical Coupling Measures

2.4.1 Autoregressive Model

Although not a metric for coupling between multiple channels of data, the autoregressive (AR) model is discussed here as the foundation of the two coupling measures introduced later in this section. The AR model is used to predict future values of a signal based on its values in the past. Shown below is an autoregressive model of order p, where ψ_i are parameters of the model, c is the constant term, and ε is the noise term.

$$X_t = c + \sum_{i=1}^{p} \psi_i X_{t-i} + \varepsilon \tag{2.11}$$

It is also possible to add input or other signals to the model to generate the multivariate autoregressive models with exogenous inputs (MVARX):

$$X_t = c + \sum_{i=1}^{p} \psi_i X_{t-i} + \sum_{j=1}^{p} \phi_i U_{t-j} + \varepsilon \tag{2.12}$$

There have been many successful examples using the autoregressive model and its transfer functions to analyze neural activity [52]–[55]. In the case of signal analysis after cardiac arrest, our lab has utilized the model along with Itakura and cepstral distance to characterize the EEG signal change from baseline to injury and early recovery period [56], [57]. [56] showed that Itakura distance coupled with AR model can distinguish between hypoxia and asphyxia and can predict recovery following the insult.

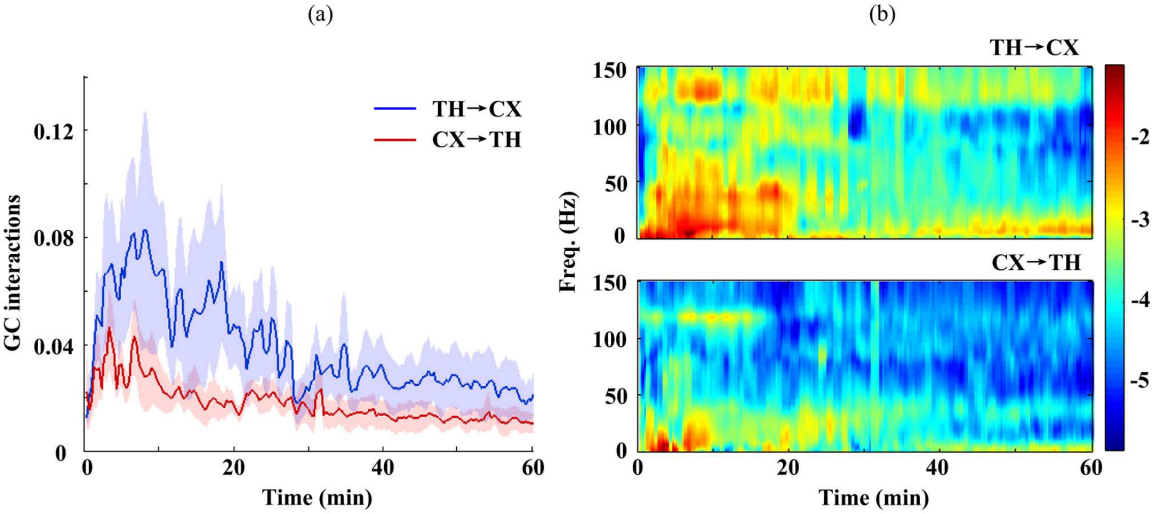

Figure 2.9: Evolution of Granger causalities (GC) between thalamic and cortical local field potentials (LFPs) after CA. (A) Evolution of GC in the time domain. Blue curve represents the GC from the thalamus to the cortex, and the red curve represents the GC from the cortex to the thalamus. Time t = 0 indicates the onset of asphyxia. The GC from the thalamus to the cortex was elevated in the immediate recovery phase after cardiac arrest. (B) Evolution of GC in the frequency domain. Similarly, the GC from the thalamus to the cortex in the 0-50 Hz frequency band was elevated in the immediate recovery phase (Adapted from [58]).

2.4.2 Granger Causality

Granger causality (GC) analysis builds on the framework of the AR model. Clive Granger invented GC based on a bivariate autoregressive model in order to predict a pair of stochastic process in economics [59]. Fundamentally to this analysis, if including signal B in the prediction of signal A reduces the error variance, then we can say signal B "Granger-causes" signal A. Twenty years after the original invention, GC in the spectral domain was invented [60]. Starting from the early 2000s, GC has been used in the field of neuroscience to analyze causal interaction among multi-channel neural data [58], [61]–[64].

To implement the model, let the two channels of data be $x(t)$ and $y(t)$. The two time series can be described by two separate autoregressive (AR) models of order p with certain amount of error ϵ_x or ϵ_y, given by

$$\begin{cases} x(t) = \sum_{i=1}^{p} a_x(i)x(t-i) + \epsilon_x(t),\ \epsilon_x(t) \sim N(0, \sigma_x) \\ y(t) = \sum_{i=1}^{p} a_y(i)y(t-i) + \epsilon_y(t),\ \epsilon_y(t) \sim N(0, \sigma_y) \end{cases}, \tag{2.13}$$

or by two joint AR models with other amount of error ϵ'_x or ϵ'_y, given by

$$\begin{cases} x'(t) = \sum_{i=1}^{p} a_{xx}(i)x(t-i) + \sum_{i=1}^{p} a_{yx}(i)y(t-i) + \epsilon'_x(t), \\ \epsilon'_x(t) \sim N(0, \sigma'_x) \\ y'(t) = \sum_{i=1}^{p} a_{xy}(i)x(t-i) + \sum_{i=1}^{p} a_{yy}(i)y(t-i) + \epsilon'_y(t), \\ \epsilon'_y(t) \sim N(0, \sigma'_y) \end{cases}. \tag{2.14}$$

The level of this causal influence from x to y and from y to x can then be mathematically defined as:

$$g_{xy} = \ln \frac{\sigma_y}{\sigma'_y},\ g_{yx} = \ln \frac{\sigma_x}{\sigma'_x}. \tag{2.15}$$

One of our previous studies used GC interaction to analyze the causal relationship between local field potentials recorded from the thalamic ventral posterolateral nucleus and the primary somatosensory cortex [58]. The study found that during the post-CA acute period the GC interaction from the thalamus to the cortex were consistently higher than those from the cortex to the thalamus (1.983 ± 0.278 times higher, p = 0.021) (Figure 2.9). While GC can be a powerful tool for causality analysis, it should be noted that GC is an estimate and cannot imply true causality. If two processes are driven by a common third process with different latencies, one might still accept the alternative hypothesis of GC. However, manipulation of one of the variables would not change the other [65].

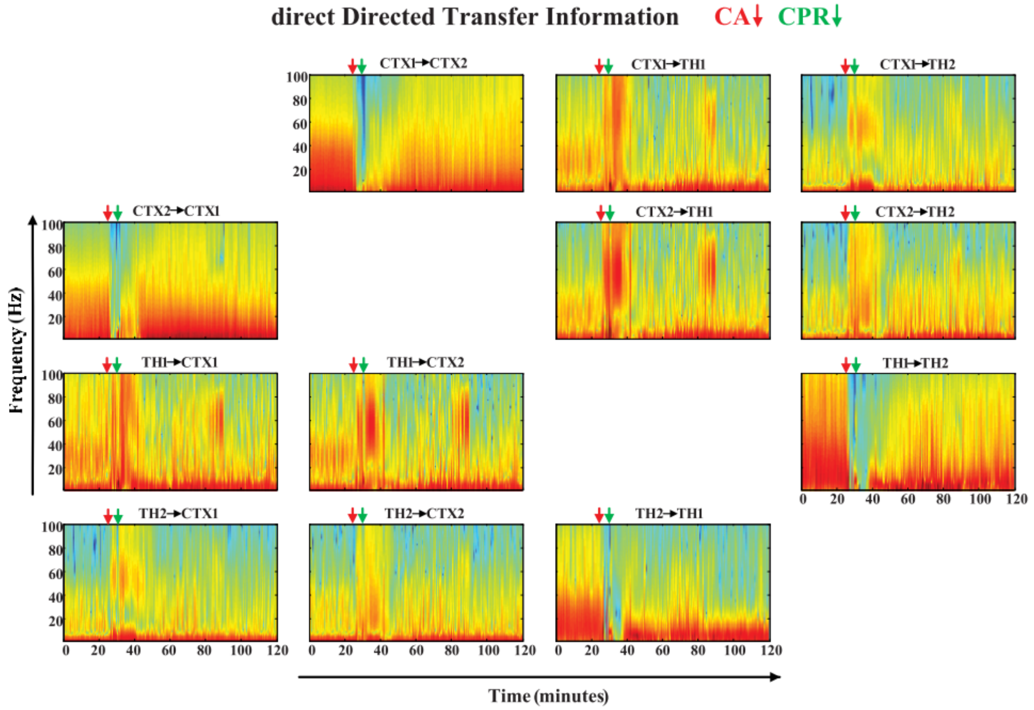

Figure 2.10: Direct Directed Transfer Functions (dDTFs) form a graphical matrix between cortical LFPs (CTX1 and CTX2) and thalamic LFPs (TH1 and TH2) during a 20-min baseline, 5-min anesthesia washout, 5-min asphyxial CA and the following recovery periods. In each small box, the intensity of flow measured by dDTF is reflected in the color scale (minimum=blue, maximum=red). The increase in dDTFs between thalamic and cortical channels can be discerned from the red bars immediately after CA (Adapted from [66]).

2.4.3 Directed Transfer Function & direct Directed Transfer Function

As pointed out by Granger in his later career, the causality principle of GC analysis only hold if there are only two channels of data [67]. Similar to GC analysis, directed transfer function (DTF) was also developed based on the multivariate autoregressive model (MVAR), but has the advantage of accounting for influences from other channels of data. DTF describes the causal influence of channel j on channel i at frequency f. direct Directed

Transfer Function (dDTF) provides the directed partial coherence between a given pair of channels while the influence of all other interconnected channels is statistically excluded [66].

In an MVAR model, an n-channel data vector $X(t) = [x_1(t), x_2(t), x_3(t) \dots x_n(t)]$ can be modelled as:

$$X(t) = \sum_{i=1}^{p} A(i) X(t-i) + E(t) \tag{2.16}$$

where $A(i)$ are the model coefficient vectors, and $E(t)$ is the white noise error term.

Equation 2.16 can be transformed into the frequency domain [68]:

$$\begin{gathered} H(f) = \left(\sum_{m=0}^{p} A(m) \exp(-2\pi i m f \Delta t) \right)^{-1} \\ X(f) = A^{-1}(f) E(f) = H(f) E(f) \\ E(f) = A(f) X(f) = H^{-1}(f) X(f) \end{gathered} \tag{2.17}$$

From the form above, white noise $E(f)$ can be viewed as an input to a linear system, $H(f)$ as the transfer function of the linear system, and the signals $X(f)$ as the output of the linear system. Because the input signal is white noise, the transfer function matrix $H(f)$ contains all the information between data channels. [69] introduced DTF in the form:

$$\gamma_{ij}^2(f) = \frac{|H_{ij}(f)|}{\sum_j |H_{ij}(f)|} \tag{2.18}$$

The DTF describes causal influence of channel j on channel i at frequency f. The equation above represents the ratio between the inflow from channel j to channel i and the summation of all inflow to channel j, i.e. the relative information flow from j to i.

However, the properties of DTF causes it to show information flow between not only causal channels, but also cascading channels. For example, if channel 1 causes channel 2, and channel 2 causes channel 3, DTF will show information flow between channel 1 and 3. Thus, direct Directed Transfer Function (dDTF) was introduced in [70]. The DTF was multiplied by the partial coherence to filter out cascading relationships, thus producing the dDTF.

Partial coherence is defined as

$$\chi_{ij}^2(f) = \frac{M_{ij}^2(f)}{M_{jj}(f)M_{ii}(f)} \tag{2.19}$$

where $M_i j(f)$ is the minor of the spectral matrix produced by removing the i-th row and the j-th column from $X(f)$ [71].

By multiplying the DTF by partial coherence, only the direct connections remain in the dDTF:

$$\sigma_{ij}^2(f) = \gamma_{ij}^2(f)\chi_{ij}^2(f) \tag{2.20}$$

One of our previous studies [66] used the dDTF to show that the dDTFs between the centromedian nucleus of the thalamus and the parietal cortex in both directions increased, accompanied by a shift of maximum intensity to higher frequencies (40-80 Hz), during the immediate recovery phase. On the other hand, the dDTFs between the two cortical channels and between the two thalamic channels both dramatically decreased immediately after CA and gradually recovered afterwards (Figure 2.10).

2.5 Discussion

Summary of all analysis methods reviewed in this chapter can be found in Table 2.1.

ICA has been used extensively in blind source separation and artifact detection in electroencephalogram signal. Our previous study has shown that ICA can also be used to separate short-latency SSEP components from the long-latency ones [28]. However, since ICA is essentially a statistical method, it does not take into account of the SSEP component generator locations. Nevertheless, the physiology of the sensory pathway means that SSEP components with thalamic origins would appear before components with cortical origins, and thus ICA can be used with care to separate SSEP components for coupling analysis in the next step.

PSA is the first measure that can capture the shape information and changes of the SSEP signal after cardiac arrest. To a certain degree, it can also reflect the energy level of the signal. More importantly, it shows large separation between good and bad recovery groups. However, two disctinct SSEP signals could share the same PSA values. Furthermore, it makes no distinction between SSEP components with subcortical and cortical origins. Thus, while PSA may be a promising biomarker for neuroprognostication, it is not suited for development into a metric for thalamocortical coupling.

Multiresolution wavelet (MRW) analysis separates the original signal into different frequency bands. MRW has low time resolution but high frequency resolution at low frequency, and high time resolution but low frequency resolution at high frequency. This adaptive resolution quality enables MRW to accurately localize transient oscillation components in the time-frequency domain. Buried underneath the broadband SSEP wave exists a series of high-frequency oscillation (HFO) component centered around the N10 peak. The HFO components can be extracted with a bandpass filter from 300 to 1000 Hz. However, a multiresolution wavelet matched to the shape of the HFOs would better extract the signal than bandpass filters. Source localization studies in humans have found that the HFO components are generated by the thalamocortical axons [72], [73]. Thus, it is possible to design wavelets to optimally extract the HFO signal for coupling analysis in the next step.

Both of the coupling measures explored previously–GC and dDTF–required simultaneous LFP recordings with microelectrodes from the thalamus and the cortex. While such method is plausible in humans, it is definitely not ideal in post-CA patients as it may trigger further neuronal injury and immune responses [74]. It would be more translatable to clinical practice if a noninvasive thalamocortical coupling measure is developed and validated.

2.6 Conclusion

Based on the review and discussion of current analysis methods of SSEP and coupling, it is worth exploring if a combined method of wavelet extraction of HFOs and coupling analysis between HFOs and N10 peaks may yield a noninvasive bedside biomarker for thalamocortical dissociation after CA.

Table 2.1: Summary of SSEP and Coupling Analysis Methods

Name	Description	Pros	Cons
Independent Component Analysis (ICA) [28]	ICA is the statistical process of decomposing a signal into its maximum likelihood independent components.	ICA can separate short-latency and long-latency components. ICA can also reveal masked components	Since the method is agnostic to the generating mechanism of evoked potential, the extracted components may not generated from single sources
Phase Space Area (PSA) [22]	The phase space curve is the set of coordinates of all possible values of a signal and its derivative, and PSA is the hull area encircled by the curve.	The PSA is related to the energy of a signal, accounting for information discarded by amplitude and latency measures	In many cases, the phase space curves would form multiple circles due to multiple peaks in the original signal. The PSA would only account for the energy of the largest peak component.
Multi-resolution Wavelet (MRW) [49]	MRW transforms a signal into its time-frequency domain representation.	Wavelet is optimized for the identification of transient oscillating signals. Wavelet has adaptive frequency resolution. Wavelet can be used to denoise signal.	Orthogonal wavelet analysis requires the identification of a closely matched wavelet to the signal, which is often done based on visual inspection.
Superlet [50]	Similar to MRW, but superlet combines a set of wavelets geometrically to achieve higher resolution.	While keeping the high time resolution of single wavelet, the superlet method improves the frequency resolution in the upper frequency band.	Little application of the method has been shown.
Granger Causality (GC) [58]	GC quantifies the causality between two channels based on the prediction errors of the autoregressive models	GC is very powerful to quantify the relationship between two channels and has been used extensively in many fields of research.	GC is only an estimate of causality and cannot imply true causality. GC only works for two channels of data.
direct Directed Transfer Function (dDTF) [66]	The dDTF describes the direct causal influence from one channel to another at certain frequency while accounting for the cascading information flow.	Compared to GC, dDTF can estimate the causality for more than two channels of data.	I am not aware of any weakness of the dDTF method.

References

[1] J. G. Betts, K. A. Young, J. A. Wise, E. Johnson, B. Poe, D. H. Kruse, O. Korol, J. E. Johnson, M. Womble, and P. DeSaix, "Central Processing," in *Anatomy & Physiology*, Houston, Texas: OpenStax, 2013. [Online]. Available: `https://openstax.org/books/anatomy-and-physiology/pages/14-2-central-processing`.

[2] D. Purves, G. J. Augustine, and D. Fitzpatrick, *Neuroscience*. Sinauer Associates, 2018.

[3] H. Pratt, "Sensory erp components," *The Oxford handbook of event-related potential components*, pp. 89–114, 2011.

[4] H Pratt, R. Amlie, and A Starr, "Short latency mechanically evoked somatosensory potentials in humans," *Electroencephalography and clinical neurophysiology*, vol. 47, no. 5, pp. 524–531, 1979.

[5] A Carmon, Y Dotan, and Y Sarne, "Correlation of subjective pain experience with cerebral evoked responses to noxious thermal stimulations," *Experimental brain research*, vol. 33, no. 3, pp. 445–453, 1978.

[6] L Garcia-Larrea, M. Frot, and M Valeriani, "Brain generators of laser-evoked potentials: From dipoles to functional significance," *Neurophysiologie clinique/Clinical neurophysiology*, vol. 33, no. 6, pp. 279–292, 2003.

[7] E. Zandbergen, A Hijdra, R. De Haan, J. van Dijk, B. O. de Visser, F Spaans, D. Tavy, and J. Koelman, "Interobserver variation in the interpretation of sseps in anoxic–ischaemic coma," *Clinical neurophysiology*, vol. 117, no. 7, pp. 1529–1535, 2006.

[8] S. J. Luck, *An introduction to the event-related potential technique*. MIT press, 2014.

[9] A. R. Panchal, J. A. Bartos, J. G. Cabañas, M. W. Donnino, I. R. Drennan, K. G. Hirsch, P. J. Kudenchuk, M. C. Kurz, E. J. Lavonas, P. T. Morley, *et al.*, "Part 3: Adult basic and advanced life support: 2020 american heart association guidelines for cardiopulmonary resuscitation and emergency cardiovascular care," *Circulation*, vol. 142, no. 16_Suppl_2, S366–S468, 2020.

[10] S. P. Choi, K. N. Park, J. H. Wee, J. H. Park, C. S. Youn, H. J. Kim, S. H. Oh, Y. S. Oh, S. H. Kim, and J. S. Oh, “Can somatosensory and visual evoked potentials predict neurological outcome during targeted temperature management in post cardiac arrest patients?” *Resuscitation*, vol. 119, pp. 70–75, 2017.

[11] J. H. Kim, M. J. Kim, J. S. You, H. S. Lee, Y. S. Park, I. Park, and S. P. Chung, “Multimodal approach for neurologic prognostication of out-of-hospital cardiac arrest patients undergoing targeted temperature management,” *Resuscitation*, vol. 134, pp. 33–40, 2019.

[12] R. N. Leão, P. Ávila, R. Cavaco, N. Germano, and L. Bento, “Therapeutic hypothermia after cardiac arrest: Outcome predictors,” *Revista Brasileira de terapia intensiva*, vol. 27, pp. 322–332, 2015.

[13] E. Golan, K. Barrett, A. S. Alali, A. Duggal, D. Jichici, R. Pinto, L. Morrison, and D. C. Scales, “Predicting neurologic outcome after targeted temperature management for cardiac arrest: Systematic review and meta-analysis,” *Critical care medicine*, vol. 42, no. 8, pp. 1919–1930, 2014.

[14] B. J. Ruijter, M. C. Tjepkema-Cloostermans, S. C. Tromp, W. M. van den Bergh, N. A. Foudraine, F. H. Kornips, G. Drost, E. Scholten, F. H. Bosch, A. Beishuizen, *et al.*, “Early electroencephalography for outcome prediction of postanoxic coma: A prospective cohort study,” *Annals of neurology*, vol. 86, no. 2, pp. 203–214, 2019.

[15] A Grippo, R Carrai, M Scarpino, M Spalletti, G Lanzo, C Cossu, A Peris, S Valente, and A. Amantini, “Neurophysiological prediction of neurological good and poor outcome in post-anoxic coma,” *Acta Neurologica Scandinavica*, vol. 135, no. 6, pp. 641–648, 2017.

[16] M. Scarpino, F. Lolli, G. Lanzo, R. Carrai, M. Spalletti, F. Valzania, M. Lombardi, D. Audenino, M. G. Celani, A. Marrelli, *et al.*, “Neurophysiological and neuroradiological test for early poor outcome (cerebral performance categories 3–5) prediction after cardiac arrest: Prospective multicentre prognostication data,” *Data in brief*, vol. 27, p. 104 755, 2019.

[17] M. Scarpino, R. Carrai, F. Lolli, G. Lanzo, M. Spalletti, F. Valzania, M. Lombardi, D. Audenino, S. Contardi, M. G. Celani, *et al.*, “Neurophysiology for predicting good and poor neurological outcome at 12 and 72 h after cardiac arrest: The proneca multicentre prospective study,” *Resuscitation*, vol. 147, pp. 95–103, 2020.

[18] S. W. Kim, J. S. Oh, J. Park, H. H. Jeong, J. H. Kim, J. H. Wee, S. H. Oh, S. P. Choi, K. N. Park, *et al.*, "Short-latency positive peak following n20 somatosensory evoked potential is superior to n20 in predicting neurologic outcome after out-of-hospital cardiac arrest," *Critical care medicine*, vol. 46, no. 6, e545–e551, 2018.

[19] C. B. Maciel, A. O. Morawo, C. Y. Tsao, T. S. Youn, D. R. Labar, E. O. Rubens, and D. M. Greer, "Ssep in therapeutic hypothermia era," *Journal of Clinical Neurophysiology*, vol. 34, no. 5, pp. 469–475, 2017.

[20] R. G. Geocadin, J. Muthuswamy, D. L. Sherman, N. V. Thakor, and D. F. Hanley, "Early electrophysiological and histologic changes after global cerebral ischemia in rats," *Movement disorders*, vol. 15, no. S1 S1, pp. 14–21, 2000.

[21] X. Kang, M. Koenig, I. Orukari, R. G. Geocadin, and N. V. Thakor, "Assessment of post-cardiac-arrest somatosensory evoked potential in rats," in *2009 4th International IEEE/EMBS Conference on Neural Engineering*, IEEE, 2009, pp. 609–613.

[22] J. Madhok, A. Maybhate, W. Xiong, M. A. Koenig, R. G. Geocadin, X. Jia, and N. V. Thakor, "Quantitative assessment of somatosensory-evoked potentials after cardiac arrest in rats: Prognostication of functional outcomes," *Critical care medicine*, vol. 38, no. 8, p. 1709, 2010.

[23] W. Xiong, M. A. Koenig, J. Madhok, X. Jia, H. A. Puttgen, N. V. Thakor, and R. G. Geocadin, "Evolution of somatosensory evoked potentials after cardiac arrest induced hypoxic–ischemic injury," *Resuscitation*, vol. 81, no. 7, pp. 893–897, 2010.

[24] D. Wu, W. Xiong, X. Jia, R. G. Geocadin, and N. V. Thakor, "Short-and long-latency somatosensory neuronal responses reveal selective brain injury and effect of hypothermia in global hypoxic ischemia," *Journal of neurophysiology*, vol. 107, no. 4, pp. 1164–1171, 2012.

[25] F. A. Bazley, A. Maybhate, C. S. Tan, N. V. Thakor, C. Kerr, and A. H. All, "Enhancement of bilateral cortical somatosensory evoked potentials to intact forelimb stimulation following thoracic contusion spinal cord injury in rats," *IEEE Transactions on Neural Systems and Rehabilitation Engineering*, vol. 22, no. 5, pp. 953–964, 2014.

[26] G. Agrawal, C. Kerr, N. V. Thakor, and A. H. All, “Characterization of graded multicenter animal spinal cord injury study contusion spinal cord injury using somatosensory-evoked potentials,” *Spine*, vol. 35, no. 11, pp. 1122–1127, 2010.

[27] L. M. Young, R. Choudhary, and X. Jia, “Multimodel quantitative analysis of somatosensory evoked potentials after cardiac arrest with graded hypothermia,” in *2016 38th Annual International Conference of the IEEE Engineering in Medicine and Biology Society (EMBC)*, IEEE, 2016, pp. 1846–1849.

[28] D. Wu, B. Anastassios, W. Xiong, J. Madhok, X. Jia, and N. V. Thakor, “Study of the origin of short-and long-latency ssep during recovery from brain ischemia in a rat model,” *Neuroscience letters*, vol. 485, no. 3, pp. 157–161, 2010.

[29] C. Madl, G. Grimm, L. Kramer, W Yagenehfar, F. Sterz, A Kranz, B Schneeweiss, K Lenz, and B Schneider, “Early prediction of individual outcome after cardiopulmonary resuscitation,” *The Lancet*, vol. 341, no. 8849, pp. 855–858, 1993.

[30] D. S. Wheeler, H. R. Wong, T. P. Shanley, *et al.*, *The Central Nervous System in Pediatric Critical Illness and Injury*. Springer, 2009, p. 80.

[31] C. Endisch, G. Waterstraat, C. Storm, C. J. Ploner, G. Curio, and C. Leithner, “Cortical somatosensory evoked high-frequency (600 hz) oscillations predict absence of severe hypoxic encephalopathy after resuscitation,” *Clinical Neurophysiology*, vol. 127, no. 7, pp. 2561–2569, 2016.

[32] I. Ozaki and I. Hashimoto, “Exploring the physiology and function of high-frequency oscillations (hfos) from the somatosensory cortex,” *Clinical neurophysiology*, vol. 122, no. 10, pp. 1908–1923, 2011.

[33] E. Urasaki, T. Genmoto, N. Akamatsu, S.-i. Wada, and A. Yokota, “The effects of stimulus rates on high frequency oscillations of median nerve somatosensory-evoked potentials–direct recording study from the human cerebral cortex,” *Clinical neurophysiology*, vol. 113, no. 11, pp. 1794–1797, 2002.

[34] T. Emori, T. Yamada, Y. Seki, A. Yasuhara, K. Ando, Y. Honda, A. A. Leis, and P. Vachatimanont, “Recovery functions of fast frequency potentials in the initial negative wave of median sep,” *Electroencephalography and clinical neurophysiology*, vol. 78, no. 2, pp. 116–123, 1991.

[35] F. Klostermann, G. Nolte, and G. Curio, “Multiple generators of 600 hz wavelets in human sep unmasked by varying stimulus rates,” *Neuroreport*, vol. 10, no. 8, pp. 1625–1629, 1999.

[36] S. Makeig, T.-P. Jung, A. J. Bell, D. Ghahremani, and T. J. Sejnowski, “Blind separation of auditory event-related brain responses into independent components,” *Proceedings of the National Academy of Sciences*, vol. 94, no. 20, pp. 10 979–10 984, 1997.

[37] M. J. McKeown, T.-P. Jung, S. Makeig, G. Brown, S. S. Kindermann, T.-W. Lee, and T. J. Sejnowski, “Spatially independent activity patterns in functional mri data during the stroop color-naming task,” *Proceedings of the National Academy of Sciences*, vol. 95, no. 3, pp. 803–810, 1998.

[38] S. Maeda, S. Inagaki, H. Kawaguchi, and W.-J. Song, “Separation of signal and noise from in vivo optical recording in guinea pigs using independent component analysis,” *Neuroscience letters*, vol. 302, no. 2-3, pp. 137–140, 2001.

[39] D. Lelic, M. Gratkowski, M. Valeriani, L. Arendt-Nielsen, and A. M. Drewes, “Inverse modeling on decomposed electroencephalographic data: A way forward?” *Journal of Clinical Neurophysiology*, vol. 26, no. 4, pp. 227–235, 2009.

[40] T. Tao, “Phase space,” *The Princeton Companion to Mathematics*, 2008.

[41] D. D. Nolte, “The tangled tale of phase space,” *Physics today*, vol. 63, no. 4, pp. 33–38, 2010.

[42] J. Morlet, G Arens, E Fourgeau, and D Glard, “Wave propagation and sampling theory—part i: Complex signal and scattering in multilayered media,” *Geophysics*, vol. 47, no. 2, pp. 203–221, 1982.

[43] S. G. Mallat, “A theory for multiresolution signal decomposition: The wavelet representation,” *IEEE transactions on pattern analysis and machine intelligence*, vol. 11, no. 7, pp. 674–693, 1989.

[44] I. Daubechies, “The wavelet transform, time-frequency localization and signal analysis,” *IEEE transactions on information theory*, vol. 36, no. 5, pp. 961–1005, 1990.

[45] M. Vetterli and C. Herley, “Wavelets and filter banks: Theory and design,” *IEEE transactions on signal processing*, vol. 40, no. ARTICLE, pp. 2207–2232, 1992.

[46] A. Haar, *Zur theorie der orthogonalen funktionensysteme*. Georg-August-Universitat, Gottingen., 1909.

[47] J. Z. Wang, G. Wiederhold, O. Firschein, and S. Xin Wei, "Content-based image indexing and searching using daubechies' wavelets," *International Journal on Digital Libraries*, vol. 1, no. 4, pp. 311–328, 1998.

[48] S. Mahmoodabadi, A. Ahmadian, and M. Abolhasani, "Ecg feature extraction using daubechies wavelets," in *Proceedings of the fifth IASTED International conference on Visualization, Imaging and Image Processing*, 2005, pp. 343–348.

[49] N. V. Thakor, G. Xin-Rong, S. Yi-Chun, and D. F. Hanley, "Multiresolution wavelet analysis of evoked potentials," *IEEE transactions on biomedical engineering*, vol. 40, no. 11, pp. 1085–1094, 1993.

[50] V. V. Moca, H. Bârzan, A. Nagy-Dăbâcan, and R. C. Mureșan, "Time-frequency super-resolution with superlets," *Nature communications*, vol. 12, no. 1, pp. 1–18, 2021.

[51] I. Shafi, J. Ahmad, S. I. Shah, and F. M. Kashif, "Techniques to obtain good resolution and concentrated time-frequency distributions: A review," *EURASIP Journal on Advances in Signal processing*, vol. 2009, no. 1, p. 673 539, 2009.

[52] V. Goel, A. M. Brambrink, A. Baykal, R. C. Koehler, D. F. Hanley, and N. V. Thakor, "Dominant frequency analysis of eeg reveals brain's response during injury and recovery," *IEEE transactions on biomedical engineering*, vol. 43, no. 11, pp. 1083–1092, 1996.

[53] M. Ding, S. L. Bressler, W. Yang, and H. Liang, "Short-window spectral analysis of cortical event-related potentials by adaptive multivariate autoregressive modeling: Data preprocessing, model validation, and variability assessment," *Biological cybernetics*, vol. 83, no. 1, pp. 35–45, 2000.

[54] J.-Y. Chang, A. Pigorini, M. Massimini, G. Tononi, L. Nobili, and B. D. Van Veen, "Multivariate autoregressive models with exogenous inputs for intracerebral responses to direct electrical stimulation of the human brain," *Frontiers in human neuroscience*, vol. 6, p. 317, 2012.

[55] G. Kamali, R. J. Smith, M. Hays, C. Coogan, N. E. Crone, J. Y. Kang, and S. V. Sarma, "Transfer function models for the localization of seizure onset zone from cortico-cortical evoked potentials," *Frontiers in neurology*, vol. 11, 2020.

[56] X. Kong, N. Thakor, and V. Goel, "Characterization of eeg signal changes via itakura distance," in *Proceedings of 17th International Conference of the Engineering in Medicine and Biology Society*, IEEE, vol. 2, 1995, pp. 873–874.

[57] J. Paul, S Tong, D Sherman, A Bezerianos, and N. Thakor, "On the application of model based distance metrics of signals for detection of brain injury," in *Proceedings of the 11th IEEE Signal Processing Workshop on Statistical Signal Processing (Cat. No. 01TH8563)*, IEEE, 2001, pp. 257–260.

[58] C. Chen, A. Maybhate, D. Israel, N. V. Thakor, and X. Jia, "Assessing thalamocortical functional connectivity with granger causality," *IEEE Transactions on Neural Systems and Rehabilitation Engineering*, vol. 21, no. 5, pp. 725–733, 2013.

[59] C. W. Granger, "Investigating causal relations by econometric models and cross-spectral methods," *Econometrica: journal of the Econometric Society*, pp. 424–438, 1969.

[60] J. Geweke, "Measurement of linear dependence and feedback between multiple time series," *Journal of the American statistical association*, vol. 77, no. 378, pp. 304–313, 1982.

[61] M. Kamiński, M. Ding, W. A. Truccolo, and S. L. Bressler, "Evaluating causal relations in neural systems: Granger causality, directed transfer function and statistical assessment of significance," *Biological cybernetics*, vol. 85, no. 2, pp. 145–157, 2001.

[62] M. Ding, Y. Chen, and S. L. Bressler, "17 granger causality: Basic theory and application to neuroscience," *Handbook of time series analysis: recent theoretical developments and applications*, vol. 437, 2006.

[63] C. Chen, A. Maybhate, and N. V. Thakor, "Granger causality analysis reveals the changes of thalamocortical functionality after cardiac arrest induced hypoxic-ischemic injury," in *2012 38th Annual Northeast Bioengineering Conference (NEBEC)*, IEEE, 2012, pp. 63–64.

[64] A. K. Seth, A. B. Barrett, and L. Barnett, "Granger causality analysis in neuroscience and neuroimaging," *Journal of Neuroscience*, vol. 35, no. 8, pp. 3293–3297, 2015.

[65] A. Maybhate, C. Chen, N. V. Thakor, and X. Jia, "Effect of hypothermia on the thalamocortical function in the rat model," in *2012 Annual International Conference of the IEEE Engineering in Medicine and Biology Society*, IEEE, 2012, pp. 4680–4683.

[66] D. Wu, A. Bezerianos, D. Sherman, X. Jia, and N. V. Thakor, “Causal interactions between thalamic and cortical lfps following hypoxic-ischemic brain injury,” in *2011 5th International IEEE/EMBS Conference on Neural Engineering*, IEEE, 2011, pp. 184–187.

[67] C. W. Granger, “Testing for causality: A personal viewpoint,” *Journal of Economic Dynamics and control*, vol. 2, pp. 329–352, 1980.

[68] K. J. Blinowska, “Review of the methods of determination of directed connectivity from multichannel data,” *Medical & biological engineering & computing*, vol. 49, no. 5, pp. 521–529, 2011.

[69] M. J. Kaminski and K. J. Blinowska, “A new method of the description of the information flow in the brain structures,” *Biological cybernetics*, vol. 65, no. 3, pp. 203–210, 1991.

[70] A. Korzeniewska, M. Mańczak, M. Kamiński, K. J. Blinowska, and S. Kasicki, “Determination of information flow direction among brain structures by a modified directed transfer function (ddtf) method,” *Journal of neuroscience methods*, vol. 125, no. 1-2, pp. 195–207, 2003.

[71] L. A. Baccalá and K. Sameshima, “Partial directed coherence: A new concept in neural structure determination,” *Biological cybernetics*, vol. 84, no. 6, pp. 463–474, 2001.

[72] T. Kimura, I. Ozaki, and I. Hashimoto, “Impulse propagation along thalamocortical fibers can be detected magnetically outside the human brain,” *Journal of Neuroscience*, vol. 28, no. 47, pp. 12 535–12 538, 2008.

[73] R Gobbelé, T. Waberski, H Simon, E Peters, F Klostermann, G Curio, and H Buchner, “Different origins of low-and high-frequency components (600 hz) of human somatosensory evoked potentials,” *Clinical neurophysiology*, vol. 115, no. 4, pp. 927–937, 2004.

[74] H. W. Bedell, N. J. Schaub, J. R. Capadona, and E. S. Ereifej, “Differential expression of genes involved in the acute innate immune response to intracortical microelectrodes,” *Acta biomaterialia*, vol. 102, pp. 205–219, 2020.

Chapter 3

High Frequency Oscillation Granger Causality Analysis of Somatosensory Evoked Potentials

3.1 Abstract

Previous chapters showed that there is a need to develop bedside monitoring of thalamocortical dissociation after CA. After cardiac arrest, brain injury is first induced by ischemia and subsequent reperfusion of the brain [1]. While the cortex is more vulnerable to ischemic injury compared to subcortical structures, we believe that the thalamus is the key structure to wake up unconscious comatose patients after cardiac arrest. Thus, it is important to characterize the progression of thalamic injury after return of spontaneous circulation.

In this chapter, we hypothesized that the thalamocortical dissociation after cardiac arrest can be characterized by the Granger causality (GC) between the broadband SSEP signal and the high-frequency oscillation (HFO) SSEP signal. With the help of the db6 orthogonal wavelet, the SSEP signal was successfully

separated into the two frequency bands. Their different signal origins were validated by the different trajectories of amplitude recovery after cardiac arrest. In the 3-minute cardiac arrest cases, both the broadband and HFO amplitudes recovered in the first 10 minutes post-CA, while the HFO amplitude recovery predated the braodband amplitude recovery in the 7-minute cardiac arrest cases. Granger causality autoregressive models were trained on the baseline data for each subject, and successfully captured the dissociation between the broadband and HFO signals after cardiac arrest in the 7-minute cases. In the 3-minute cases, Granger causality showcased a smaller dip in the first 10 minutes of recovery, indicating a lower level of injury. These results shed light on the importance of the first 10 minutes of recovery and will help in identifying effective perturbation or treatment to the thalamocortical injury. Future work can leverage the method developed here to evaluate the effects of potential interventions on TC dissociation after CA.

3.2 Introduction

With improved cardiac arrest (CA) care, CA has become the leading cause of coma [2]. The comatose state, if persistent, is the strongest predictor of poor neurological outcome and usually leads to the withdraw of life support [3], [4]. Thus, there is an increasing need for better assessment parameters of the progression of cortical and subcortical injuries after global cerebral ischemia. Global cerebral ischemia after CA triggers a cascade of cellular and molecular processes that results in ischemic neuronal injury [5]. MRI studies have discovered a selective vulnerability of the thalamus to hypoxic-ischemic injury in humans [6] and have shown the importance of early thalamocortical (TC) reperfusion to neurological recovery in a rodent model [7]. In particular, the thalamus plays important roles in sensory processing and relaying [8], attention and sleep regulation [9], [10], and most importantly arousal from unconsciousness [11], [12]. Thus, we believe that it is important to characterize thalamic injury after CA.

In our previous studies in a rodent model of cardiac arrest, our group recorded local field potentials (LFPs) from the ventroposterior lateral nucleus of the thalamus and the forelimb area of the primary somatosensory cortex (S1) in a rodent CA model. The TC synchronization was then quantified with Granger causality interactions (GCIs) and other techniques [13]–[15]. It was found that the information flow from the thalamus to the cortex and vice versa both increased in the first 10 minutes of recovery compared to baseline. Although the general cortical and thalamic activities were reduced after resuscitation from CA, the increased connectivity was hypothesized to be related to injury of the inhibitory thalamic reticular nucleus (RT) [16]–[19]. Nevertheless, our current understanding of the increased connectivity is limited, and therefore, further studies are needed to elucidate its potential clinical implications and impacts.

However, LFP is an invasive measure and fraught with complications clinically [20]. To the contrary, somatosensory evoked potentials (SSEPs) are noninvasive measures of cortical evoked potentials from stimulations of the median or posterior tibial nerves. Furthermore, SSEPs are commonly used for prognostication of neurological outcomes after cardiac arrest [21].

The N20 component in humans (N10 in rats) is a negative peak component that situates approximately 20 ms after stimulation onset and represents cortical neuron activation [21], [22]. Previous studies found that the absence of N20 in humans is the most reliable predictor of poor neurological outcome [21], [23], but the presence of N20 is unreliable as a predictor of favorable outcome. In this rodent model, we observed that around the N10 component are high-frequency oscillations (HFOs) in the range of 300-1000Hz, which can be separated by the peak of the N10 component into an early component generated by TC action potentials, and a late component generated by spiking activities in the primary somatosensory cortex [24], [25]. In another previous study from our group, we found that the HFOs and N10 followed different trajectories of recovery after CA, signaling a TC decoupling [26].

Therefore, this chapter proposes a noninvasive Granger causality measurement between the SSEP N10 and HFO components to quantify the TC connectivity after CA. The new noninvasive measurement could capture the TC dynamics after CA and may have high clinical impact as it is less invasive and easier to measure.

3.3 Methods

3.3.1 Animal Model

All experiment protocols were approved by the Johns Hopkins Animal Care and Use Committee. 4 male Wistar rats were subjected to 7-minute asphyxial CA as the severe injury group, and 2 male Wistar rats were subjected to 3-minute asphyxial CA as the mild injury group.

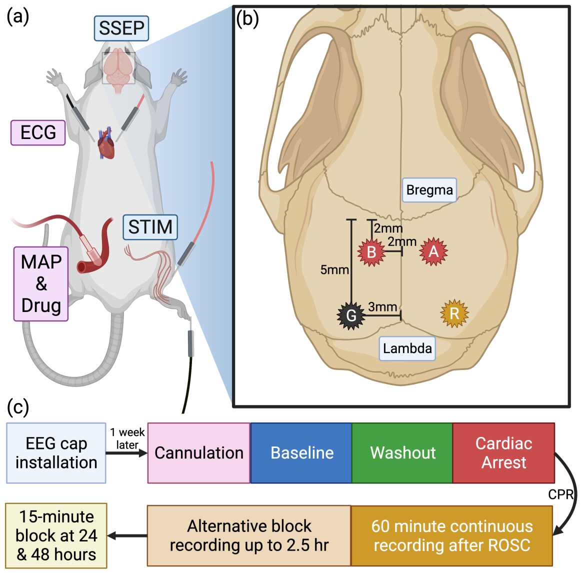

Figure 3.1: (a) Placements of electrodes for arterial catheter, SSEP stimulating, and ECG recording electrodes. (b) EEG electrodes placements. Electrodes A and B were placed on the S1 hindlimb regions. Ground and reference electrodes were placed on top of the parietal lobe. (c) Experimental timeline. Created with Biorender.com

Experimental procedures were described in detail in [7], [19]. Briefly, the rats were intubated and ventilated with 2% isoflurane in 1:1 N_2/O_2. The left femoral artery and vein were cannulated to record blood pressure and administrate medications. After a 10-minute baseline SSEP recording and a 5-minute anesthesia washout, CA was induced for 3 or 7 minutes. Immediately following the asphyxia period, cardiopulmonary resuscitation (CPR) was performed until the return of spontaneous circulation (ROSC) (Fig. 3.1 (c)). SSEPs were recorded continuously from baseline to 60 minutes post-ROSC.

3.3.2 Stimulation and Recording

A stainless-steel electrode (F-E2-48, Natus, Gort, Ireland) was inserted into the gap between the second and third digits of the right paw, and another electrode was inserted at the middle of the gastrocnemius muscle (Fig. 3.1 (a)). The correct electrode placement was confirmed by the existence of SSEPs. Stimulation pulses were 200 µs in duration and 6 mA in amplitude, and the stimulation was delivered every two seconds through an isolated constant current stimulator (DS3, Digitimer Ltd., Hertforshire, England).

Two transcranial screw electrodes (E363/20, P1 Technologies, Roanoke, VA) were implanted on the S1 hindlimb regions for SSEP recording (AP: -2; ML: ±2), and two more on the parietal lobe (AP: -5; ML: ±3) as the intracranial reference and ground (Fig. 3.1 (b)). SSEPs were sampled at 12.2 kHz continuously on the TDT system (TDT System 3, Tucker-David Technologies, Alachua, FL). Each trial was recorded from 100 ms before to 200 ms after stimulation onset. The ipsilateral evoked potentials were subtracted from the contralateral evoked potentials, and the means of the pre-stimulus baseline period were removed to form the single-trial SSEPs. Because of the phase-locked quality of SSEPs, the single-trial recordings were averaged 100 times to increase the signal-to-noise ratios.

The N10 amplitude was measured as the peak-to-peak amplitude between the N10 and P13 components identified in a time window of 8 to 23 ms after stimulation onset (Fig. 3.2 (b)). The HFO amplitude was measured as the maximum amplitude in the HFOs in the same time window. Both amplitudes were normalized to the baseline amplitudes for each subject.

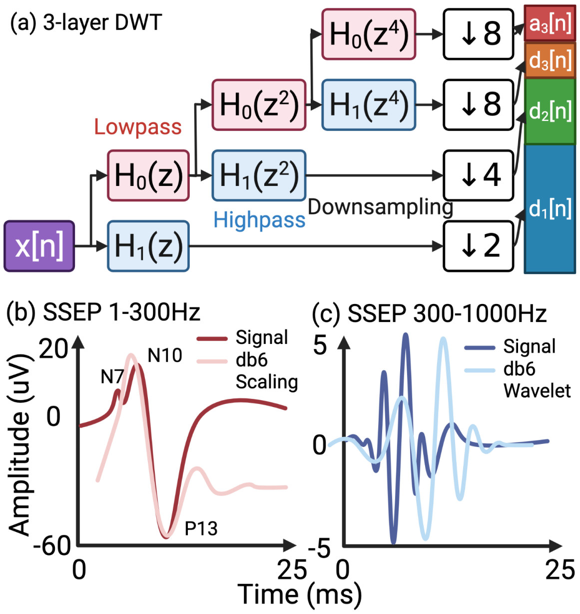

Figure 3.2: (a) Illustration of a 3-layer DWT that produces one approximation layer and three detail layers. The relative heights of the coefficient blocks correspond to their frequency band ranges. (b) The db6 scaling function matches with the N10 component. (c) The db6 wavelet function matches with the HFO components. Created with Biorender.com

3.3.3 Wavelet Decomposition and Reconstruction

Since SSEP components (N10 and HFO) are transient signals that have stimulus-locked properties and exist in two distinct frequency bands (0-300 Hz and 300-1000 Hz), the two signals can be extracted and denoised with the discrete wavelet transform (DWT) [27]. We selected the Debauchies 6 (db6) orthogonal scaling function and mother wavelet because we found it to reconstruct the signal using a single coefficient with the least mean square error and best R-square scores (Fig. 3.2 (b) (c)). We performed a 6-layer DWT to produce one approximation layer and six detail layers (Fig. 3.2 (a)). The seven layers of coefficients correspond to passbands of 0-95 Hz, 95-190

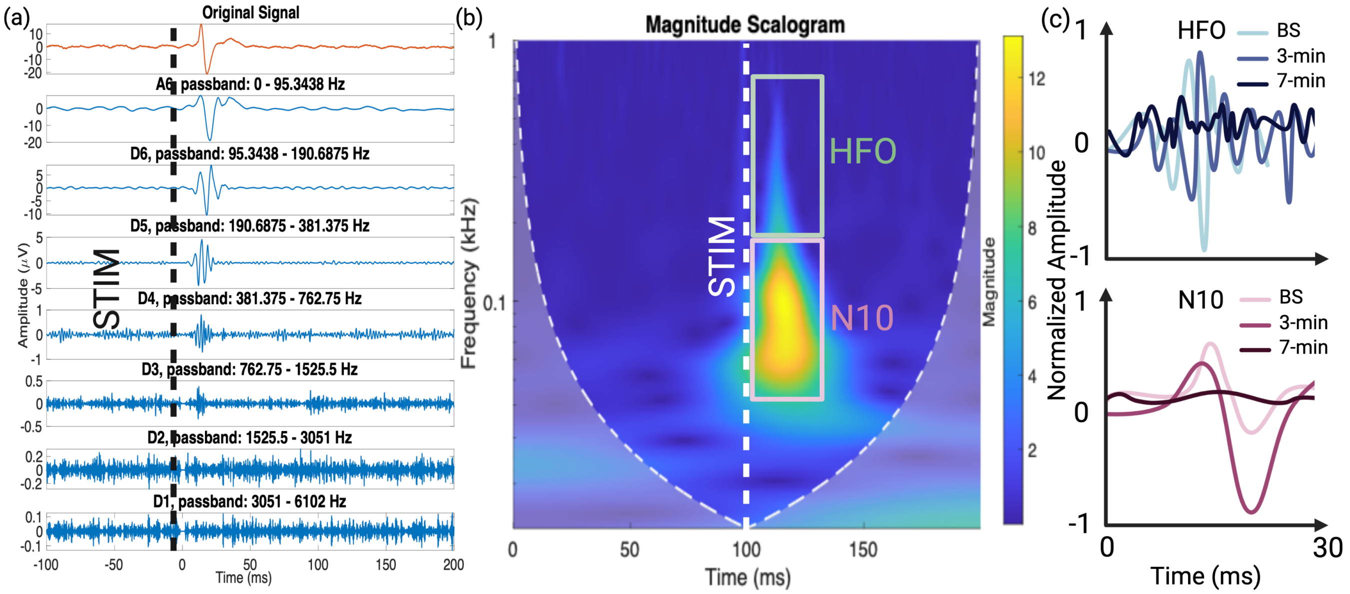

Figure 3.3: SSEP N10 and HFOs. (a) Representative wavelet decomposition and reconstruction of 100-trial averaged SSEP into 1 approximation and 6 detail bands. The stimulation was a single pulse at 0 ms. The localized SSEPs can be discerned from bands A6 to D3. (b) Representation of the same signal in the wavelet time-frequency domain using continuous wavelet transform. The stimulation was a single pulse at 100 ms. The N10 and HFO components were well-localized in both time and frequency. (c) Illustration of SSEP waveform changes at 10 minutes of recovery from one 3-min and one 7-min subject. Created with Biorender.com

Hz, 190-381 Hz, 381-762 Hz, 762-1525 Hz, 1525-3051 Hz, and 3051-6102 Hz, respectively. Since it's known that the N10 lies in the 0-300 Hz range and the HFOs lie in the 300-1000 Hz range, the N10 component was reconstructed with the approximation (a6) and the first layer of detail coefficients (d6), and the HFO component was reconstructed with the second and third layers of detail coefficients (d4-d5) (Fig. 3.3 (a)) [24]. Although the D3 band also contained a localized HFO components, it was not included in the HFO reconstruction due to its low signal-to-noise ratio.

3.3.4 Granger Causality Interaction

Although Granger causality interaction (GCI) was initially developed for economics analysis, its use in neuroscience has become popular in the last decade [28], [29]. If, by incorporating the past values of $y(t)$ in the prediction of $x(t)$, the prediction error is lower than the error of predicting with just the past values of $x(t)$, then we can accept the alternative hypothesis that $y(t)$ "Granger-causes" $x(t)$.

Let the extracted time series HFOs be $x(t)$, and N10 be $y(t)$. The two time series can be described by two separate autoregressive (AR) models of order p with certain amount of error ϵ_x or ϵ_y:

$$\begin{cases} x(t) = \sum_{i=1}^{p} a_x(i)x(t-i) + \epsilon_x(t),\ \epsilon_x(t) \sim N(0, \sigma_x) \\ y(t) = \sum_{i=1}^{p} a_y(i)y(t-i) + \epsilon_y(t),\ \epsilon_y(t) \sim N(0, \sigma_y) \end{cases} \tag{3.1}$$

Or by two joint AR models with other amount of error ϵ'_x or ϵ'_y:

$$\begin{cases} x'(t) = \sum_{i=1}^{p} a_{xx}(i)x(t-i) + \sum_{i=1}^{p} a_{yx}(i)y(t-i) + \epsilon'_x(t), \\ \epsilon'_x(t) \sim N(0, \sigma'_x) \\ y'(t) = \sum_{i=1}^{p} a_{xy}(i)x(t-i) + \sum_{i=1}^{p} a_{yy}(i)y(t-i) + \epsilon'_y(t), \\ \epsilon'_y(t) \sim N(0, \sigma'_y) \end{cases} \tag{3.2}$$

The level of this causal influence from x to y and from y to x can then be mathematically defined as:

$$g_{xy} = \ln \frac{\sigma_y}{\sigma'_y},\ g_{yx} = \ln \frac{\sigma_x}{\sigma'_x} \tag{3.3}$$

In this study, the joint and separate AR models were trained on baseline data for each subject using the multivariate Granger causality MATLAB toolbox [30]. The order of the autoregressive model was determined using the

Akaike information criterion (AIC) [31]. The AIC dropped monotonically with increasing model order until an order of 180, which corresponds to a time-period of 14.75 ms with the sampling frequency of 12.2 kHz. Such period is sensible out of the signal length of 200 ms, so a model of order 180 was selected for all GC analysis. Lastly, the GCI were calculated based on the errors made by these models with a moving window of 100 trials and 20 trials as the moving step.

3.3.5 Statistical Analysis

Two-sample t tests were performed at each time point to test the alternative hypothesis that the amplitudes or GCI measures from the 3-min and 7-min groups were from different populations.

3.4 Results

Fig. 3.3 (a) shows the results of wavelet filtering of the SSEP signal. The stimulation was a single pulse at 0 ms. The SSEPs were well-localized after stimulation onset and could be extracted into frequency bands in the range of 0-1000 Hz (A6-D3). Fig. 3.3 (b) shows the same signal in the time-frequency domain using the continuous wavelet transform (CWT). Based on the traditional cutoff between N10 and HFOs, the two components can be easily identified from the CWT scalogram [24]. Furthermore, the two components exhibit different shapes in the time-frequency domain. While the N10 component is represented as a globule, the HFOs are shown as a long strand that stretches from 300 to 1000 Hz. Fig. 3.3 (c) shows the SSEP waveform changes at 10 minutes of recovery from one 3-min and one 7-min subject. While the 7-min SSEPs were mainly flat, the 3-min SSEP amplitudes were larger than baseline values. This increase could have been related to selective injury of the inhibitory RT neurons [16]–[19].

Fig. 3.4 (a) and (b) shows the progression of N10 and HFO amplitudes during the continuously monitored phase of the experiment. The separation of N10 between the two groups was statistically significant from 2 to 7 minutes post-ROSC (average p-value: 0.013), and the separation of HFO was statistically significant from 7 to 11 minutes post-ROSC (average p-value: 0.022). Fig. 3.4 (c) and (d) shows the progression of GCIs between N10 and HFOs in both directions. The separations of the GCIs in both directions between the 3-min and 7-min groups were not statistically significant. In the 3-min cases, the HFO to N10 GCI dipped below zero in the first 15 minutes post-ROSC because of the asynchronous recoveries of N10 and HFOs [26]. The negative values in GCI should be interpreted as the joint AR model performing worse than the separate AR models because the TC circuit was in a different state compared to baseline.

3.4.1 Discussion

Although the separation of HFO to N10 GCIs between the two groups was not statistically significant, the average of the 7-min GCI was always lower than that of the 3-min group, indicating that GCI can reflect the level of injury. The statistical insignificance was due to the large variations in GCI post-ROSC in the 7-min group. Future work will address this issue by not overfitting to the baseline data and repeating in more rats. The insignificance in the case of N10 to HFO was expected because the physiology does not support a N10 to HFO causal relationship [24]. Compared to the amplitude measures, the HFO to N10 GCI showed a smoother transition during 7-min CA instead of an instant drop. Interestingly, the GCI measure revealed a TC dissociation in the 3-min group, which we assumed to suffer no neurological injury.

Similarly to our previous studies, the amplitude and the new noninvasive measures highlighted the distinction of the first 5-15 minutes post-ROSC from the rest of the ROSC period [14], [15], [18]. The noninvasive nature of the new SSEP GCI measure invites possibilities of testing the effect of interventions to the TC circuit during this crucial period. This also presents an opportunity to characterize the SSEP waveforms in relation the areas that are likely to generate them. The implications of these waveforms and their relationships to prognosis will be further studied.

Focused ultrasound has been shown to have both excitatory and inhibitory effects when applied to brain neural tissue [32]. Specifically, low-intensity focused ultrasound (LIFU) targeting the thalamus has been shown to reduce the amount of time required for rats to show pinch response and voluntary movement from intraperitoneal ketamine-xylazine anesthesia [33]. Another study in human focused the ultrasound sonification on ventro-posterior lateral (VPL) nucleus of thalamus and found inhibition of the P14 thalamic SSEP component and worse discrimination task performance compared to control subjects [34]. Similar inhibitory effect was found in a porcine model of LIFU targetting the VPL nucleus [35]. In a more recent and exciting clinical study, LIFU to the thalamus was delivered to three patients with chronic disorders of consciousness, and two of the three patients showed exhibited clinically significant increases in behavioral responsiveness [36]. While currently both excititory and inhibitory effects have been demonstrated with LIFU onto the sensory thalamus, there has been no study on the effect of LIFU onto the sensory thalamus in the acute phase after cardiac arrest. The stimulation parameters also need to be further studied to achieve excititory or inhibitory effects as idealized.

Vagus nerve is the main nerve of the parasympathetic nervous system and controls digestions, heart rate, respirations among other things. Vagus nerve stimulation has been approved by the Food and Drug Administration as treatment for epilepsy, depression, and stroke [37]–[39]. Recently, many studies have found vagus nerve stimulation to provide neuroprotection after cardiac arrest[40]–[43]. However, all of these studies evaluated damage to the hippocampal CA1 neurons. Therefore, future studies should evaluate the neuroprotective effects of vagus nerve stimulation to the thalamocortical and reticular thalamic neurons.

3.5 Conclusion

The novel SSEP GCI measure was able to show thalamocortical dissociation in the first 10 minutes post-ROSC, and the level of dissociation was associated with the level of injury.

3.6 Acknowledgement

The work for this chapter was performed with collaboration with Ariel Slepyan, and under the guidance of Dr. Yu Guo, Dr. Payam Gharibani, Dr. Trac Duy Tran, Dr. Romergryko Geocadin, Dr. Nitish Thakor.

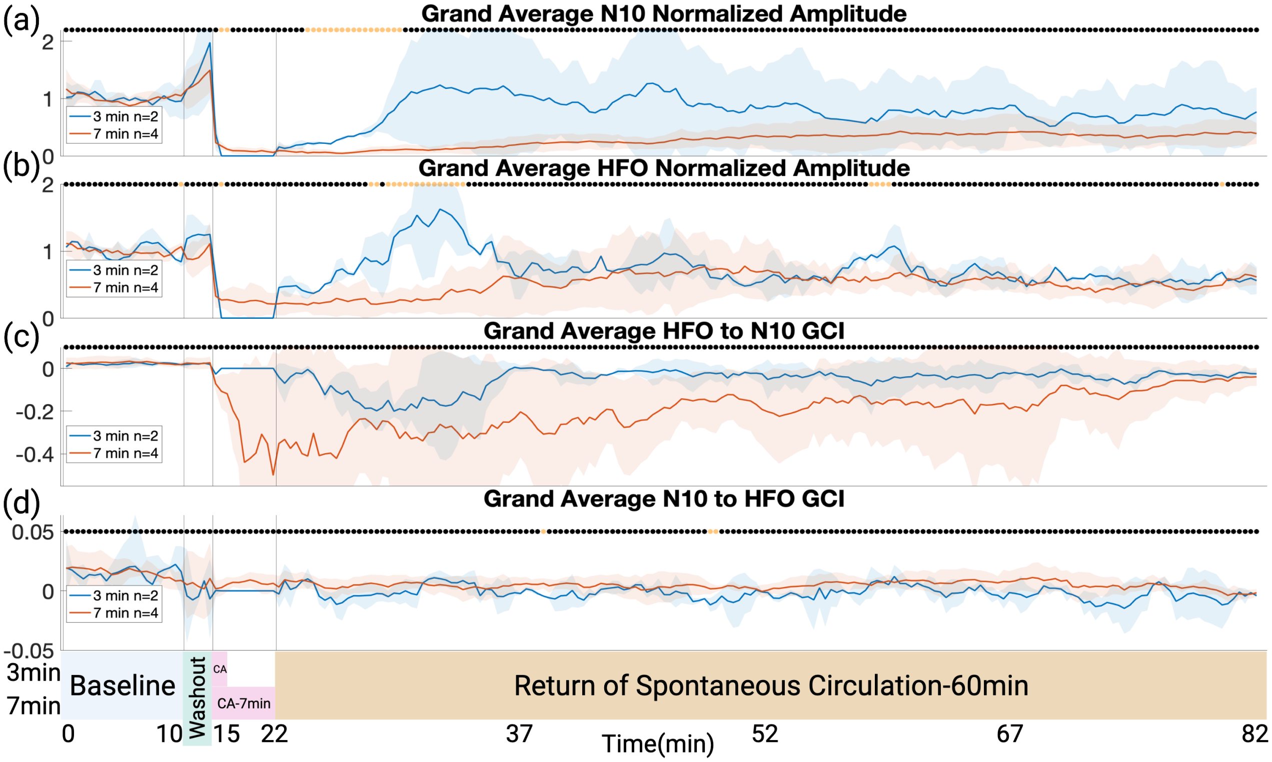

Figure 3.4: SSEP N10 and HFO amplitudes and GCIs for both the 3-min and 7-min groups. Both the mean and the standard deviation range were shown for each metric. Two-sample t tests were performed at each time point to test the alternative hypothesis that the samples from the 3-min and 7-min groups were from different populations. Insignificant test results were shown as black dots, and significant results as orange dots on the top of each plot. (a) N10 amplitudes were stable during baseline, increased during anesthesia washout, and dropped to almost zero during CA. During ROSC, N10 recovered earlier in the 3-min cases, and N10 in both groups converged at the end of the 60-minute recording period to 50-80% of baseline. (b) Similarly, HFO amplitudes were stable during baseline, increased during washout, and dropped during CA. During recovery, HFO amplitudes for the 3-min group initially increased above baseline levels but converged with the HFO amplitudes for the 7-min group. The HFO amplitudes for both groups recovered to 80% of baseline at the end of the 60 minutes. (c) In the 3-min cases, the HFO to N10 GCI dipped below zero in the first 15 minutes post-ROSC. In the 7-min cases, the HFO to N10 GCI quickly dropped to -0.4 during CA and slowly approached the level of the 3-min group. (d) N10 to HFO GCIs were close to 0 for the duration of the experiment. Created with Biorender.com

References

[1] M. S. Sekhon, P. N. Ainslie, and D. E. Griesdale, "Clinical pathophysiology of hypoxic ischemic brain injury after cardiac arrest: A "two-hit" model," *Critical Care*, vol. 21, no. 1, pp. 1–10, 2017.

[2] A. O. Rossetti, A. A. Rabinstein, and M. Oddo, "Neurological prognostication of outcome in patients in coma after cardiac arrest," *The Lancet Neurology*, vol. 15, no. 6, pp. 597–609, 2016.

[3] G. B. Young, "Neurologic prognosis after cardiac arrest," *New England Journal of Medicine*, vol. 361, no. 6, pp. 605–611, 2009.

[4] J. Elmer, C. Torres, T. P. Aufderheide, M. A. Austin, C. W. Callaway, E. Golan, H. Herren, J. Jasti, P. J. Kudenchuk, D. C. Scales, *et al.*, "Association of early withdrawal of life-sustaining therapy for perceived neurological prognosis with mortality after cardiac arrest," *Resuscitation*, vol. 102, pp. 127–135, 2016.

[5] I. Harukuni and A. Bhardwaj, "Mechanisms of brain injury after global cerebral ischemia," *Neurologic clinics*, vol. 24, no. 1, pp. 1–21, 2006.

[6] E. L. Fink, J. Wisnowski, R. Clark, R. P. Berger, A. Fabio, A. Furtado, S. Narayan, D. C. Angus, R. S. Watson, C. Wang, *et al.*, "Brain mr imaging and spectroscopy for outcome prognostication after pediatric cardiac arrest," *Resuscitation*, vol. 157, pp. 185–194, 2020.

[7] Y. Guo, S.-M. Cho, Z. Wei, Q. Wang, H. R. Modi, P. Gharibani, H. Lu, N. V. Thakor, and R. G. Geocadin, "Early thalamocortical reperfusion leads to neurologic recovery in a rodent cardiac arrest model," *Neurocritical Care*, pp. 1–13, 2022.

[8] S. M. Sherman and R. W. Guillery, *Exploring the thalamus and its role in cortical function*. MIT press, 2006.

[9] M. F. Wells, R. D. Wimmer, L. I. Schmitt, G. Feng, and M. M. Halassa, "Thalamic reticular impairment underlies attention deficit in ptchd1y/- mice," *Nature*, vol. 532, no. 7597, pp. 58–63, 2016.

[10] J. E. Jan, R. J. Reiter, M. B. Wasdell, and M. Bax, "The role of the thalamus in sleep, pineal melatonin production, and circadian rhythm sleep disorders," *Journal of pineal research*, vol. 46, no. 1, pp. 1–7, 2009.

[11] N. D. Schiff, "Central thalamic contributions to arousal regulation and neurological disorders of consciousness," *Annals of the New York Academy of Sciences*, vol. 1129, no. 1, pp. 105–118, 2008.

[12] B. L. Edlow, R. L. Haynes, E. Takahashi, J. P. Klein, P. Cummings, T. Benner, D. M. Greer, S. M. Greenberg, O. Wu, H. C. Kinney, *et al.*, "Disconnection of the ascending arousal system in traumatic coma," *Journal of Neuropathology & Experimental Neurology*, vol. 72, no. 6, pp. 505–523, 2013.

[13] A. Maybhate, C. Chen, N. V. Thakor, and X. Jia, "Effect of hypothermia on the thalamocortical function in the rat model," in *2012 Annual International Conference of the IEEE Engineering in Medicine and Biology Society*, IEEE, 2012, pp. 4680–4683.

[14] D. Wu, A. Bezerianos, D. Sherman, X. Jia, and N. V. Thakor, "Causal interactions between thalamic and cortical lfps following hypoxic-ischemic brain injury," in *2011 5th International IEEE/EMBS Conference on Neural Engineering*, IEEE, 2011, pp. 184–187.

[15] C. Chen, A. Maybhate, D. Israel, N. V. Thakor, and X. Jia, "Assessing thalamocortical functional connectivity with granger causality," *IEEE Transactions on Neural Systems and Rehabilitation Engineering*, vol. 21, no. 5, pp. 725–733, 2013.

[16] H. T. Ton, K. Raffensperger, and M. Shoykhet, "Early thalamic injury after resuscitation from severe asphyxial cardiac arrest in developing rats," *Frontiers in cell and developmental biology*, p. 3521, 2021.

[17] M. Shoykhet, D. J. Simons, H. Alexander, C. Hosler, P. M. Kochanek, and R. S. Clark, "Thalamocortical dysfunction and thalamic injury after asphyxial cardiac arrest in developing rats," *Journal of Neuroscience*, vol. 32, no. 14, pp. 4972–4981, 2012.

[18] J. Muthuswamy, T Kimura, M. Ding, R Geocadin, D. Hanley, and N. Thakor, "Vulnerability of the thalamic somatosensory pathway after prolonged global hypoxic–ischemic injury," *Neuroscience*, vol. 115, no. 3, pp. 917–929, 2002.

[19] R. G. Geocadin, J. Muthuswamy, D. L. Sherman, N. V. Thakor, and D. F. Hanley, "Early electrophysiological and histologic changes after global cerebral ischemia in rats," *Movement disorders*, vol. 15, no. S1 S1, pp. 14–21, 2000.

[20] H. W. Bedell, N. J. Schaub, J. R. Capadona, and E. S. Ereifej, "Differential expression of genes involved in the acute innate immune response to intracortical microelectrodes," *Acta biomaterialia*, vol. 102, pp. 205–219, 2020.

[21] B. Lachance, Z. Wang, N. Badjatia, and X. Jia, “Somatosensory evoked potentials and neuroprognostication after cardiac arrest,” *Neurocritical care*, vol. 32, no. 3, pp. 847–857, 2020.

[22] R Gobbelé, T. Waberski, H Simon, E Peters, F Klostermann, G Curio, and H Buchner, “Different origins of low-and high-frequency components (600 hz) of human somatosensory evoked potentials,” *Clinical neurophysiology*, vol. 115, no. 4, pp. 927–937, 2004.

[23] C. B. Maciel, A. O. Morawo, C. Y. Tsao, T. S. Youn, D. R. Labar, E. O. Rubens, and D. M. Greer, “Ssep in therapeutic hypothermia era,” *Journal of Clinical Neurophysiology*, vol. 34, no. 5, pp. 469–475, 2017.

[24] I. Ozaki and I. Hashimoto, “Exploring the physiology and function of high-frequency oscillations (hfos) from the somatosensory cortex,” *Clinical neurophysiology*, vol. 122, no. 10, pp. 1908–1923, 2011.

[25] T Götz, T Milde, G Curio, S Debener, T Lehmann, L Leistritz, O. Witte, H Witte, and J Haueisen, “Primary somatosensory contextual modulation is encoded by oscillation frequency change,” *Clinical Neurophysiology*, vol. 126, no. 9, pp. 1769–1779, 2015.

[26] D. Wu, A. Bezerianos, H. Zhang, X. Jia, and N. V. Thakor, “Exploring high-frequency oscillation as a marker of brain ischemia using s-transform,” in *2010 Annual International Conference of the IEEE Engineering in Medicine and Biology*, IEEE, 2010, pp. 6099–6102.

[27] N. V. Thakor, G. Xin-Rong, S. Yi-Chun, and D. F. Hanley, “Multiresolution wavelet analysis of evoked potentials,” *IEEE transactions on biomedical engineering*, vol. 40, no. 11, pp. 1085–1094, 1993.

[28] C. W. Granger, “Investigating causal relations by econometric models and cross-spectral methods,” *Econometrica: journal of the Econometric Society*, pp. 424–438, 1969.

[29] M. Ding, Y. Chen, and S. L. Bressler, “Granger causality: Basic theory and application to neuroscience,” *Handbook of time series analysis: recent theoretical developments and applications*, pp. 437–460, 2006.

[30] L. Barnett and A. K. Seth, “The mvgc multivariate granger causality toolbox: A new approach to granger-causal inference,” *Journal of neuroscience methods*, vol. 223, pp. 50–68, 2014.

[31] H. Akaike, “A new look at the statistical model identification,” *IEEE transactions on automatic control*, vol. 19, no. 6, pp. 716–723, 1974.

[32] X. Jiang, O. Savchenko, Y. Li, S. Qi, T. Yang, W. Zhang, and J. Chen, "A review of low-intensity pulsed ultrasound for therapeutic applications," *IEEE Transactions on Biomedical Engineering*, vol. 66, no. 10, pp. 2704–2718, 2018.

[33] S.-S. Yoo, H. Kim, B.-K. Min, and S. P. E. Franck, "Transcranial focused ultrasound to the thalamus alters anesthesia time in rats," *Neuroreport*, vol. 22, no. 15, p. 783, 2011.

[34] W. Legon, L. Ai, P. Bansal, and J. K. Mueller, "Neuromodulation with single-element transcranial focused ultrasound in human thalamus," *Human brain mapping*, vol. 39, no. 5, pp. 1995–2006, 2018.

[35] R. F. Dallapiazza, K. F. Timbie, S. Holmberg, J. Gatesman, M. B. Lopes, R. J. Price, G. W. Miller, and W. J. Elias, "Noninvasive neuromodulation and thalamic mapping with low-intensity focused ultrasound," *Journal of neurosurgery*, vol. 128, no. 3, pp. 875–884, 2017.

[36] J. A. Cain, N. M. Spivak, J. P. Coetzee, J. S. Crone, M. A. Johnson, E. S. Lutkenhoff, C. Real, M. Buitrago-Blanco, P. M. Vespa, C. Schnakers, *et al.*, "Ultrasonic thalamic stimulation in chronic disorders of consciousness," *Brain Stimulation: Basic, Translational, and Clinical Research in Neuromodulation*, vol. 14, no. 2, pp. 301–303, 2021.

[37] C. B. Nemeroff, H. S. Mayberg, S. E. Krahl, J. McNamara, A. Frazer, T. R. Henry, M. S. George, D. S. Charney, and S. K. Brannan, "Vns therapy in treatment-resistant depression: Clinical evidence and putative neurobiological mechanisms," *Neuropsychopharmacology*, vol. 31, no. 7, pp. 1345–1355, 2006.

[38] B. Koo, S. D. Ham, S. Sood, and B. Tarver, "Human vagus nerve electrophysiology: A guide to vagus nerve stimulation parameters," *Journal of clinical neurophysiology*, vol. 18, no. 5, pp. 429–433, 2001.

[39] J. Dawson, C. Y. Liu, G. E. Francisco, S. C. Cramer, S. L. Wolf, A. Dixit, J. Alexander, R. Ali, B. L. Brown, W. Feng, *et al.*, "Vagus nerve stimulation paired with rehabilitation for upper limb motor function after ischaemic stroke (vns-rehab): A randomised, blinded, pivotal, device trial," *The Lancet*, vol. 397, no. 10284, pp. 1545–1553, 2021.

[40] B. Kim, I. Park, J. H. Lee, S. Kim, M. J. Lee, and Y. H. Jo, "Effect of electrical vagus nerve stimulation on cerebral blood flow and neurological outcome in asphyxial cardiac arrest model of rats," *Neurocritical Care*, vol. 30, no. 3, pp. 572–580, 2019.

[41] P. Sun, J. Wang, S. Zhao, Z. Yang, Z. Tang, N. Ravindra, J. Bradley, J. P. Ornato, M. A. Peberdy, and W. Tang, "Improved outcomes of cardiopulmonary resuscitation in rats treated with vagus nerve stimulation and its potential mechanism," *Shock: Injury, Inflammation, and Sepsis: Laboratory and Clinical Approaches*, vol. 49, no. 6, pp. 698–703, 2018.

[42] W.-j. Shao, T.-t. Shu, S. Xu, L.-c. Liang, J. M. Le Grange, Y.-r. Zhou, H. Huang, Y. Cai, Q. Zhang, and P. Sun, "Left-sided vagus nerve stimulation improves cardiopulmonary resuscitation outcomes in rats as effectively as right-sided vagus nerve stimulation," *World Journal of Emergency Medicine*, vol. 12, no. 4, p. 309, 2021.

[43] R. C. Choudhary, U. Ahmed, M. Shoaib, E. Alper, A. Rehman, J. Kim, K. Shinozaki, B. T. Volpe, S. Chavan, S. Zanos, *et al.*, "Threshold adjusted vagus nerve stimulation after asphyxial cardiac arrest results in neuroprotection and improved survival," *Bioelectronic Medicine*, vol. 8, no. 1, pp. 1–12, 2022.

Chapter 4

Low-Intensity Focused Ultrasound Neuromodulation of a Rodent's Spinal Cord Leads to Motor Evoked Potential Suppression

4.1 Acknowledgement

The work for this chapter was a collaboration project with Yohannes Tsehay, Yinuo Zeng, Carly Weber-Levine, Tolulope Awosika, Max Kerensky, Andrew M. Hersh, Kelly Jiang, Meghana Bhimreddy, Stuart J. Bauer, John N. Theodore, Victor M. Quiroz, Ian Suk, Dr. Safwan Alomari, Dr. Junfeng Sun, Dr. Shanbao Tong, Dr. Nitish Thakor, Dr. Joshua C. Doloff, Dr. Amir Manbachi, Dr. Nicholas Theodore.

4.2 Introduction

Ultrasound (US) technology has increasingly been applied to modulate neural activity and can elicit both excitatory and inhibitory effects when applied to neural brain tissue [1]. US neuromodulation can be achieved using high- or low- intensity waves [2]. While high intensity US can ablate tissues, low intensity focused ultrasound (LIFUS) has emerged as an effective, safe, and non-invasive tool for the transient modulation of neural activity using intensities in the range of 0.02-1 $\mathrm{W\,cm^{-2}}$. Compared to other neuromodulation tools, LIFUS can achieve high spatial resolution and deep penetration without requiring any genetic alterations [3].

LIFUS has predominantly been studied for cranial and peripheral nerve applications, with few studies investigating its effects on spinal cord tissue [3]–[7]. Li et al. used US waves to drive piezoelectric stimulation pulses, which induced MEPs in the hindlimbs and restored locomotion in paralyzed rats with thoracic spinal cord injury [8]. Liao et al. demonstrated that US can activate spinal cord neurocircuits and contract the soleus muscle without increasing inflammatory factors [9]. LIFUS directed at the spinal cord has the potential to help with the treatment of movement disorders. Therefore, we sought to characterize the ability of LIFUS applied to the spinal cord to modulate the transmission of motor signals. We hypothesized that LIFUS would alter the amplitude of MEPs in muscle groups distal to the area of stimulation.

4.3 Materials and Methods

4.3.1 Animal Preparation

All experimental procedures were approved by the Johns Hopkins Medical Institute Animal Care and Use Committee and conducted in accordance with the National Institutes of Health guidelines for the care and use of laboratory animals. Male adult Sprague-Dawley rats (n = 10, 250-300 g, 15 weeks old; Charles River Laboratories) were used in this study and were housed at a temperature of 25°C with a 12/12-h light/dark cycle. Anesthesia was initially induced with 2% isoflurane (Baxter, IL, USA) carried by oxygen at 4 L/min via a nose cone. The rat was placed on a surgical platform with a warming pad placed under the animal and the temperature was maintained at 37 ± 0.5°C throughout the entire experiment.

4.3.2 Electrode Placement

The rat was placed on a stereotactic apparatus (Stoelting, USA) and the head was fixed with ear bars. The head of the rat was shaved, and a midline incision was made to expose the cranium. Two holes were drilled in the skull over the motor cortex using a standard dental drill (Vogue Professional 6000, USA). Screw electrodes (E363/20, Plastics One, Inc, Roanoke, VA) were inserted 2 mm posterior to the bregma and 2 mm lateral to the midline and were implanted at a depth of 0.75 mm so that they contacted the dura mater without damaging its integrity [10]. Two ground needle electrodes were placed, with one in the soft tissue bulk of the left forelimb and the other in the proximal tail. Two recording needle electrodes were placed in the soleus of the left hindlimb and two electrodes were placed in the brachioradialis of the left forelimb.

4.3.3 Experiment Procedures

Following electrode placement, the back of the rat was shaved, and a midline incision was made from approximately the T10 to T13 vertebral levels. A subperiosteal dissection was performed to expose the spinous process, which were then clamped at T10 and T13 by forceps attached to ball joint arms to confer stability. Laminectomies were performed at T11 and T12 using a high-speed dental drill (Aseptico AEU-10, USA) to expose the spinal cord.

Following laminectomy, anesthesia was maintained via intraperitoneal injection of ketamine (100 mg/kg) with xylazine (10 mg/kg). All electrodes were then connected to an intraoperative neurophysiological monitoring system (IOM system, Nicolet Biomedical, USA) to record MEPs. The two screw electrodes on the skull served as stimulation electrodes, with the left electrode connected to the negative output and the right electrode connected to the positive output. The needle electrode pair at the right hindlimb and left forelimb were used as recording electrodes. The sonication site was situated in the distal thoracic spinal cord, and therefore we hypothesized that LIFUS would only affect the hindlimb MEPs, while the forelimb MEPs would serve as a control for each subject.

4.3.4 Low Intensity Ultrasound Neuromodulation

The ultrasound neuromodulation system consists of two function generators, a RF amplifier, an ultrasound transducer (Olympus Panametrics V301, USA) and a custom-made acoustic collimator. One function generator outputs a square wave to trigger the second function generator, which outputs a sine wave to form a pulsed sine wave signal. The RF amplifier receives the pulsed signal and drives the ultrasound transducer. The acoustic collimator couples the ultrasound wave from the transducer to the target region. Prior studies have used similar setups [11].

At the time of the study, no prior literature existed on ultrasound interventions for the spinal cord, and parameters were therefore adapted from investigations into the brain and peripheral nerves [12]–[15]. The probe modulated for both 5 minute and 10-minute stimulation periods using a fundamental frequency (f0) of 500 kHz, tone burst duration of 500 µs, and a 50% duty cycle.

The ultrasound transducer was secured onto the acoustic collimator filled with ultrasound transmission gel (Aquasonic 100, Parker Laboratories). The apparatus was fixed on a probe stand and carefully lowered to the exposed spinal cord (T11 and T12). Additional gel interfaced the apex of the cone and the spinal cord. The probe rested at this fixed location throughout the experiment. A hydrophone (ONDA HNR-0500, USA) was used to calculate the root-mean-square (RMS) pressures throughout the middle portion of the bursts as 0.0297 MPa, while the instantaneous intensities were 0.060 W/cm2.

After setting up the ultrasound neuromodulation system, a five-minute sonication trial started. All ten rats received a five-minute sonication trial and five of these rats received an additional ten-minute sonication trial. Within each trial, there were three periods: baseline period, during-modulation period and post-modulation period. In the five-minute sonication trial, the baseline, during-modulation and post-modulation period last for 1 minute, 5 minutes and 5 minutes, respectively. While for the ten-minute sonication trial, the baseline, during-modulation and post-modulation period last for 2 minutes, 10 minutes and 5 minutes, respectively. There's a 10-minute recovery time between the five-minute and ten-minute trial.

4.3.5 Electrophysiology Recording Parameters

The electrical stimulation to induce MEPs was controlled by the IOM system. To induce one MEP, a train of electrical stimulation consisting of 5 square waves was used. Each square wave lasts 100 μs and waves were separated by 2 ms, resulting in a frequency of 500 Hz. The stimulus intensity was set at 8mA. This intensity is high enough to induce an obvious MEP without damaging the tissue [10]. Each train of electrical stimulation would induce one MEP signal, and one train was given every second for 20 seconds and then stopped for the following 40 seconds, which ensured that the rat recovered from the electrical stimulation. As a result, each experiment trial was separated into multiple 1-minute-windows and each window was named according to the period and it's time order.

The IOM system recorded the signal automatically, and a notch filter (60 Hz) was used to eliminate electric grid noise. MEP signals were collected immediately after the system setup and the MEPs were averaged over 20 signals within each 1-minute-window. It was monitored closely until the MEP amplitude was stable. Baseline MEP was collected for 1 minute after ensuring the stability and then the ultrasound modulation began. For the ten-minute sonication trial, an additional 1-minute baseline was recorded which was used to ensure the baseline was stable enough after the previous five-minute stimulation trial. Following the modulation period, the ultrasound was turned off and post-modulation MEPs were acquired for an additional five minutes.

4.3.6 Data Processing and Statistical Analysis

MEPs were extracted from raw recordings and self-developed MATLAB scripts (MATLAB version 2021b, The Mathworks, Inc.) was used to process the data. The MEP signals were also inspected manually to ensure it doesn't contain obvious artifacts or noises. MEP peak amplitudes and latencies of the positive and negative peaks were measured by searching for the global extremum in the extracted data. Peak amplitude is defined as the difference between the amplitude of the peak and the average amplitude of the baseline period. Peak latency is defined as the time difference between stimulation onset and the peak. The peak-to-peak amplitude was then calculated by subtracting the negative peak amplitude from the positive peak amplitude. Within each trial, all calculated MEP amplitudes and latencies in each 1-minute-window were normalized relative to the average of that metric in the baseline of each animal.

The averages of the normalized amplitudes or latencies in all the 1-minute-windows within each period were calculated for statistical analysis. One-way Kruskal-Wallis tests were performed on the amplitudes and latencies of the three periods in both the 5-min and 10-min trials to test the alternative hypothesis that the measures of the three periods were sampled from different distributions. If the result was significant, post hoc Dunn tests were performed to identify statistically significant differences of the measurements between

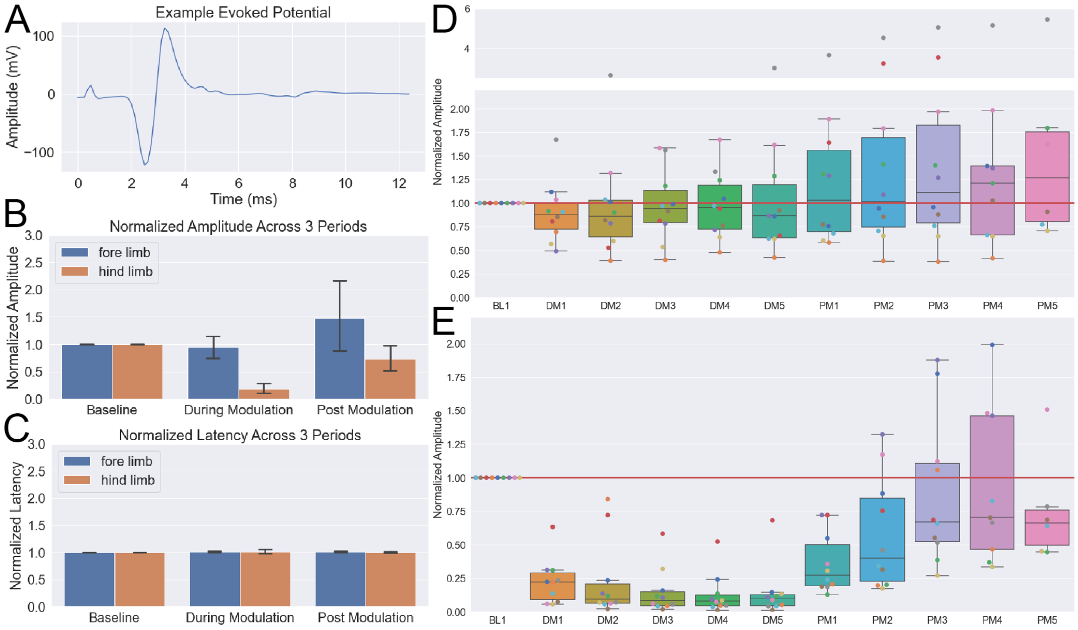

Figure 4.1: 5-minute sonication result (A) Representative motor evoked potential; (B) Normalized amplitude across the baseline, the during-modulation and the post-modulation periods; (C) Normalized latency across the three stages; (D) Boxplot of normalized forelimb amplitude; (E) Boxplot of normalized hindlimb amplitude. **, $p < 0.01$, ***, $p < 0.001$

each pair of periods. Wilcoxon rank sum tests were also performed to compare each of the baseline, during-modulation, and post-modulation periods in the 5-min trials to the periods in the 10-min trials. Lastly, a linear regression was fitted to the post-modulation period for both the 5-min and 10-min trials for each animal, and a Wilcoxon rank sum test was performed on the distribution of the recovery slopes in the two trials

4.4 Results

MEPs were recorded from both the forelimb and the hindlimb in the 5-minute (Fig. 4.1A) and 10-minute (Fig. 4.2A) sonication trials and were

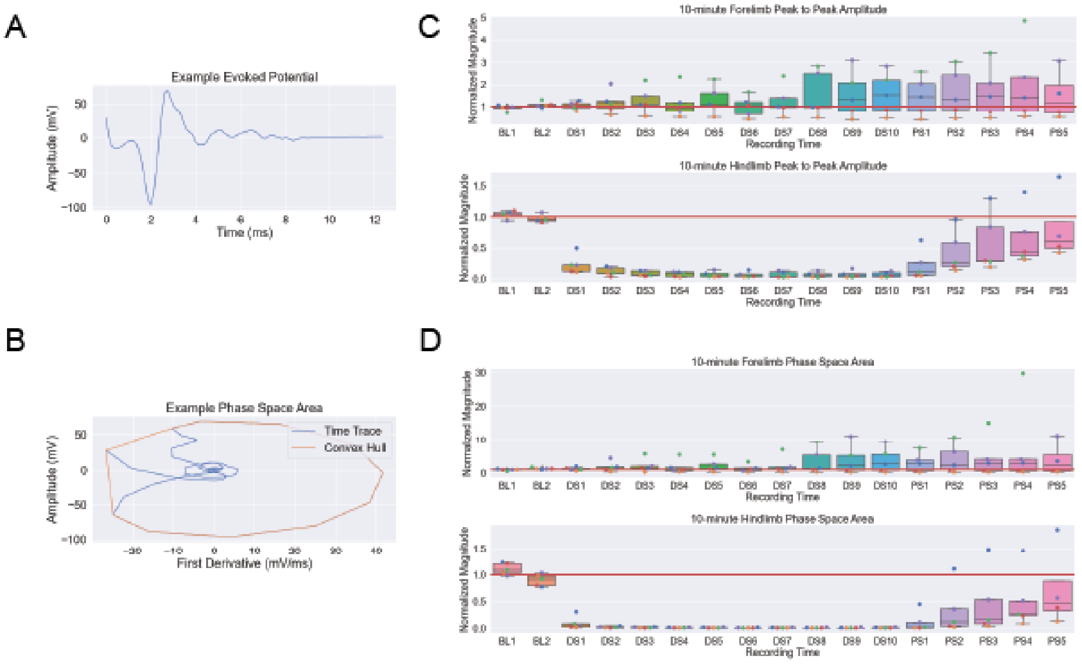

Figure 4.2: 10-minute sonication result (A) Representative motor evoked potential; (B) Normalized amplitude across the baseline, the during modulation state and the post modulation state; (C) Normalized latency across the three stages; (D) Boxplot of normalized forelimb amplitude; (E) Boxplot of normalized hindlimb amplitude. **, $p < 0.01$, ***, $p < 0.001$

depicted as boxplots. An obvious depression of the MEP amplitude in the hindlimb was observed immediately after the beginning of the sonication. The suppressed MEP amplitude recovered gradually during the post-modulation period (Figs. 4.1E and 4.2E). As a comparison, no obvious variation was found in the forelimb MEP amplitude (Figs. 4.1D and 4.2D). In both the five-minute and ten-minute trials, forelimb MEP amplitude did not show any statistically significant differences between the three periods ($\chi^2(2)=1.54$, $p=0.46$ for five-minute trials; $\chi^2(2)=0.44$, $p=0.80$ for ten-minute trials) (Figs. 4.1B and 4.2B). In contrast, hindlimb MEP amplitude showed a statistically significant decrease during neuromodulation, and a gradual recovery to baseline in both

5-minute and 10-minute sonication trials ($\chi^2(2)$=19.17, p<0.001 for five-minute trials; $\chi^2(2)$=10.89, p<0.01 for ten-minute trials) (Figs. 4.1E and 4.2E). Post hoc analyses showed statistically significant differences between baseline and during-modulation period for the 5- (p<0.001) and 10-minute (p<0.01) trials, and between during-modulation and post-modulation periods for the 5-minute cohort (p<0.01) while trending towards significance in the ten-minute case (p=0.08) Figs. 4.1B and 4.2B). Wilcoxon rank sum tests also showed statistically significant differences between forelimb and hindlimb MEP amplitudes in the during-modulation period for both the 5-minute (p<0.001) and the 10-minute cohorts (p<0.01) (Figs. 4.1B and 4.2B).

There were two outliers in the 5-minute forelimb MEP recordings that were four standard deviations away from the mean, so the statistical tests were repeated without the outliers as a measure of robustness. These tests illustrated that the result was not statistically significant even without the outliers ($\chi^2(2)$=0.77, p=0.68).

MEP amplitude showed a general recovery after modulation. The recovery trajectory of each subject was fitted with a linear regression with respect to time, and a Wilcoxon rank-sum test was performed on the distribution of the recovery slope. The test confirmed that there was no statistically significant difference in the recovery speed between the 5-minute and the 10-minute groups (p=0.59). In the 5-minute groups, the fitted line recovered back to baseline after 5 minutes of recovery. However, in the 10-minute groups, the fitted line only recovered to 80% of baseline after 5 minutes of recovery. The average recovery speed was 20% of baseline per minute for the 5-minute group, and 14% of baseline per minute for the 10-minute group.

As for the latencies of both the positive and negative peaks, it only showed statistically significant differences between the stages for the 5-minute forelimb positive peak and 5-minute hindlimb negative peak (5-minute forelimb positive peak 2(2)=7.26, p=0.027, 5-minute hindlimb negative peak χ^2(2)=6.31, p=0.042) (Figs. 4.1C and 4.2C).

4.5 Discussion

The main hypothesis we are testing in this paper is that ultrasound neuromodulation on the spinal cord (T11 and T12) would alter the hindlimb MEPs while keeping the forelimb MEPs remain unchanged. Figures 4.1E and 4.2E showed a significant depression effect of the LIFUS on the hindlimb MEP amplitudes, and the statistical analysis also showed significant changes in the hindlimb MEP amplitudes. The MEP amplitudes were kept depressed during modulation for both 5-minute and 10-minute sonication, and a longer recovery time was observed for the 10-minute sonication. On the other hand, the forelimb MEP amplitudes didn't show significant change during modulation. Other than the amplitudes, the MEP latencies of both 5-minute and 10-minute sonication didn't show significant change. This result indicates that LIFUS on the dorsal spinal cord has a depression effect, and the longer the sonication is, the longer it takes to recover to baseline. The unchanged latency indicates that LIFUS would not affect the nerve conduction velocity.

4.6 Conclusion

Low intensity focused ultrasound (LIFUS) neuromodulation can causes transient suppression of MEP signals.

References

[1] X. Jiang, O. Savchenko, Y. Li, S. Qi, T. Yang, W. Zhang, and J. Chen, "A review of low-intensity pulsed ultrasound for therapeutic applications," *IEEE Transactions on Biomedical Engineering*, vol. 66, no. 10, pp. 2704–2718, 2018.

[2] H. Baek, K. J. Pahk, and H. Kim, "A review of low-intensity focused ultrasound for neuromodulation," *Biomedical Engineering Letters*, vol. 7, no. 2, pp. 135–142, 2017.

[3] X. Liu, F. Qiu, L. Hou, and X. Wang, "Review of noninvasive or minimally invasive deep brain stimulation," *Frontiers in Behavioral Neuroscience*, vol. 15, 2021.

[4] A. Fomenko, K.-H. S. Chen, J.-F. Nankoo, J. Saravanamuttu, Y. Wang, M. El-Baba, X. Xia, S. S. Seerala, K. Hynynen, A. M. Lozano, *et al.*, "Systematic examination of low-intensity ultrasound parameters on human motor cortex excitability and behavior," *Elife*, vol. 9, e54497, 2020.

[5] A. Fomenko, C. Neudorfer, R. F. Dallapiazza, S. K. Kalia, and A. M. Lozano, "Low-intensity ultrasound neuromodulation: An overview of mechanisms and emerging human applications," *Brain stimulation*, vol. 11, no. 6, pp. 1209–1217, 2018.

[6] M. Zhang, B. Li, X. Lv, S. Liu, Y. Liu, R. Tang, Y. Lang, Q. Huang, and J. He, "Low-intensity focused ultrasound-mediated attenuation of acute seizure activity based on eeg brain functional connectivity," *Brain Sciences*, vol. 11, no. 6, p. 711, 2021.

[7] E. J. Bubrick, N. J. McDannold, and P. J. White, "Low intensity focused ultrasound for epilepsy-a new approach to neuromodulation," *Epilepsy Currents*, p. 15 357 597 221 086 111, 2022.

[8] S. Li, M. Alam, R. U. Ahmed, H. Zhong, X.-Y. Wang, S. Ng, and Y.-P. Zheng, "Ultrasound-driven piezoelectric current activates spinal cord neurocircuits and restores locomotion in rats with spinal cord injury," *Bioelectronic medicine*, vol. 6, no. 1, pp. 1–9, 2020.

[9] Y.-H. Liao, M.-X. Chen, S.-C. Chen, K.-X. Luo, B. Wang, Y. Liu, and L.-J. Ao, "Effects of noninvasive low-intensity focus ultrasound neuromodulation on spinal cord neurocircuits in vivo," *Evidence-Based Complementary and Alternative Medicine*, vol. 2021, 2021.

[10] S. Iyer, A. Maybhate, A. Presacco, and A. H. All, "Multi-limb acquisition of motor evoked potentials and its application in spinal cord injury," *Journal of neuroscience methods*, vol. 193, no. 2, pp. 210–216, 2010.

[11] Y. Tufail, A. Yoshihiro, S. Pati, M. M. Li, and W. J. Tyler, "Ultrasonic neuromodulation by brain stimulation with transcranial ultrasound," *nature protocols*, vol. 6, no. 9, pp. 1453–1470, 2011.

[12] B.-K. Min, A. Bystritsky, K.-I. Jung, K. Fischer, Y. Zhang, L.-S. Maeng, S. In Park, Y.-A. Chung, F. A. Jolesz, and S.-S. Yoo, "Focused ultrasound-mediated suppression of chemically-induced acute epileptic eeg activity," *BMC neuroscience*, vol. 12, no. 1, pp. 1–12, 2011.

[13] R. L. King, J. R. Brown, W. T. Newsome, and K. B. Pauly, "Effective parameters for ultrasound-induced in vivo neurostimulation," *Ultrasound in medicine & biology*, vol. 39, no. 2, pp. 312–331, 2013.

[14] S.-S. Yoo, A. Bystritsky, J.-H. Lee, Y. Zhang, K. Fischer, B.-K. Min, N. J. McDannold, A. Pascual-Leone, and F. A. Jolesz, "Focused ultrasound modulates region-specific brain activity," *Neuroimage*, vol. 56, no. 3, pp. 1267–1275, 2011.

[15] M. Plaksin, E. Kimmel, and S. Shoham, "Cell-type-selective effects of intramembrane cavitation as a unifying theoretical framework for ultrasonic neuromodulation," *Eneuro*, vol. 3, no. 3, 2016.

Chapter 5

Grip force and Cortical Responses to Graded Electrocutaneous Stimulation

5.1 Disclaimer

This work was separate from the main focus of the thesis, which is cardiac arrest. It's placed here in the thesis purely for archiving.

5.2 Introduction

Tactile sensory feedback is an integral part of motor control. For upper-limb amputees, the creation of myoelectric prosthetic hands has allowed them to perform simple tasks involved in daily lives. However, these devices lack the ability to provide tactile sensory feedback, and often receive rejections from the users. Therefore, one of the goals in the development of future prosthetic device is the restoration of sensory feedback. Many techniques have been developed to elicit phantom hand sensations in the missing limb, and have shown improvement in prosthetic control and subjectsive user satisfaction [1]–[5]. Sensations elicited include electrical tingling [1], [3], pressure [6], touch [7], vibration [2], and pain [6].

The current challenges in sensory feedback lie in accounting for individual variation and evaluating the feedback objectively. Most of the works use behavior questionnaires to evaluate the quality and effect of sensory feedback [5], [6]. More recently, some studies have developed objective measures such as proprioceptive drift [8] and cortical impact of sensory feedback [9] to evaluate phantom limb perception. These questionnaires and objective measures show effective sensory restoration and prosthetic hand embodiment. In particular, the dynamic functional connectivity analysis in [9] discovers the involvement of multisensory processing areas, faster information transfer, and larger number of connections between sensorimotor processing areas during trials with sensory feedbacks. This finding shows the promises in utilizing brain signals to analyze sensory feedback perception and effectiveness.

In a grip force study with transcutaneous electrical nerve stimulation (TENS) done by D'Anna et al., subjects reported difficulty in generating more than three levels of force [1]. The authors hypothesized that the limiting factor is memorizing the exact force needed for each level, instead of motor control or sensory feedback. However, they did not provide evidence in terms of cognitive processing in the brain. In the same study, electroencephalography (EEG) data was collected and processed into stimulus-locked somatosensory evoked potential (SEP), which exhibited a significant contralateral component at electrode C3 50 ms after stimulation onset. The study also presented scalp topographies consistent with a generator within the post-central gyrus from 45-100 ms. However, the EEG data in this specific study was recorded when subjects were passively receiving the stimulation. Furthermore, the components analyzed are early sensory components not affected by cognitive processing. Therefore, in the current study, we set to explore the cortical processing of novel sensory feedback information with cognitive event related potential (ERP), specifically the P300 component, and the limit of grip force feedback levels.

The P300 component is a large positive deflection happening between 300 to 500 ms post-stimulus. It is also named the P3 component because it is usually the third positive peak in the ERP signals. Sutton et al. first discovered the P300 component in 1965, by presenting target stimuli associated with different probabilities. The uncertain stimulus pair elicited larger P300 component across the visual and auditory sensory modalities compared to the certain stimulus pair [10]. In 1978, Donchin et al. designed the oddball experiment to further elucidate the relationship between stimulus probability and P300 amplitude [11]. In a traditional two-stimulus oddball experiment, an infrequent target stimulus is presented in the background of a frequent standard stimulus. The subjects is asked to respond to the target stimulus by counting or pressing a button. Utilizing the oddball paradigm and a smart design of stimulus category, Kutas et al. discovered that the P300 wave is sensitive to the probability of the stimulus category but not to the probability of the particular stimulus [12].

To compare the P300 component across conditions and subjects groups, the component is often characterized by its peak amplitude, peak latency, and scalp distribution. The peak amplitude is defined as the difference between the mean prestimulus baseline voltage and the largest positive-going peak of the ERP within a time window defined by stimulus modality, task types, and other factors. Peak latency is defined as the time from stimulus onset to the point of the peak in the same time window. The scalp distribution of P300 is summarized as the increase in peak amplitude over the midline electrodes going from frontal to parietal electrodes (Fz, Cz, Pz) [13]. Increase in P300 amplitude is often associated with greater neuronal activity, but P300 amplitude can be smaller when the subjects is uncertain of whether a given stimulus is a target or nontarget. Therefore, if a task is made more difficult, the P300 amplitude might increase because the subjects is devoting more attention to the task, or the amplitude might also decrease because the subjects is uncertain of the category of the stimulus [14]. Thus, there is no simple method to predict the P300 amplitude for more difficult tasks. On the other hand, decrease in peak latency often symbolizes easier stimulus discrimination and task processing. The nature that the shape of P300 depends on the category of the stimulus indicates that the subjects has begun the categorization of the stimulus by the time the difference is significant.

In this study, we present four intensity levels of TENS feedback and ask subjects to generate corresponding forces. The subjects are only trained on three out of the four levels of stimulations, and the last condition is introduced in the last part of the experiment without informing the subjects. We hypothesize that subjects are able to generate four distinct levels of forces, i. e. they do not need to memorize the force levels, and we are able to identify distinct levels of P300 components.

5.3 Methods

5.3.1 subjects

Two intact-limb participants (one male, one female, age 20-21) were recruited and provided written informed consent. The subjects have no known neurological disorder and are right-handed. The study is approved by the Johns Hopkins Medicine Institutional Review Board.

5.3.2 Experiment

5.3.2.1 Sensory Mapping

Targeted TENS was first performed to identify stimulation sites that elicited referred sensation in subjects' right hand. The stimulator Arduino (Uno, Arduino, Italy) controlled a constant current stimulator (DS3, Digitimer Ldt, UK) and sent monophasic square wave pulses through a beryllium copper probe. The ground electrode was placed above the medial nerve on the palm side of the wrist through a 5-mm disposable Ag-Ag/Cl electrode. An amplitude of 0.5-3 mA, frequency of 2-4 Hz, and pulse width of 0.5-4 ms were used while mapping. The entire wrist area was scanned with the stimulating probe. An outline of a hand was used for each subject to indicate which region was activated during stimulation. Once sensory mapping was performed, the positive electrode was placed at the spot eliciting sensation through another Ag-Ag/Cl electrode. For both of our subjects, the positive electrode was placed between the scaphoid and the radius bones on the back side of the hand, and they reported sensation of tingling and pressure in the thenar region of their hand.

5.3.2.2 Threshold Identification

To create individualized stimulation patterns, we performed a psychophysical experiment to determine detection threshold by stimulating the subjects with varying pulse width from a pool of five. The frequency of the stimulation was set to 2 Hz, and the amplitude was set to 1 mA. During each trial, the target site was stimulated for 3 s, and the subjects verbally indicated if they felt the stimulation. The stimulation order was randomized and and each stimulation pulse width was presented at least 5 times, and there were a total of 50 trials. Psychometric function was fit to the data using a sigmoid link function:

$$\frac{1}{1+e^{-(x-\alpha)/\beta}}$$

where α is the detection threshold and β is the discrimination sensitivity.

5.3.2.3 Grip Force Training

The detection threshold pulse width and two pulse widths above with a difference of 1ms and 2.25ms were then used to train each subject to generate three levels of forces. Each stimulation was delivered for 3 s, and the subjects gripped and held a hand dynamometer (Vernier, Beaverton, OR, USA) with an appropriate level of force based on their subjective scales for the entire duration of the trial. There was a intertrial rest period of 3 s, with a jitter of ±0.5 s. After each trial, the average force traces and variances for all three stimulation levels up to the current trial were displayed on the screen as visual feedback. There were a total of 30 trials, and each condition was presented at least 8 times. The subjects were trained until we saw a clear separation between the three levels. Both of our subjects reported difficulty in discriminating between the medium and high stimulation at the beginning, so the gap between those two were larger than that between the low and medium conditions to encourage clear distinction.

5.3.2.4 EEG Recording

After sensory feedback grip force mapping, the subjects went through a 3-block EEG experiment. Sixty four channel EEG data was collected with silver/silver chloride electrodes at a sampling rate of 500 Hz using a SynAmps 2 system (Compumedics Neuroscan, Charlotte, NC, USA). All electrode impedance was below 10 kΩ. There were 144 trials for each block with a long rest period every 30 trials. The subjects were asked to focus on a crosshair on the monitor during each trial to reduce eye artifacts. During block 1 (Stim Force), the subjects gripped the hand dynamometer solely relying on the TENS feedback. There were three levels of stimulation, and each condition was repeated at least 24 times. During block 2 (Stim Only), the subjects passively received stimulation and did not respond. Besides the three levels of intensity used in block 1, a subthreshold stimulation was added as the control. The subthreshold pulse width is below the detection threshold such that the subjects did not feel any referred or local sensation. Each condition was repeated at least 15 times. During block 3 (New Stim), a higher stimulation intensity was introduced without informing the subjects. The purpose is to explore how the subjects would interpret the new stimulation both behaviorally and cognitively. The new stimulation pattern pulse width was 2.75 ms above the threshold. Each condition was repeated at least 15 times.

At the start of each trial, the stimulator Arduino sent a 10-µs pulse trigger to the EEG recording system to symbolize the beginning of a trial. During each trial, whenever the response force surpassed 1 N, the sensor Arduino connected to the hand dynamometer would send another 10-µs pulse trigger to mark the beginning of response.

5.3.3 EEG Processing

The raw 64 channel EEG data was processed using the EEGLAB and ERPLAB toolboxes in MATLAB (MathWorks, Natick, MA, USA) [15]. The EEG signal was bandpass filtered between 0.1 Hz and 30 Hz, and notch filtered between 59 and 61 Hz to get ride of power grid interference. Both filters used the default IIR Butterworth filter in ERPLAB. Muscle artifacts were removed with EEGLAB Automatic Artifact Rejection (AAR) plugin. The continuous EEG data was imported into ERPLAB to generate epochs and ERPs. An EventList is created for each event in the recording. Each trial was assigned to a specific bin based on the stimulation intensity using a bin description file, and a -500 ms–trial end epoch was extracted for each trial. Independent component analysis was performed on the epoched data to remove eye and other artifacts. Lastly, averaged ERP was calculated for each condition in each block using ERPLAB. More details can be found in the preprocessing pipeline in the appendix.

5.3.4 Statistical Analysis

The average force generated for each condition and the variance was calculated at each time point from all trials for training, block 1 (Stim Force), and block 3 (New Stim). A one-second time window was selected based on a visual inspection of the steady state of generated force. The time window selected for training block was from 1.5 to 2.5 s, and were from 1 to 2 s for both block 1 and 3. Then the average force and the average variance was calculated within the time window. A one-way ANOVA test was performed to observe any statistical significance between the force profiles of the 3 conditions.

The reaction time for each trial was calculated by subtracting the time of the response trigger by the time of the stimulus trigger from the EEG data. Then the mean and the variance of the reaction time were calculated for each condition in each block. A paired-sample t-test was performed to identify any statistical significance between reaction time and condition.

The P300 mean amplitude was extracted from a time window of 300ms to 500 ms based on a combination of past studies and visual inspection of the data [10], [11]. The results were compared qualitatively. Once we have recordings from more subjects, we will perform a 2-way ANOVA test to locate any variations accounted by the conditions.

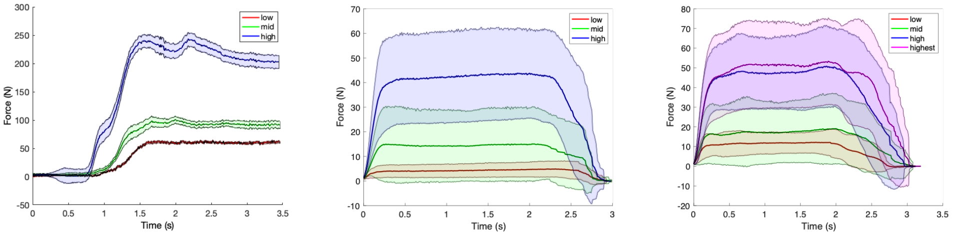

(a) Training **(b)** Block 1 **(c)** Block 3

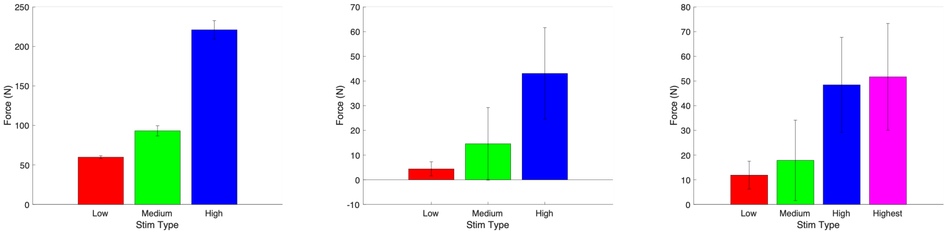

(d) Training **(e)** Block 1 **(f)** Block 3

Figure 5.1: Representative Averaged Force Dynamics (a) Force dynamics during training. (b) Force dynamics during Block 1. (c) Force dynamics during Block 3. (d) Averaged steady-state force during training. (e) Averaged steady-state force during Block 1. (f) Averaged stead-stage force during Block 3.

5.4 Results

5.4.1 Force Levels

The steady state forces generated during training are 59.82 ± 1.76N, 94.10 ± 6.80N, and 232.36 ± 12.17N. The steady state forces during block 1 are 4.16 ± 2.71N, 14.32 ± 14.64N, and 42.24 ± 18.49N. And the steady state forces for block 3 are 11.89 ± 5.63N, 17.86 ± 16.31N, 48.45 ± 19.24N, and 51.71 ± 21.62N.

During training, the subjects were able to generate three statistically significant different levels of forces ($F(2, 273) = 266.49, p < 1\text{e}{-5}$). Post hoc analysis showed statistical differences between low and high, and medium and high conditions ($p < 1\text{e}{-5}, p < 0.01$) as shown in Fig. 5.1a.

During block 1, the average steady force increased with the intensity of the stimulation ($F(2, 136) = 91.98, p < 1e{-}27$), and post hoc analysis showed statistically significant difference between all three stimulation conditions ($p < 0.05$ for low and medium, $p < 1e{-}24$ for low and high, and $p < 1e{-}16$ for medium and high).

Similar situations follows in block 3 ($F(3, 140) = 52.15, p < 1e{-}21$). Post hoc analysis showed statistically significant differences between low and high, low and highest, medium and high, medium and highest conditions ($p < 1e{-}13, p < 1e{-}16, p < 1e{-}11, p < 1e{-}13$). A new stimulation with the longest pulse width was introduced in block 3 to observe how the subjects would respond to the stimulus both behaviorally and cognitively. In terms of force levels, the highest condition elicited slightly larger grip force on average than the high condition, but the difference was not significantly different.

As the experiment progressed from training to block 1, then to block 3 at last, we observed habituation in the levels of force generated for each condition. For the low stimulation condition, the average steady state force dropped from 59.82N in training to 4.16N in block 1 and 11.89N in block 3. The medium stimulation condition saw a larger drop from 94.10N in training to 14.32N in block 1 and 17.86N in block 3. Lastly, the high stimulation condition had the most dramatic drop from 232.36N to 42.24N in block 1 and 48.45N in block 3. Although there was habituation in the experiment, the subjects were not confounding between the three levels of stimulation. It showed that as experiment went on, the subjects were getting better and could apply finer control over the generated forces. Although we see a small raise in grip forces going from block 1 to block 3, the change is not significant in any of the three

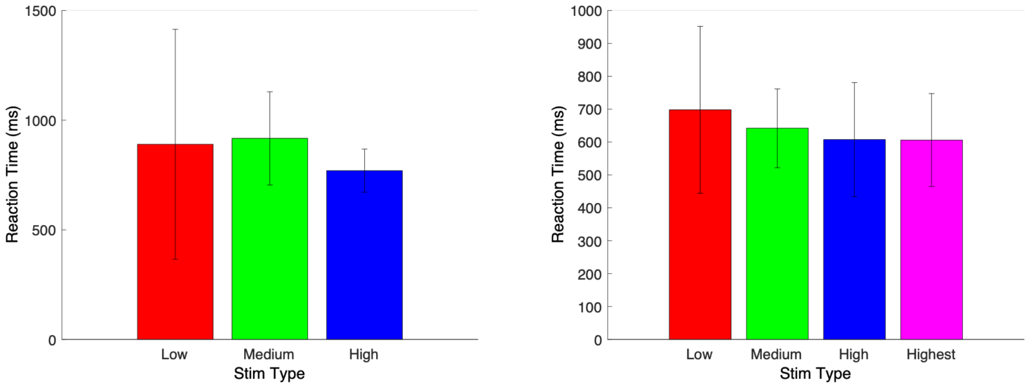

(a) Block 1

(b) Block 3

Figure 5.2: Reaction Times

conditions. We suspect that the introduction of a highest stimulation condition in block 3 might had confounded the discrimination process and caused the general increment.

5.4.2 Reaction Time

Reaction time data was calculated based on the triggers recorded in the EEG data, thus they are only available for blocks 1 and 3. The reaction times for block 1 are 890.10 ± 524.45s, 916.96 ± 212.58s, and 769.62 ± 98.31s for low, medium, and high conditions respectively. The reaction times for block 3 are 698.20 ± 253.70s, 642.09 ± 119.85s, 607.65 ± 173.54s, and 606.24 ± 141.27s for low, medium, high, and highest conditions respectively.

The reaction time data did not show any specific trend in block 1, but did show a slight downward trend in block 3 as stimulus intensity increased. The one-way ANOVA test did show statistical differences between conditions

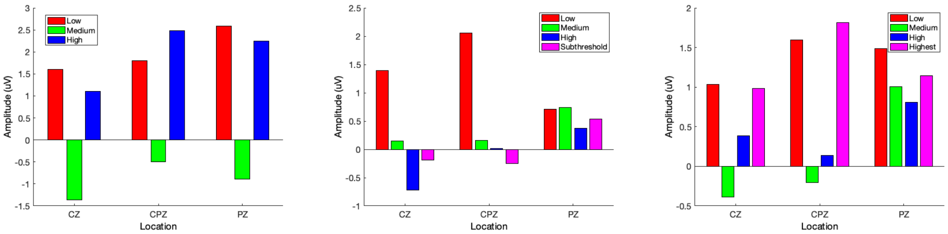

(a) Block 1 **(b)** Block 2 **(c)** Block 3

Figure 5.3: P300 Mean Amplitude

($F(2, 227) = 3.42, p < 0.05$). We hypothesized that as the experiment progressed, the subjects became more familiar with the stimulus and was able to determine the stimulus type in a shorter period of time. The discrimination task became much easier for the higher intensity stimuli than the lower intensity ones.

Similar to the grip force responses, the reaction time also experiences a habituation effect groin from block 1 to block 3 for each condition ($F(1, 227) = 35.27, p < 1\mathrm{e}{-7}$). The drops in reaction time are statistically significant for the medium condition ($p < 0.01$), but not for the low or high conditions. This shows that the subjects was still improving how to differentiate between the stimuli even after training was completed.

5.4.3 P300

The P300 mean amplitudes for the midline electrodes (CZ, CPZ, and PZ) are measured from a time window of 300 ms to 500 ms post-stimulation. The mean amplitudes of the CZ electrode for block 1, in an order of low, medium, and high conditions, were 1.60µV, −1.36µV, and 1.10µV. The mean amplitudes of the CZ electrode for block 2 were 1.39µV, 0.15µV, −0.72µV for the low, medium, and high conditions, and −0.19μV for the subthreshold condition. The mean amplitudes of the CZ electrode for block 3 were 1.032μV, −0.388μV, 0.384μV for the low, medium, and high conditions, and 0.985μV for the highest condition. Similar trends were observed for the CPZ and PZ electrodes.

As mentioned in the introduction, the P300 amplitude might increase because the subjects was paying more attention to the task, or it might decrease because the subjects was more uncertain about the category of the stimulus. In our current case, we observed a U-shape in the P300 amplitudes in block 1 and block 3 for all electrodes. In 2007, Azizian and Polich conducted an ERP experiment, in which the subjects were asked to memorize and recall an list of 12 words, and they discovered also that the P300 mean amplitudes displayed a U-shape in terms of the order of the word in the list [16]. The words in the first 3 and last 3 positions elicited larger P300 amplitudes than words in the middle. The percentage of successful recall also demonstrated this primacy and recency effects. Therefore, in the case of memory recall tasks, the P300 amplitude would decrease if the word is harder to memorize because of its position. Thus, a U shape was present in both the success rate and the P300 amplitude. Based on this previous study, we believe that our block 1 and block 3 P300 mean amplitudes exhibited U shapes because it was easier for the subjects to discriminate the lowest and highest levels of stimulations within a block, but harder to make a decision when it is a medium level stimulation. Based on this hypothesis, it is interesting to note that when a higher stimulation was introduced in block 3, the P300 amplitudes of the high condition became much smaller. Although the subjects was not able to discriminate between the high and highest stimuli behaviorally, the brain was able to recognize the introduction of a new highest stimulus and became uncertain when the previously highest stimulus was presented.

We also conducted a stimulation-only block between block 1 and 3 to serve as a long rest period and control for the experiment. A subthreshold stimulation was introduced in this block. Since the subjects was not able to perceive the subthreshold stimulation, it should not elicit any sensory or cognitive components, and was used as a template for baseline activities. For the other three stimulation conditions, since the subjects was only passively receiving stimulation and was not making any judgement about the categories of the stimuli, the P300 component should not be present. Here in this case, we observed a large peak for the low stimulation condition, and small peaks for the rest of the conditions. We hypothesized that because the low stimulation condition shared the same parameters with the subjects's perception threshold, the brain dedicated more attention to analyze the stimulus and generated a large peak in the time window. The absence of the U-shape in block 2 demonstrated that, in our current task setting, the P300 component is related to the cognitive discrimination of the stimulus categories and is correlated with the difficulty of the task.

5.5 Conclusion

This chapter presented a study aimed to study the behavior and cortical processing of untrained TENS grip force feedback through the lens of ERP.

We designed a 3-block EEG experiment that was capable of eliciting graded referred sensation in the palm of able-bodied subjects and recording responses both in the hand and in the brain. We found that the subjects was able to generate three statistically different levels of force after a short training, and marginally higher level of force for an untrained higher intensity stimulation. We also found that there is statistical differences in reaction time for the three trained conditions, with the highest stimulation having the shortest reaction time. Habituation was present in terms of both force levels and reaction time, and it showed that the subjects was improving his performance throughout the experiment. Lastly, we were able to identify the P300 component as a marker for the cognitive processing of sensory stimuli. The component mean amplitude exhibited a U shape plotted against the stimulation intensity. We hypothesized that the component mean amplitude is negatively correlated with the difficulty of the discrimination task. In the future, we would like to recruit more subjects to further elucidate the relationship between the P300 component and subjects behavior within sensory feedback paradigms.

5.6 Acknowledgement

The work for this chapter was performed under the guidance of Dr. Nitish Thakor and Cathering Ding.

References

[1] E. D'anna, F. M. Petrini, F. Artoni, I. Popovic, I. Simanić, S. Raspopovic, and S. Micera, "A somatotopic bidirectional hand prosthesis with transcutaneous electrical nerve stimulation based sensory feedback," *Scientific reports*, vol. 7, no. 1, pp. 1–15, 2017.

[2] H. Shin, Z. Watkins, H. H. Huang, Y. Zhu, and X. Hu, "Evoked haptic sensations in the hand via non-invasive proximal nerve stimulation," *Journal of neural engineering*, vol. 15, no. 4, p. 046 005, 2018.

[3] L. Osborn, M. Fifer, C. Moran, J. Betthauser, R. Armiger, R. Kaliki, and N. Thakor, "Targeted transcutaneous electrical nerve stimulation for phantom limb sensory feedback," in *2017 IEEE Biomedical Circuits and Systems Conference (BioCAS)*, IEEE, 2017, pp. 1–4.

[4] S. Raspopovic, M. Capogrosso, F. M. Petrini, M. Bonizzato, J. Rigosa, G. Di Pino, J. Carpaneto, M. Controzzi, T. Boretius, E. Fernandez, *et al.*, "Restoring natural sensory feedback in real-time bidirectional hand prostheses," *Science translational medicine*, vol. 6, no. 222, 222ra19–222ra19, 2014.

[5] T. Rosenbaum-Chou, W. Daly, R. Austin, P. Chaubey, and D. A. Boone, "Development and real world use of a vibratory haptic feedback system for upper-limb prosthetic users," *JPO: Journal of Prosthetics and Orthotics*, vol. 28, no. 4, pp. 136–144, 2016.

[6] L. E. Osborn, A. Dragomir, J. L. Betthauser, C. L. Hunt, H. H. Nguyen, R. R. Kaliki, and N. V. Thakor, "Prosthesis with neuromorphic multilayered e-dermis perceives touch and pain," *Science robotics*, vol. 3, no. 19, 2018.

[7] E. D'Anna, G. Valle, A. Mazzoni, I. Strauss, F. Iberite, J. Patton, F. M. Petrini, S. Raspopovic, G. Granata, R. Di Iorio, *et al.*, "A closed-loop hand prosthesis with simultaneous intraneural tactile and position feedback," *Science Robotics*, vol. 4, no. 27, 2019.

[8] D. M. Page, J. A. George, D. T. Kluger, C. Duncan, S. Wendelken, T. Davis, D. T. Hutchinson, and G. A. Clark, "Motor control and sensory feedback enhance prosthesis embodiment and reduce phantom pain after long-term hand amputation," *Frontiers in Human Neuroscience*, vol. 12, p. 352, 2018.

[9] K. Ding, A. Dragomir, R. Bose, L. E. Osborn, M. S. Seet, A. Bezerianos, and N. V. Thakor, “Towards machine to brain interfaces: Sensory stimulation enhances sensorimotor dynamic functional connectivity in upper limb amputees,” *Journal of neural engineering*, vol. 17, no. 3, p. 035 002, 2020.

[10] S. Sutton, M. Braren, J. Zubin, and E. John, “Evoked-potential correlates of stimulus uncertainty,” *Science*, vol. 150, no. 3700, pp. 1187–1188, 1965.

[11] E. Donchin, W. Ritter, W. C. McCallum, *et al.*, “Cognitive psychophysiology: The endogenous components of the erp,” *Event-related brain potentials in man*, vol. 349, p. 411, 1978.

[12] M. Kutas, G. McCarthy, and E. Donchin, “Augmenting mental chronometry: The p300 as a measure of stimulus evaluation time,” *Science*, vol. 197, no. 4305, pp. 792–795, 1977.

[13] R. Johnson Jr, “On the neural generators of the p300 component of the event-related potential,” *Psychophysiology*, vol. 30, no. 1, pp. 90–97, 1993.

[14] S. J. Luck, *An introduction to the event-related potential technique*. MIT press, 2014.

[15] A. Delorme and S. Makeig, “Eeglab: An open source toolbox for analysis of single-trial eeg dynamics including independent component analysis,” *Journal of neuroscience methods*, vol. 134, no. 1, pp. 9–21, 2004.

[16] A. Azizian and J. Polich, “Evidence for attentional gradient in the serial position memory curve from event-related potentials,” *Journal of cognitive neuroscience*, vol. 19, no. 12, pp. 2071–2081, 2007.